Polytechnic University of Marche
Department of Civil and Building Engineering and Architecture
Civil and Building Engineering and Architecture Curriculum

The evolution of spilling breakers: experiments and analyses

Ph.D. Dissertation of:
Alessia Lucarelli

Advisor:
Prof.re Maurizio Brocchini

Coadvisor:
Dr. Claudio Lugni

Curriculum Supervisor:
Prof.re Stefano Lenci

XV edition - new series

Polytechnic University of Marche
Department of Civil and Building Engineering and Architecture
Civil and Building Engineering and Architecture Curriculum

The evolution of spilling breakers: experiments and analyses

Ph.D. Dissertation of:
Alessia Lucarelli

Advisor:
Prof.re Maurizio Brocchini

Coadvisor:
Dr. Claudio Lugni

Curriculum Supervisor:
Prof.re Stefano Lenci

XV edition - new series

Polytechnic University of Marche
Department of Civil and Building Engineering and Architecture
Polytechnic University of Marche
Via Brecce Bianche – 60131 Ancona (AN), Italy

...to my loving parents

Acknowledgments

The writing and completion of this dissertation would not have been possible without the help of so many people in so many ways. It was also the product of a large measure of fortuitous encounters with people who have changed the course of my studies I wish to express a deep sense of gratitude to my advisor, Professor Maurizio Brocchini, who provided me with the opportunity to prepare the project. I thank him for his advice, guidance, valuable comments, suggestions and constructive criticism. I would like to express my deepest gratitude to my co-advisor Dr. Claudio Lugni for his full support, expert guidance and understanding. Without his incredible patience and timely wisdom and counsel, my thesis work would have been frustrating and overwhelming. A special thank you goes to Massimo, for his attentions, care and support before, during and after the experimental campaign. All of my experimental work would not have been completed Without his and Mario's assistance and support in the laboratory where I have spent a lot of time in the last year. They have all made it possible for me to commence and complete this enormous task. I would like to acknowledge and commend them for their effort, cooperation and collaboration Which have all contributed towards the development of this project. This is in spite of the difficult challenges and predicaments that we were all faced with. My thank you also go to my friends: Andrea B., Andrea C., Fabio, Giuseppina, Matteo and Salvatore for their friendship, trust, support and mostly for their laughter and smiles. Last but not least, I would like to thank my family, for their unconditional love and support during the last two years. I would not have been able to complete this thesis without their continuous love and encouragement.

Ancona, Novembre 2016

Alessia Lucarelli

Abstract

The objective of this dissertation is to understand the physics of a spilling breaker and the validation of a simplified mathematical model. Such a model is based on a three-layer structure: an underlying potential flow, a thin, turbulent single-phase layer in the middle and a turbulent two-phase layer (air-water) on the upper part (see Brocchini (1996)). The analysis relies on the data obtained from dedicated laboratory experiments on a spilling breaker. One major challenge was to reproduce an unsteady spilling breaker with high repeatability and, at the same time, with a good accuracy in the measurement of mean and turbulent physical quantities. A large part of this work was the design, construction and building of the experimental setup. A sloshing wave was used for the generation of the breaker. A 3m long, 0.6m deep and 0.10m wide tank was built in Plexiglass and forced through an hexapode system, which allows a high accuracy of the motion. To ensure repeatability of the phenomenon, a suitable breaker event was generated to occur during the first two oscillation cycles of the tank. The tank motion was suitably designed using a potential Harmonic Polynomials Cell and a Navier-Stokes solver. The latter, was useful to understand the dimension of the area of interest for the measurements. An accurate analysis of the breaker inception and its evolution inside the tank, was done in order to evaluate the geometric characteristics of the wave and, in particular, the definition of the water depth condition, for the definition of the length scale to use for make dimensionless time and the quantities to evaluate. Mean and turbulent kinematic quantities were measured using the Particle Image Velocimetry (PIV) method. The evolution of the breaker is described in terms of both global and local properties. Wave height and steepness show that after an initial growth, the height immediately decays after peaking, while the wave steepness remains constant around 0.25. The evolution of the local properties, like vorticity and turbulence, vortical and turbulent flows displays the most interesting dynamics. Two main stages characterise such evolution. In stage (1), regarded as a "build-up" stage, vorticity and Turbulent Kinetic Energy rapidly reach their maximum intensity and longitudinal extension. During such stage the thickness of the single-phase turbulent region remains almost constant. Stage (2), is regarded as a "relaxation" stage, characterised by some significant flow pulsation till the wave attains a quasi-steady shape. In support to the analytical, three-layer model of Brocchini and co-workers it is demonstrated that

the cross-flow profile of the mean streamwise velocity U inside the single-phase turbulent layer is well represented by a cubic polynomial. However, differently from available steady-state models the coefficient of the leading-order term is function of time: $A = A(s,t)$. During stage (1) a fairly streamwise-uniform distribution of U is characterized by $A(s,t) \approx 1$, while during stage (2) U is less uniform and A varies over a much larger range.

Contents

List of Figures

List of Symbols

$\Delta\rho$	Water-air density difference
Δs	Distance of the seeding particle
Δt	Time interval of particles displacement
ϵ	Thickness parameter
γ	Surface tension
$\hat{U}$	Mean streamwise velocity at the lower limit of the one-phase turbulent flow
κ	Local curvature of the free surface
λ	Wavelength
$\langle u(1) \rangle$	Streamwise component of the mean velocity in physical component
$\langle u^2 \rangle, \langle v^2 \rangle, \langle uv \rangle$	Reynolds Stress terms
μ	Ratio of the scales for turbulent velocities and mean flow
ν	Kinematic viscosity
Ω	Angular velocity
ω	Angular velocity
$\partial\phi/\partial s$	Velocity of the potential flow
σ	$\sigma = n/b$
Υ	Interface between potential flow and one-phase turbulent flow
A	Oscillation amplitude of tank motion
a_n	Amplitude of the n-th wave component
B	F/EC Threshold
b	Thickness of the single-phase turbulent flow

b^*_{max}	Dimensionless maximum thickness of the single-phase layer
Bo	Bond number
C	Phase speed
d_{pi}	Seeding particles diameter
E	Energy density
F	Local energy flux
Fr	Froude number
g	Gravity acceleration
H	Wave height
h_0	Filling depth
$kH/2$	Wave steepness
k	Wave number
k_c	Wave number of the central wave in the wave group
L^*_{max}	Dimensionless interface length
L_s	Length of Υ
n	Crossflow local coordinate
P	Pressure
R_x, R_y	Maximum displacements of the Hexapode System in the horizontal plane
Re	Reynolds number
S	Global steepness
s	Streamwise local coordinate
S_0	Critical wave steepness
St	Stokes number
t^*	Dimensionless time
U	Mean streamwise velocity
u	Turbulent streamwise velocity

U_c	Crest particle velocity
V	Mean crossflow velocity
v	Turbulent crossflow velocity
U_b	Mean streamwise velocity at the upper limit of the one-phase turbulent flow

Chapter 1

Introduction

Wave breaking plays an important role for the dissipation of wave energy and momentum and for heat and mass transfer at the air-sea interface. It is also responsible, in conjunction with currents, for the erosion of beaches, the transport of seabed sediments and the interaction with ships and structures.

Wave breaking is, generally, associated with steep waves and the phenomenon of breaking cannot be ignored in the statistical prediction of wave height, which is of great importance for ocean engineers.

The breaker is characterized by turbulent dissipative processes that involve air-entrainment and the generation of a two-phase flow. Thus, the intrinsic difficulty of studying a breaker from theoretical, experimental and numerical viewpoints.

The goal of this work is to understand the physics of a spilling breaker and support and validate a simplified mathematical model by Brocchini (1996). One major challenge of the present study, was the generation of an unsteady spilling breaker, with high repeatability, PIV measurements very close to the free surface and good accuracy of measured mean and turbulent physical quantities, which requires an ensemble average. Experimental data was used both to study the geometric characteristics of the wave along with its kinematics and for the validation of the analytical model by Brocchini (1996).
With the main objective of fulfil the above mentioned requirements, a gentle breaker is generated. This ensures an almost 2D flow in the vertical plane and a weak turbulence level in the turbulent layer. Although this is not common in nature, it is well suited to the validation of the analytical model by Brocchini (1996) where the details and the theoretical issues of the free-surface flow are taken into account.

1.1 Description of wave breaking inception

A breaking event at a beach or in the open sea is easily detectable watching the generation of foam and noise. Alternatively, breaking may be regarded to start when the wave becomes too energetic and unstable. A wave can contain

a maximum amount of energy and when this limit is exceeded, the wave starts to release, through breaking, some of its excess energy.
When breaking occurs, the motion of the wave changes rapidly, the flow evolves into a turbulent and unpredictable form. Viscous forces become important and energy is dissipated into heat.

In nature different types of breaking occur: spilling, plunging, surging, etc. (see Fig.1.1).

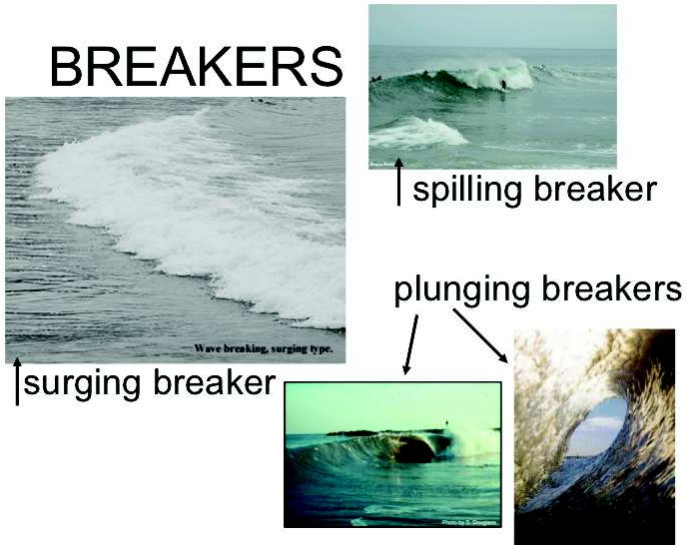

Figure 1.1: Different types of breaking waves.

In this thesis an unsteady spilling breaking wave is considered and it is the most common type of breaker in deep water. Spillers in the open sea, essentially forced by the wind friction on the sea surface, or, to a more limited extent, by steepness limitation, are also defined *whitecaps* (see Fig. 1.2). In deep-water spillers the turbulence is confined in a region near the crest of the wave, with white water spilling down the front face, starting from the wave crest.

Important observations of the wave crest-profile in the vicinity of breaking and its evolution, were performed by Duncan et al. (1994). They observed in detail the wave crest evolution of unsteady spilling breakers, induced through dispersive focusing, using a high-speed camera with a resolution of 500 fps. They reported on the generation of a bulge, parasitic capillary waves and the subsequent breakdown of the bulge into turbulence in the forward face of the crest. Hence, according to Duncan breaking is essentially connected with the injection of vorticity into the flow, largely through parasitic capillaries as proposed by Longuet-Higgins (1992). In a subsequent study, Duncan et al. (1999) measured the maximum surface elevation, the length and thickness of the bulge,

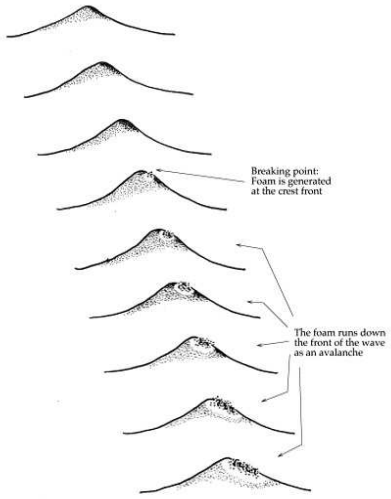

Figure 1.2: Evolution of a spilling breaker.

the position of the toe and the capillary waves. This was done in order to describe the crest shape deformation. Testing multiple breaking waves, they observed the same behaviour of the crest front face. This was also confirmed by Diorio et al. (2009) using three different breaking modalities: dispersive focusing, modulation instability and wind forcing. They generated unsteady spilling breakers with lengths ranging from 10 to 120 cm and observed that, independently of the method used for wave breaking generation, bulge and capillary waves always occur on the crest-front face (See Fig. 1.3). This similarity

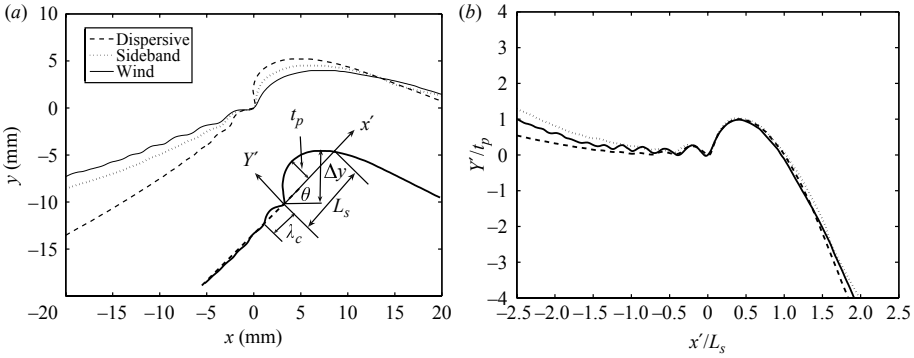

Figure 1.3: Crest profiles of spilling breakers generated by three different methods and their geometric similarity. Adapted from Diorio et al. (2009).

was attributed to the crest flow being dominated by both surface tension and

gravity (Duncan, 2001; Diorio et al., 2009).
The deformation of the wave crest approaching breaking can also be influenced by surface tension. The relative importance of buoyancy to that of surface tension, γ, is measured by the Bond number $Bo = \frac{\Delta\rho g\lambda^2}{\gamma}$ where λ is the wavelenght, $\Delta\rho$ the water-air density difference and g gravity acceleration. Being $Bo \approx \lambda^2$, surface tension matters for short wavelengths. Duncan (2001) analysed in detail the important role of surface tension for decreasing wavelenght and breaking intensity. In particular, for large wavelengths and negligible surface tension effects, breaking occurs through a jet-like crest deformation (very locally in case of a gentle breaker) which impinges the wave face, inducing a turbulent spilling process (see left panel of Fig.1.4) with formation of air bubbles and droplets downstream the toe. Conversely, for a shorter wave and for a weaker breaker, the local jet flow is strongly affected by the surface tension and then replaced by a surface tension-dominated ripple pattern, with the formation of a bulge on the wave crest and capillary wave upstream the toe (see right panel of Fig. 1.4). The toe moves upstream inducing a turbulent flow without formation of bubbles. Although Duncan and co-workers largely focussed on surface-tension dominated breakers, i.e. on specific breaking modes, their investigation of the role of surface tension is of interest for the overall understanding of breaking inception. These aspects have been evaluated for

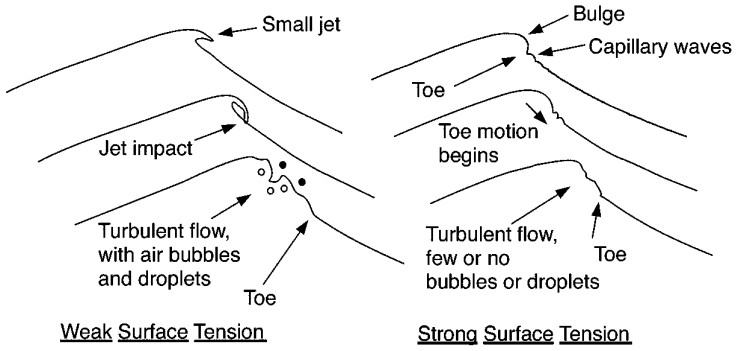

Figure 1.4: Three different phases of spilling breaking for weak and strong surface tension effects. Figure adapted from Duncan (2001).

many years, in order to understand better what mechanisms govern the inception of wave breaking. Such mechanisms have been described in terms of various breaking criteria. Among them, we can mention criteria based on: 1) the air entrainment (see Monahan and Mac Niocaill (2012)), used at first to study the wave in real scale, 2) the steepness of the wave front (Duncan et al., 1999; Diorio et al., 2009; Oh et al., 2005; Tian et al., 2008), 3) the velocity of the near-crest flow (Oh et al., 2005; Tian et al., 2008), 4) the acceleration of

the near-crest flow (Phillips, 1958; Longuet-Higgins, 1963; Snyder et al., 1983; Longuet-Higgins, 1985), 5) the vorticity injection at the free surface (Duncan et al., 1994; Hornung et al., 1995; Dabiri and Gharib, 1997; Qiao and Duncan, 2001), and criteria that refer to the wave energy content (Banner and Peirson, 2007; Tian et al., 2008, 2010). All these criteria have had their merits in the understanding and modelling of this complex phenomenon and are still used in various fashions in various models. Hence, breaking criteria might be regarded as dependent on the type of breaking. However, it is arguable that one single mechanism is at the roots of all types of wave breaking. Like for all breakers, various breaking criteria have been used also for spilling breakers. However, recent studies have focussed on the details of the mechanics underlying breaking inception at spillers.

With regards to geometric characteristics of the wave, Nepf et al. (1998); Wu and Nepf (2002) and Oh et al. (2005), proposed an accurate study of the wave steepness which was used as a critical parameter to predict the breaking onset. From laboratory experiments, the value of this parameter ranges between 0.15 and 0.44. Such large range of variation renders it improbable its universal application to predict the onset of breaking. Babanin et al. (2007, 2010) introduced on the basis of numerical simulations and experimental measurements, a modulation instability that leads to wave breaking. They defined an Initial Monochromatic Steepness (IMS) to predict the breaking onset. They showed that for $IMS > 0.44$ wave breaking occurs immediately and for $IMS < 0.08$ the wave breaks only in presence of wind forcing. Alternatively, Rapp and Melville (1990) proposed a global steepness, $S = k_c(\Sigma a_n)$ associated with the wave group. k_c is the wave number of the central wave in the wave group, and a_n is the amplitude of the n-th wave component. They found that $S_0 = 0.25$, where S_0 is the critical wave steepness above which the breaking onset occurs, worked well for their specific waves. Later, it was shown that S_0 can be affected by the spectral shape: Chaplin et al. (1996) reported $S_0 = 0.25$ and 0.30 for wave groups of constant-amplitude and constant-steepness spectra, respectively. Subsequently Drazen et al. (2008) proposed $S = (\Sigma k_c a_n)$ and reported that the breaking onset due to dispersive focusing is in the range $0.32 - 0.36$. Overall the definition of the parameters used in geometric criteria is simple but, at the some time does not allow for a universally-applicable criterion. Geometric criteria can not give a good prediction of the wave breaking onset because a breaking wave can be generated in different modes, such as dispersive focusing, modulation instability, wind forcing and wave-current interaction. These different mechanisms can influence the breaking wave geometry at onset. Furthermore, the wave can break with different intensity at the some length-scale. This implies that the geometric criteria is destined to fail.

Kinematic criteria relate the horizontal velocity of the crest particle U_c with

the wave phase speed C, and wave breaking is taken to occur when $U_c/C \geq 1$ so $U_c \geq C$. Determination of the crest particle velocity can be facilitated by PIV measurements. In their Annual Review of Fluid Mechanics paper (Perlin et al., 2013), Perlin contributed to the scientific debate on the kinematic breaking criterium. Many authors indeed, found in their investigation, that $U_c/C \geq 1$ is a sufficient, but not necessary, condition for the onset of the breaking. In particular, from numerical simulations of modulating waves, confirmed also by experimental observations, Tulin and Landrini (2001) found that a well-defined criterion in deep water for the onset of the initial wave deformation is $U_c/C = 1$. Note that the last criterion confirms that $U_c = C$ is only a sufficient but not necessary condition for the wave breaking occurrence. With reference to the acceleration of the near-crest profile and the energy variation of higher-frequency wave components, we focus our attention on the local energy growth rate like dynamic breaking criterion. Schultz et al. (1994) reported one of the earliest numerical studies of this type and demonstrated that the energy associated with the root-mean-square wave height can be used to define a breaking criterion for regular 2D deep-water waves. The critical condition is that the potential energy exceeds 52% of the total energy of a limiting Stokes wave. Barthelemy et al. (2015) focused their attention, through a numerical study, on a unified criteria for predicting breaking onset, valid for 2D and 3D gravity water waves propagating over flat topography, for water depth ranging from intermediate to deep. After reviewing the criteria available in the literature, they proposed a new breaking criteria based on the ratio between the local energy flux F and the local energy density E. Because F/E is the local energy flux speed or advection speed associated with the scalar field E, they defined the breaking threshold as the ratio $B = F/EC$, with C local crest velocity. On the free surface B is equal to U_c/C with U_c particle speed. Barthelemy et al. (2015) found that on the crest it is $B = 0.84$ at the onset of breaking (for non breaking waves $B < 0.84$). This criterion comes from the analyses made in the works of Fedele (2014a). Fedele (2014b) indicates that as the wave crest approaches the onset of breaking, it steepness causing a decrease of the crest slowdown due to nonlinear dispersive effects. In particular, preliminary studies (Fedele, Personal communication) suggest that gently focusing wave crests slow down more than steeper crests (see also Fedele (2014a,b)). Thus, the threshold $B = 0.84$ is attained faster as wave crests steepen while the associated particle speed U_c increases as the focusing point is attained (fluid particles tend to accelerate as focusing is approached while crests slowdown less as they steepen because of nonlinear dispersion, Fedele (2014b)). More detail about this study will be presented in Chapter 3. However, at present, the energetic criterion is the most used.

1.2 Problems related to the representation of the breaker

The first conceptual models of a breaking wave regarded it as characterized by a roller residing over the front face of a non-breaking wave or an extensive turbulent region beneath the free surface or in same interpretation of a combination of both.
In the case of the occurrence of a roller region, the breaker is regarded as a closed recirculating region of aerated water in contact with the underlying wave from the crest, downward over the wave face to its leading edge. The flow is studied in a reference frame fixed with the wave and the turbulent velocities are of the same order of magnitude of the wave velocity. The fluid contained in the "roller" is continually mixing with the rest of the turbulent fluid in the wave.
Later studies (Banner and Phillips, 1974; Peregrine and Svendsen, 1978) have shown that the flow just below the breaker is not a roller, but a thin turbulent region. Peregrine (1992) and Banner and Peregrine (1993) provide overview of the principal features about spilling breakers and indicate the formation of an initial mixing layer region leading to a turbulent region beneath the wave crest and Cointe and Tulin (1994) model recirculating eddy sustained by turbulent stresses acting in the shear zone, i.e. mixing layer region.
The onset of the breaking process involves relatively small-scale events in the form of capillary waves, as described by Longuet-Higgins (1973), Longuet-Higgins (1990), Longuet-Higgins (1992), Longuet-Higgins (1994), whereas the final state of breaking exhibits irregular distortion of the free surface in conjunction with large-scale separate flow beneath it, as addressed for example by Peregrine and Svendsen (1978) and Hoyt and Sellin (1989).
On the basis of Duncan et al. (1994) observations, Longuet-Higgins (1994) proposed that the longer capillary wave are unstable waves which occur in a shear layer immediately beneath the free surface. Lin and Rockwell (1994, 1995), showed that a rapid distortion, along the free surface of the flow, occurs at this location leading to a flow separation and, as a consequence, giving rise to a mixing layer with an important concentration of vorticity. Particular attention was put in the interaction between distributed and concentrated vorticity with a free surface. Some of this interactions are important for the vorticity generation and the free surface distortion. A roller-type motion, in the form of a strong, large-scale (single) vortex does not exist, at least in an instantaneous sense, between the free-surface and the mixing layer.

Dabiri and Gharib (1997)(see Fig. 1.5) evaluated the vorticity generation reproducing a spilling breaking wave in laboratory through two different experiments based on different Froude ($Fr = U/\sqrt{gh}$) and Reynolds number

$(Re = Uh/\nu)$.

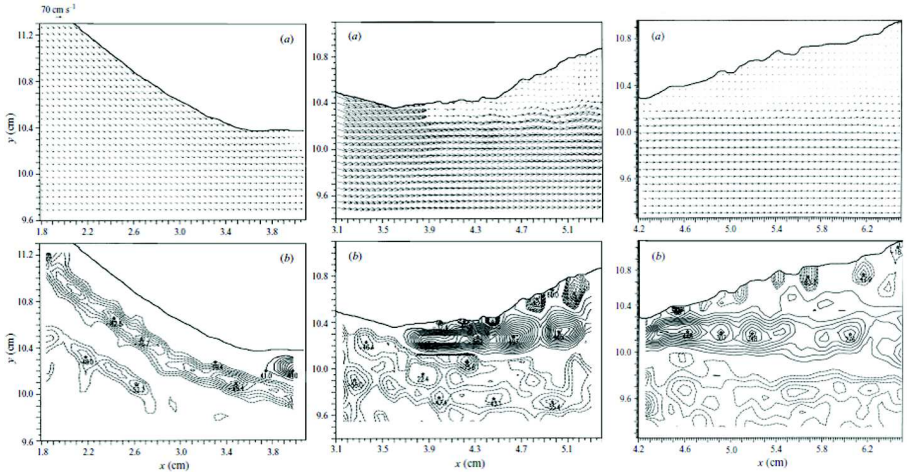

Figure 1.5: Breaking evolution at three differents temporal and spatial stages with a high Froude and Reynols number. From top to bottom, instantaneous velocity and vorticity (dashed lines for negative values and solid lines for positive values) fields are shown (adapted from Dabiri and Gharib (1997)).

In the first case (see Fig. 1.5, left-top panel), for high Froude and Reynolds numbers, they found an initial fast layer of flow which is generated at the surface and behaves like a hydraulic jump. At a more downstream (see Fig. 1.5, left-middle panel), they observed the generation of some surface-parallel vorticity due to the deceleration $(-U_s \partial U_s/\partial s)$ of a thin layer of the surface fluid (see Fig. 1.6).

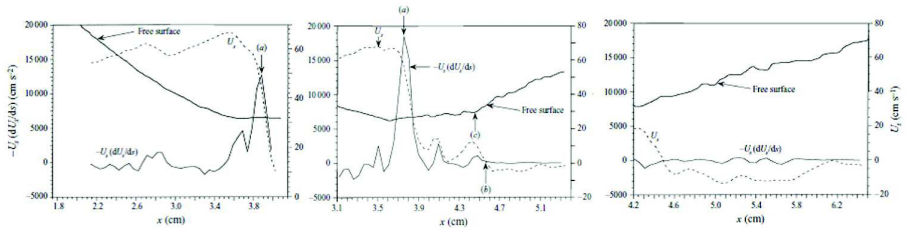

Figure 1.6: The free surface velocity and flow deceleration of the high-Froude number case. The vorticy flux is shown on the left ordinate axis, while the velocity scale is shown on the right ordinate axis; (a) shows the position of the maximum deceleration, and the flux of vorticity into the flow; (b) shows the stagnation point of the free surface fluid and (c) the initiation of wave breaking observed visually (adapted from Dabiri and Gharib (1997)).

This deceleration induces a separation of the turbulent layer that can be regarded as a roller. It was concluded that the source of vorticity was not due to the surface curvature or from a stagnation point, which could be useful to indicate the breaking, but solely due to the flow deceleration. At the most downstream section 3 (see Fig. 1.5, right-top panel and right-bottom panel), the vorticity field in the shear layer is greater than the vorticity in the layer beneath the breaker. In the second case (see Fig. 1.7), for low Froude and Reynolds numbers, no breaking occurs.

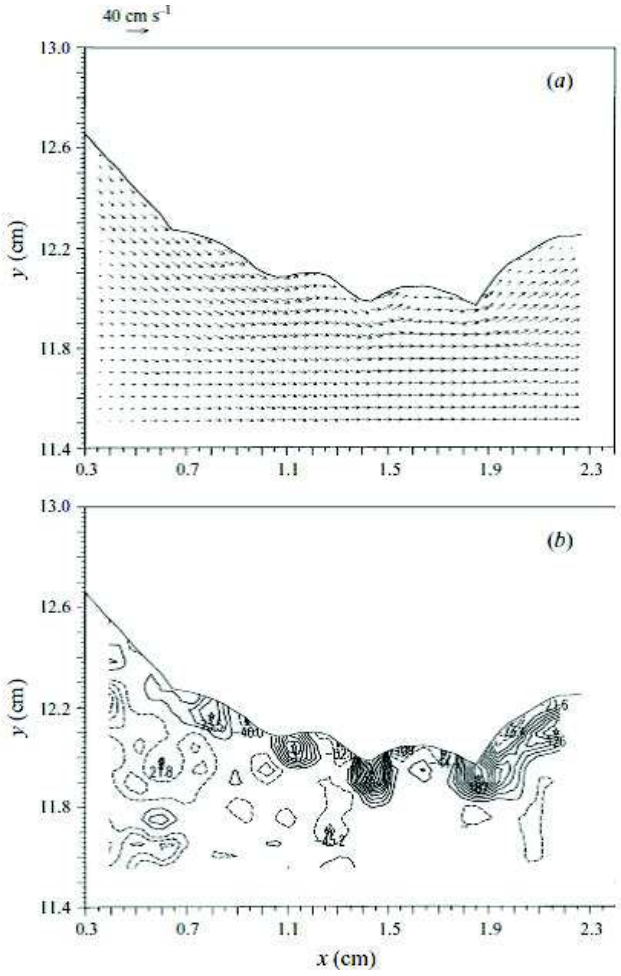

Figure 1.7: Breaking evolution at low Froude and Reynols number. From top to bottom, instantaneous velocity and vorticity (dashed lines for negative values and solid lines for positive values) fields are shown (adapted from Dabiri and Gharib (1997)).

The capillary curvature provide a negligible contribution to the gravity term

for the vorticity flux (see 1.1). The vortical flow is influenced by the deceleration term as the flow passes through the capillary waves. The vorticity flux at the free surface, can be evaluated by the following equation:

$$\nu \left(\frac{\partial \omega_z}{\partial r} \right)_{r=0} = -\frac{\partial U_s}{\partial t} - g \cos\theta - U_s \frac{\partial U_s}{\partial s} \tag{1.1}$$

where ν is the kinematic viscosity, ω_z the vorticity, U_s the velocity parallel to the free surface, (r, s) represent curvilinear orthogonal coordinates, r measuring distances in the normal-to-surface direction and s in the parallel-to-surface direction. For short-wavelenghts and quasi-steady flows, Dabiri and Gharib used the above equation neglecting the first term on the right-hand side.

Similar results were achieved by Misra et al. (2008), for the case of a classic hydraulic jump as shown in Fig. 1.8. They observed, from the analysis of the mean horizontal velocity, that at the jump toe, the adverse pressure gradient induces a rapid axial deceleration. A thin concentrated region of negative vorticity in the breaker shear layer is generated and the change in slope of the free surface plays a central role in determining the maximum vorticity. Near the toe, the value of vorticity decays rapidly away from the mean surface.

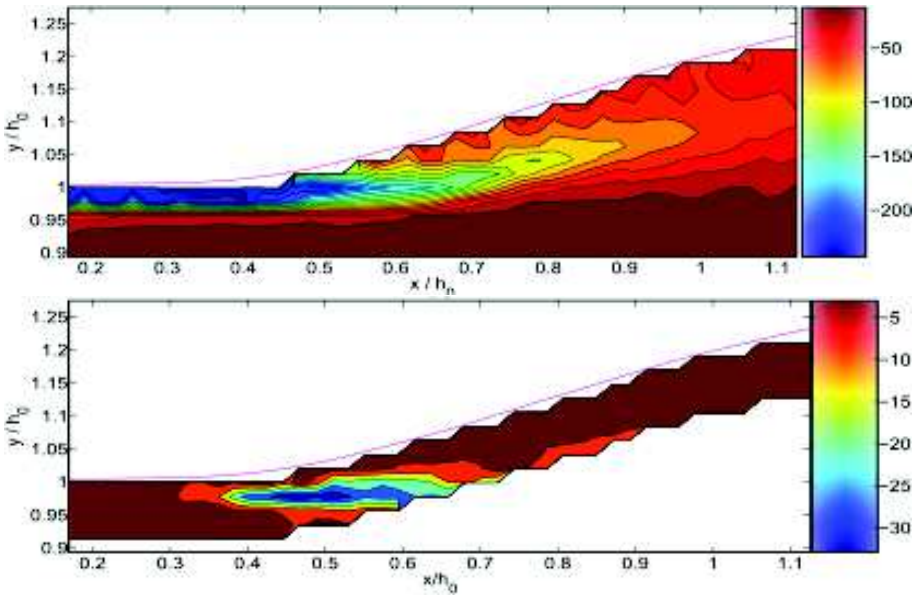

Figure 1.8: Top panel: instantaneous vorticity (1/s). Bottom panel: the ensemble-averaged surface-parallel convective acceleration $\hat{U}_s \partial \hat{U} / \partial s$ (m/s^2) (adapted from Misra et al. (2008)).

This brief description about the wave shape evolution during breaking, the

vorticity generation and its evolution related to the velocity field, provides the basis for a comparative analysis of similar dynamics induced at an unsteady breaker. This will be widely discussed in Chapter 3.

1.3 Analytical models

Over the past 20 years there has been a huge development of numerical models dedicated to the description of breaking waves. Particular attention has been put on the characterization of the free surface and on the bubble structure, on the wave breaking onset and on the dissipation of energy during breaking.

These models can provide useful information on kinematic and dynamic characteristics of a breaking wave , but with the drawback of very large computational costs. For this reasons, in a parallel way, analytical models have been developed, in order to simplify the comprehension and the representation of the breaking wave structure, this also allowing for new numerical models that, benefitting from the extra knowledge available, require a reduced computational effort.

In this section, a chronological summary is given of the models available for an analytical description of the breaker region in fully-formed spilling breakers.

Longuet-Higgins (1973) proposed the first simple model for the local turbulent flow near the forward edge of a steady spilling breaker or a hydraulic jump. The particularity of this model is the different description of the regions of laminar flow and those of turbulent flow. In the equation of motion for the mean flow, gravity was put in balance with Reynolds stresses and near the toe a non-hydrostatic pressure was assumed. The effect of air entrainment was also accounted for in the solution for the surface profile in the turbulent wedge originating from the point of discontinuity. Banner and Phillips (1974) on the basis of experimental studies, suggested that the breaker region did not include a stagnation point, but there was an intermittent zone where a low velocity water was tumbling down the front of the crest.

Longuet-Higgins and Turner (1974) proposed an entraining plume model where the spilling breaker was approximated as a turbulent gravity current riding down the forward face of a wave while laminar flow would entrain from below. The entrainment was modelled by a finite tangential stress at the boundary between the turbulent and laminar flows. For the first time, the role of the air-water mixing and the unsteady motion of the toe front was included; however, turbulence was confined within the surface roller. The steady, part of the whitecap would entrain water from below and air from above, at such a rate that the density of the air-water mixture would remain constant (see Fig. 1.9). At the front of the layer fluid would be fed into a circulating region similar to a half of a vortex pair. Extra entrainment of both air and water would certainly

occur in this case, and the penetration of the surface of the wave below would be greater than it is in the steady part of the flow (see Fig. 1.10).
From experimental investigations they found that the density of the mixture near the front could be taken as constant. This results is better applicable to the front rather than the flow behind the wave crest.
Although this theory was formulated for steady motion, it was shown to approximately describe both the acceleration of the front of an unsteady spilling breaker, as well as the geometry of the breaking region,prompting its use as possible model describing the geometry and kinematic of an unsteady spilling breaking wave.

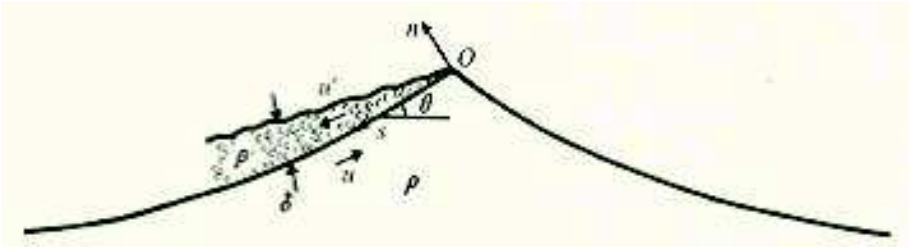

Figure 1.9: Sketch of a spilling breaker. The wave is moving from right to left and has a whitecap on its forward face. The velocities in both the wave and whitecap are measured relative to the wave crest, with positive direction downwards. Adapted from Longuet-Higgins and Turner (1974).

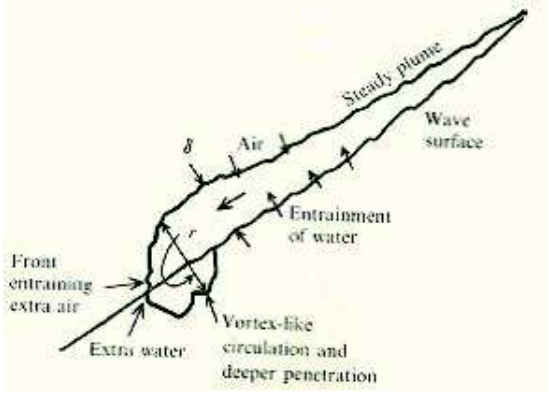

Figure 1.10: Sketch of the "starting plume" interpretation of an advancing whitecap. Adapted from Longuet-Higgins and Turner (1974).

In Madsen and Svendsen (1983) the turbulent region of a bore or hydraulic jump was modeled as a liquid wedge spreading from the toe front downward in the water body (see Fig. 1.11). Completely different from the previous works,

motivated by the observation by Peregrine and Svendsen (1978), the present model was based on depth-integrated equations. This in combination with the assumption of static pressure. A simplified $k-\epsilon$ turbulence model was used in the turbulent region to properly describe the local hydrodynamics. Although the turbulence generated at the breaker toe is realistic, the model does not take into account the air phase, flow unsteadiness, flow rotation and local curvature. Further, an infinite cross-flow velocity gradient at the toe front induces a toe singularity. Also neglected were the bottom boundary layer and shear stresses, which are natural dynamics in a bore. By restricting the analysis to such flow, they also avoided the problem of separation of the bottom boundary layer due to the adverse pressure gradient under the jump and the eventual formation of a standing vortex near the bottom, which may occur in cases of "fully developed" flow.
The major differences with the analytical model of Longuet-Higgins (1973) and Longuet-Higgins and Turner (1974), are that Longuet-Higgins (1973) suggested that: i) the toe was a stagnation point and ii) the velocity in the turbulent and irrotational region, were finite at the toe and much smaller than the phase speed. More recently Cointe and Tulin (1994), proposed a theory where the

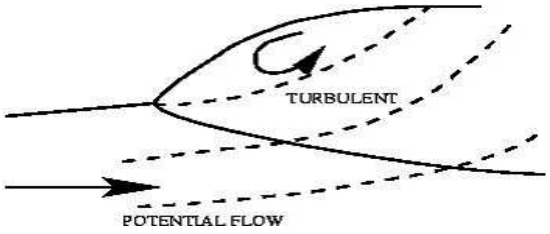

Figure 1.11: Schematic representation of the hydraulic jump/bore of Madsen and Svendsen. Adapted from Madsen and Svendsen (1983).

spilling breaker is approximated as a stationary vortex placed on the forward face of the wave, sustained by the turbulent shear stresses between the eddy and underlying flow (see Fig. 1.12). The turbulence generated at the toe resembles that of a mixing layer and the pressure is hydrostatic. This simple model provides a reasonable description of the incipient breaking conditions; however, it is valid only for quasi-steady breakers. Based on the physical observation that the time scale for the evolution of a breaker is longer than the one relative to the transport of the fluid elements through it, Peregrine (1992) defined a spilling breaker as a quasi-steady breaker in the frame moving with the wave. Conversely the event is taken to be unsteady when the time scale of the evolution of the breaker is smaller than the underlying wave motion. For an unsteady, fully-formed spilling breaker, which is the focus of this work, some analytical studies of specific interest for the present thesis are briefly described

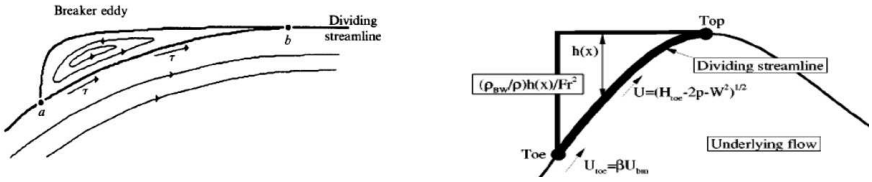

Figure 1.12: Sketch of Cointe and Tulin's analytical model. Adapted from Cointe and Tulin (1994).

in the following.

1.4 Recent analytical models

The summary outlined above, shows that the available analytical models are not fully adequate to reproduce a rapidly evolving, air-water mixing spilling breaker, e.g. turbulence concentrated only in the surface roller; simplified turbulence modeling; no air-water mixing modelling, no flow unsteadiness, no detailed representation of rotation and curvature of the free surface; singularity at the toe i.e. infinite cross-flow velocity gradient at toe. Virtually all "bulk" models, rely on concepts like that of: 1) a "roller" or a "stagnation eddy" near the crest, 2) a turbulent wedge in the form of a breaker shear layer/ mixing layer that originates at the toe because of flow separation, 3) a wake downstream. The roller model can be regarded only as a partial solution for the natural dynamics because it is evident that the fluid in a breaking wave actually mixes with the rest of the turbulent flow. It is, therefore clear that the intermittency of the fluctuating/disrupted air-water surface and the unsteadiness of the breaking process should be properly accounted for. To this purpose recently, Brocchini and co-workers (Brocchini, 1996; Brocchini and Peregrine, 2001a,b) and Brocchini (2002) focused on the effects due to strong turbulence at the water free surface and of the various different dynamics evolving in a breaker, with the aim of improving the modelling of breaking waves and applying it to a wider range of flow conditions. The main finding consists in suitable surface boundary conditions for the turbulent air-water mixture at the front and on the crest of a spilling breaker. The boundary conditions (kinematic and dynamic) are achieved by both Reynolds averaging and, then, integrating across the surface layer (in the region where air and water are present). The mentioned results on the dynamics of an turbulence-disrupted air-water interface have been implemented into the, the analytical model of Brocchini (1996), which somehow similar to that of Madsen and Svendsen (1983), is not limited to shallow-water conditions and quasi-steady flows. Brocchini (1996)'s model introduces, major improvements in representing the mean flow unsteadiness,

the stretching, local curvature and rotation of the turbulent region. In this theory, the spilling breaker is represented through a three-layers system (see Fig.1.13): a top layer, called two-phase flow, which is an air-water mixture; a middle layer characterized by a turbulent, single-phase water flow, which rides on the underling irrotational potential wave body (lowest layer).
The equations of motion were achieved on the basis of curvilinear tensor analysis because it provides the most direct method by which the equations valid for curvilinear coordinate system can be derived (see also Moore (1978)).
The mass conservation equation for an incompressible fluid with constant density ρ and the Euler's equation (conservation of linear momentum), were written in physical variables.
An appropriate coordinate system (s, n) was chosen on the curve $\Upsilon(t)$ (see Fig. 1.13) which represents either the continuous wave free surface,$(D\Upsilon/Dt = 0)$, or, in the case of breaking, a non-material interface between the irrotational flow region below and the region containing turbulent flow above and, therefore, the lower bound of the one phase-turbulent thin layer. Although, turbulence would penetrate below the Υ interface, for simplicity, such dynamics is disregarded. This can also be seen as a case in which the turbulence penetrating down the Υ interface is isotropic and passively decaying. Applying, then, the Reynolds averaging technique $\langle . \rangle$ to conservation equations, the continuity equation, for both mean and turbulent flow, was found:

$$\frac{\partial U}{\partial s} + \frac{\partial}{\partial n}\left[(1-\kappa n)\, V\right] = n\frac{\partial \Omega}{\partial s}\ , \qquad \frac{\partial u}{\partial s} + \frac{\partial}{\partial n}\left[(1-\kappa n)\, v\right] = 0 \tag{1.2}$$

n and s are, respectively, crossflow and streamwise local coordinates, U and u are the mean and turbulent streamwise velocity components, respectively, while V and v are the mean and turbulent cross-flow velocity components, respectively. $\Omega(s,t)$ is the angular velocity of the local frame of reference $(\hat{\mathbf{s}}, \hat{\mathbf{n}})$ and κ is the local curvature. Is possible to see how the angular velocity (Ω) influences only the mean flow while the curvature (κ) influences both the mean flow and the turbulent velocity. These two parameters were defined as follows:

$$\kappa = \hat{n} \cdot \frac{\partial \hat{s}}{\partial s} \qquad , \qquad \Omega = \hat{n} \cdot \frac{\partial \hat{s}}{\partial t} \tag{1.3}$$

The momentum equation was decomposed into streamwise and crossflow components:

$$(1-\kappa n)\frac{\partial U}{\partial t} + (1-\kappa n)\left[\left(V + \hat{\mathbf{n}} \cdot \frac{\partial \mathbf{R}}{\partial t}\right)\frac{\partial U}{\partial n} + \frac{\partial \langle uv \rangle}{\partial n}\right] + \frac{\partial \langle u^2 \rangle}{\partial s} - 2\kappa\langle uv\rangle +$$

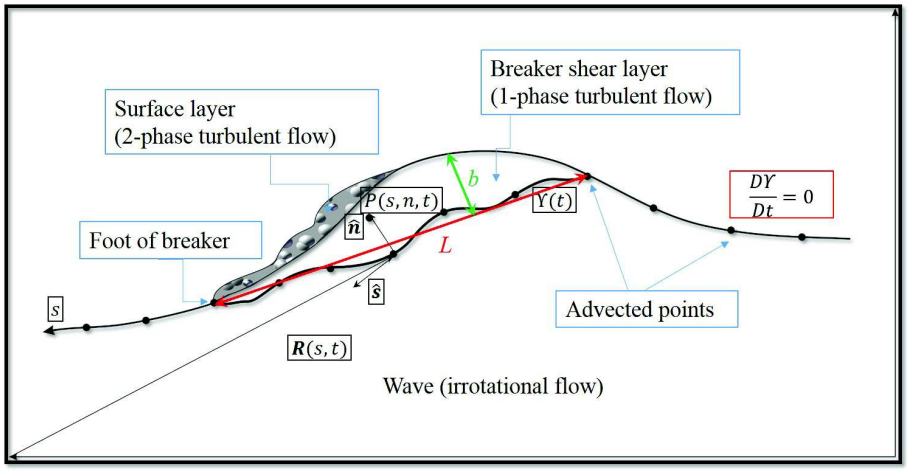

Figure 1.13: Schematic view of the theoretical model of Brocchini (1996).

$$\left(U+\hat{\mathbf{s}}\cdot\frac{\partial\mathbf{R}}{\partial t}-n\Omega\right)\left(\frac{\partial U}{\partial s}-n\frac{\partial\Omega}{\partial s}-\kappa V\right)=(1-\kappa n)\left(V\Omega+\frac{\partial\left(n\Omega\right)}{\partial t}+\hat{\mathbf{s}}\cdot\acute{\mathbf{g}}\right)-\frac{1}{\rho}\frac{\partial P}{\partial s} \quad (1.4)$$

$$\frac{\partial V}{\partial t}+\hat{\mathbf{n}}\cdot\frac{\partial\mathbf{R}}{\partial t}\frac{\partial V}{\partial n}+\frac{1}{2}\frac{\partial V^2}{\partial n}+\frac{\partial\langle v^2\rangle}{\partial n}+\frac{1}{(1-\kappa n)}\hat{\mathbf{s}}\cdot\frac{\partial\mathbf{R}}{\partial t}\left(\frac{\partial V}{\partial s}+\kappa U\right)+$$

$$\frac{(U-\kappa n)}{(1-\kappa n)}\left(\frac{\partial V}{\partial s}+\kappa U\right)+\frac{1}{(1-\kappa n)}\frac{\partial\langle uv\rangle}{\partial s}+\frac{\kappa\left(\langle u^2\rangle-\langle v^2\rangle\right)}{(1-\kappa n)}=n\Omega^2-U\Omega+\hat{\mathbf{n}}\cdot\acute{\mathbf{g}}-\frac{1}{\rho}\frac{\partial P}{\partial n} \quad (1.5)$$

In these equations the Reynolds' stress terms $\langle u_i u_j\rangle$ are responsible for momentum exchanges between turbulence and the mean flow. The contribution of curvature and local rotation like in the continuity equation, make these equations very complex, though similar to those of Bradshaw (1973) for an unsteady turbulent layer.
In order to obtain an analytically feasible solution, a simple turbulent closure model was chosen. A transport equation for the turbulent kinetic energy was also used when non-equilibrium conditions were to be reproduced. Furthermore, geometric and kinematic (1.6) scaling arguments were introduced to simplify the above equations and to analyse the "leading edge of breaker" ($\mu=\mathcal{O}(1)$), "mixing layer" ($\mu=\mathcal{O}(\sqrt{\epsilon})$) and "wake" regimes ($\mu=\mathcal{O}(\epsilon)$):

$$\epsilon=\frac{b}{L} \qquad , \qquad \mu=\frac{u}{U} \quad (1.6)$$

where b is the thickness of the single-phase turbulent layer and L the length of Υ, while μ is the ratio of the scales for turbulent velocities and mean velocities. The finally form of the dimensionless equation is:

- continuity equation for the mean flow:

$$\frac{\partial U}{\partial s}+\frac{\partial V}{\partial n}=\epsilon\left[\kappa\frac{\partial\left(nV\right)}{\partial n}+n\frac{\partial\Omega}{\partial s}\right] \tag{1.7}$$

- streamwise component of momentum equation:

$$\begin{aligned}&\left[\mu^2\frac{\partial\langle uv\rangle}{\partial n}+\hat{\mathbf{n}}\cdot\frac{\partial\mathbf{R}}{\partial t}\frac{\partial U}{\partial n}\right]+\epsilon\left[\frac{\partial U}{\partial t}+V\frac{\partial U}{\partial n}+\left(U+\hat{\mathbf{s}}\cdot\frac{\partial\mathbf{R}}{\partial t}\right)\frac{\partial U}{\partial s}-\kappa n\hat{\mathbf{n}}\cdot\frac{\partial\mathbf{R}}{\partial t}\frac{\partial U}{\partial n}\right.\\&\left.-\mu^2\left(\kappa n\frac{\partial\langle uv\rangle}{\partial n}-\frac{\partial\langle u^2\rangle}{\partial s}+2\kappa\langle uv\rangle\right)\right]-\epsilon^2\left[\kappa n\left(\frac{\partial U}{\partial t}+V\frac{\partial U}{\partial n}\right)+\frac{\partial U}{\partial s}n\Omega+\right.\\&\left.\left(U+\hat{\mathbf{s}}\cdot\frac{\partial\mathbf{R}}{\partial t}\right)\left(n\frac{\partial\Omega}{\partial s}+\kappa V\right)\right]+\epsilon^3\left[n\Omega\left(n\frac{\partial\Omega}{\partial s}+\kappa V\right)\right]=\epsilon\left[\hat{\mathbf{s}}\cdot\acute{\mathbf{g}}-\frac{\partial P}{\partial s}\right]+\\&\epsilon^2\left[V\Omega+\frac{\partial\left(n\Omega\right)}{\partial t}-\kappa n\hat{\mathbf{s}}\cdot\acute{\mathbf{g}}\right]-\epsilon^3\kappa n\left[V\Omega+\frac{\partial\left(n\Omega\right)}{\partial t}\right]\end{aligned} \tag{1.8}$$

- crossflow component of momentum equation:

$$\begin{aligned}&\mu^2\frac{\partial\langle v^2\rangle}{\partial n}+\epsilon\left[\hat{\mathbf{n}}\cdot\frac{\partial\mathbf{R}}{\partial t}\frac{\partial V}{\partial n}-\mu^2\kappa n\frac{\partial\langle v^2\rangle}{\partial n}+\kappa U\hat{\mathbf{s}}\cdot\frac{\partial\mathbf{R}}{\partial t}+\kappa U^2\right]+\\&+\epsilon^2\left[\frac{\partial V}{\partial t}-\kappa n\hat{\mathbf{n}}\cdot\frac{\partial\mathbf{R}}{\partial t}\frac{\partial V}{\partial n}+\frac{1}{2}\frac{\partial V^2}{\partial n}+\left(\hat{\mathbf{s}}\cdot\frac{\partial\mathbf{R}}{\partial t}+U\right)\frac{\partial V}{\partial s}-n\Omega\kappa U\right]\\&-\epsilon^3n\left[\kappa\frac{\partial V}{\partial t}+\kappa\frac{1}{2}\frac{\partial V^2}{\partial n}+\Omega\frac{\partial V}{\partial s}\right]=-\frac{\partial P}{\partial n}-\epsilon\left[U\Omega-\mathbf{n}\cdot\acute{\mathbf{g}}-\kappa n\frac{\partial P}{\partial n}\right]+\\&+\epsilon^2n\left[\Omega^2+\kappa U\Omega-\kappa\mathbf{n}\cdot\acute{\mathbf{g}}\right]-\epsilon^3\kappa n^2\Omega^2\end{aligned} \tag{1.9}$$

- turbulent kinetic energy equation:

$$\begin{aligned}&\hat{\mathbf{n}}\cdot\frac{\partial\mathbf{R}}{\partial t}\frac{\partial k}{\partial n}+\epsilon\left[\frac{\partial k}{\partial t}+\left(U+\hat{\mathbf{s}}\cdot\frac{\partial\mathbf{R}}{\partial t}\right)\frac{\partial k}{\partial s}+\left(V-2\kappa n\hat{\mathbf{n}}\cdot\frac{\partial\mathbf{R}}{\partial t}\right)\frac{\partial k}{\partial n}\right]-\epsilon^2n\left[2\kappa\frac{\partial k}{\partial t}+\right.\\&\left.\left(\kappa U+\kappa\hat{\mathbf{s}}\cdot\frac{\partial\mathbf{R}}{\partial t}+\Omega\right)\frac{\partial k}{\partial s}+\kappa\left(2V-\kappa\hat{\mathbf{n}}\cdot\frac{\partial\mathbf{R}}{\partial t}\right)\frac{\partial k}{\partial n}\right]-\epsilon^3\kappa n^2\left[\kappa\frac{\partial k}{\partial t}+\Omega\frac{\partial k}{\partial s}+\kappa V\frac{\partial k}{\partial n}\right]\\&=\mu\frac{\partial}{\partial n}\left(\nu_t\frac{\partial k}{\partial n}\right)-\langle uv\rangle\frac{\partial U}{\partial n}-\mu\varepsilon+\epsilon\left[2\kappa n\mu\frac{\partial}{\partial n}\left(\nu_t\frac{\partial k}{\partial n}\right)-\left(\langle u^2\rangle-\langle v^2\rangle\right)\frac{\partial V}{\partial n}\right.\\&\left.-2\langle uv\rangle\kappa n\frac{\partial U}{\partial n}+\langle uv\rangle\kappa U-2\kappa n\mu\varepsilon\right]+\epsilon^2\left[\mu\frac{\partial}{\partial s}\left(\nu_t\frac{\partial k}{\partial s}\right)+\kappa^2n^2\mu\frac{\partial}{\partial n}\left(\nu_t\frac{\partial k}{\partial n}\right)\right.\end{aligned}$$

$$-2\kappa n\left(\langle u^2\rangle-\langle v^2\rangle\right)\frac{\partial V}{\partial n}-\langle uv\rangle\left(\kappa^2 n^2\frac{\partial U}{\partial n}+\frac{\partial V}{\partial s}-\kappa^2 nU\right)-\kappa^2 n^2\mu\varepsilon\Bigg]+$$

$$\epsilon^3\kappa n\left[\kappa n\left(\langle u^2\rangle-\langle v^2\rangle\right)\frac{\partial V}{\partial n}+\langle uv\rangle\frac{\partial V}{\partial s}\right] \tag{1.10}$$

Finally, the following closure equations for the Reynold's stresses, were used:

$$\langle uv\rangle+\epsilon\kappa n\langle uv\rangle=\frac{\nu_t}{\mu}\frac{\partial U}{\partial n}+\epsilon\frac{\nu_t}{\mu}\kappa\left(U-n\frac{\partial U}{\partial n}\right)+\epsilon^2\frac{\nu_t}{\mu}\frac{\partial V}{\partial s} \tag{1.11}$$

$$\langle u^2\rangle=2C_1\kappa+\epsilon\frac{2\nu_t}{\mu}\frac{\partial V}{\partial n},\qquad \langle v^2\rangle=2C_3\kappa-\epsilon\frac{2\nu_t}{\mu}\frac{\partial V}{\partial n} \tag{1.12}$$

where ν_t is the eddy viscosity related to the turbulent kinetic energy and its rate of dissipation ε by:

$$\nu_t=C_\mu\frac{k^2}{\varepsilon} \tag{1.13}$$

while C_μ is a constant of the model and was found to be of order of $C_\mu\approx 0.09$. The rate of dissipation, instead, was related to the total thickness of the mixing turbulent layer and the kinetic energy:

$$\varepsilon=C_\varepsilon\frac{k^{3/2}}{b} \tag{1.14}$$

with $C_\varepsilon\approx 0.08$.
The above model, complete at the various orders of ϵ and μ, will be investigated in its $\mathcal{O}(1)$ form in the present work.
Experimental data from Misra et al. (2006) supported some of the findings and suggestions by Brocchini and co-workers. Further works by Brocchini and Misra, detailed in the following, helped clarify various aspects of the theoretical model under analysis, in order to gain information on turbulence inception at the leading edge of the breaker.
In Misra et al. (2004) the attention was focused on the importance of extra strain rates for the turbulent structure. According to the theoretical model, extra strain rate effects due to the geometric and streamline curvature, should be smaller than the simple shear strain rate. However, Misra et al. (2004) found, on the basis of data obtained from dedicated PIV experiments for an air-entraining weakly turbulent hydraulic jump that the effects of such terms are higher than the mean simple shear. Subsequently, Misra et al. (2006),

using the same data of Misra et al. (2004), attempted at explaining some of the dynamics entailed in the model of Brocchini (1996); Brocchini and Peregrine (2001a,b); Brocchini (2002). Particular attention was put in the description of: i) the mean flow profile within the single-phase turbulent layer and ii) the $O(1)$, in layer thickness, streamwise momentum equation. A good agreement was found between a cubic fit of the experimental velocity and the theoretical mean velocity. The latter is represented by a cubic polynomial, like in Madsen and Svendsen (1983) but with the difference that in the present case the coefficients of the cubic are functions of both time and streamwise coordinate s.
We close this Introduction by providing a short overview of the rest of the thesis. Chapter 2 of the present dissertation shown in detail an accurate laboratory experiments, using PIV technique. Chapter 3 focuses on an overall description of the dynamics of a breaker, specific focus being given to the geometry and kinematic characteristics of the breaker. Validation of the analytical model of Brocchini and co-workers, in particular the behaviour of the $\mathcal{O}(1)$ model, are shown in Chapter 4. Particular attention was also put in the extra strain induced by streamline curvature and on the study of the breaker like a flapping foil. Discussion and conclusion are presented in Chapter 5.

Chapter 2

Laboratory experiments

In previous experimental studies, a spilling breaker was analysed in similarity to either hydraulic jumps (Misra et al., 2008) or a hydrofoil-generated turbulent region (Battjes and Sakai, 1980; Duncan and Dimas, 1996; Mossa, 2008). In both cases a steady spilling breaker was generated and most often was characterized by a small curvature of the free surface with an almost vanishing local rotation. In particular, Misra et al. (2008) proposed an interesting study of a steady breaker (see Fig. 2.1) with good accuracy measurements of the statistical kinematic quantities. Thanks to the high repeatability of the phenomenon, they were able to define the characteristics of the air-water mixing layer and the kinematic quantities of the turbulent shear layer just below the turbulent free surface. Due to the realization of a large number of tests, an ensemble-average of the instantaneous velocity fields was done in order to evaluate the mean and turbulent flow structure. For example, analysing the vorticity, they found that the peak of vorticity is upstream the breaking location and in good agreement with the experimental results of Dabiri and Gharib (1997).

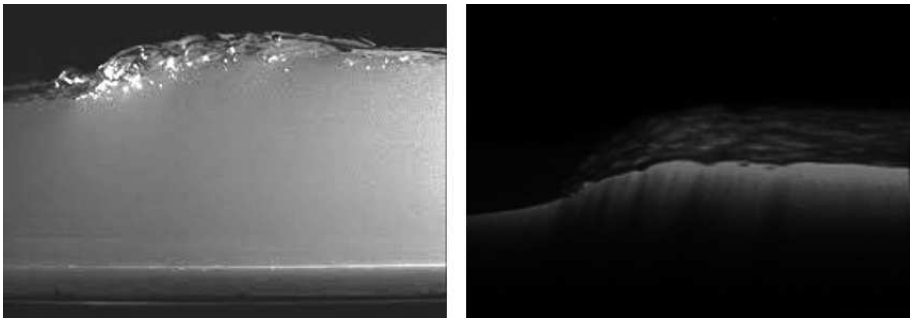

Figure 2.1: Hydraulic jump by Misra et al. (2008).

Using a conceptually different experiment, Duncan and Dimas (1996) proposed a steady breaking wave generated by a two-dimensional hydrofoil moving near the free surface with constant speed, angle attack and depth of submergence. They measured the mean and fluctuating shape of a breaking wave, the

surface ripples downstream of the breaker and the vertical distribution of vertical and horizontal velocity fluctuations at a single station behind the breaking wave (see Fig. 2.2). Similar studies were also proposed by Battjes and Sakai (1980) and Mossa (2008). In order to analyse the flow, using a hydrofoil, Battjes and Sakai (1980), observed that this solution enables the simulation of a breaker characterized by an unsteady first phase and a second phase when a quasi-steady bore is present, to which the results of a spilling type breaking downstream of a hydrofoil can be applied.
Mossa (2008) proposed an experimental work on a spiller produced by a hydrofoil positioned in a uniform current. The use of the Laser Doppler Anemometer technique, allowed to find two different regions downstream of the hydrofoil: (i) a flow field similar to a mixing layer, close to the breaking zone, and (ii) a flow field similar to a wake.
In this dissertation, we want to bring in some innovation related with both the

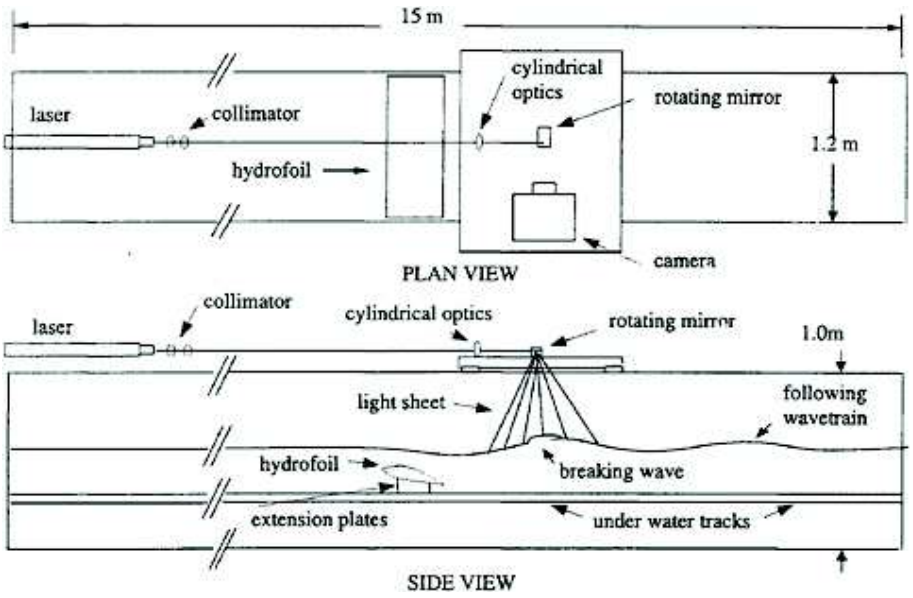

Figure 2.2: Schematic showing the configuration of the tank, carriage, optics and hydrofoil for photographing the breaker region. Adapted from Duncan and Dimas (1996).

generation mechanism of the breaker and the nature of observed phenomena. Being the aim of this work that of studying, with a very high temporal and spatial resolution and good repeatability, a rapidly-evolving spilling breaker, we have decided to resort to an impulsive generation of the breaker (see Fig. 2.3). Furthermore, the choice of a sloshing tank allows for a high repeatability of the phenomenon and a good accuracy of measurement. All these aspects are

detailed in the following and more details about the comparison between the results of a steady (previous literature studies) and unsteady breakers (current study) will be shown in the next chapter.

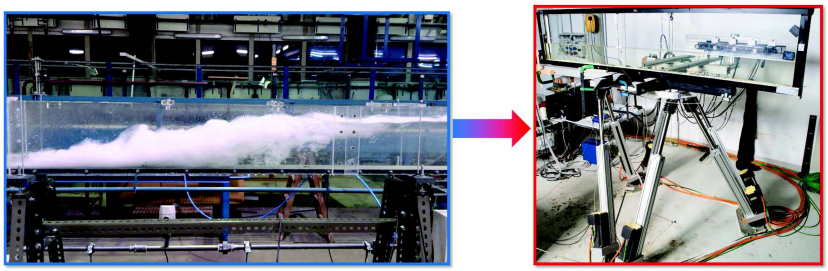

Figure 2.3: Left panel: a flume for the generation of a hydraulic jump. Right panel: Hexapode System for the generation of an unsteady spilling breaker.

2.1 PIV technique

Several methods for measuring the fluid velocity of phenomena of interest have been developed and in this case a Particle Image Velocimetry (PIV) technique was used.
The Particle Image Velocimetry is a branch of the Particle Image Technique and all use image analysis to measure velocity.
Common to all of them is that small particles are introduced in the flow and a camera captures images of the tracer particles as they follow the flow. The velocity field is, then, computed from an analysis of the images.
The image acquisition consists in the capture of the light scattered from the particles, its recording through a digital camera and its storage into a dedicated computer, used for all the needed analyses. There exist PIV systems that can measure a 3D velocity field, but for our work only a 2D velocity field is analysed.
Fig. 2.4 shows the principle at the base of the PIV. Using two different images, it is possible to evaluate the distance Δs of the seeding particles in the fluid that move during a time interval Δt. The velocity is, thus, evaluated as:

$$V = \frac{\Delta s}{\Delta t}$$

It is assumed that the tracer particles follow the flow and that the velocity

of the particle is equal to the velocity of the fluid. This only occurs for "non-massive particles", i.e. for particles with a very small Stokes number, i.e. $St < 1$ (see for example Soldati and Marchioli (2009)).

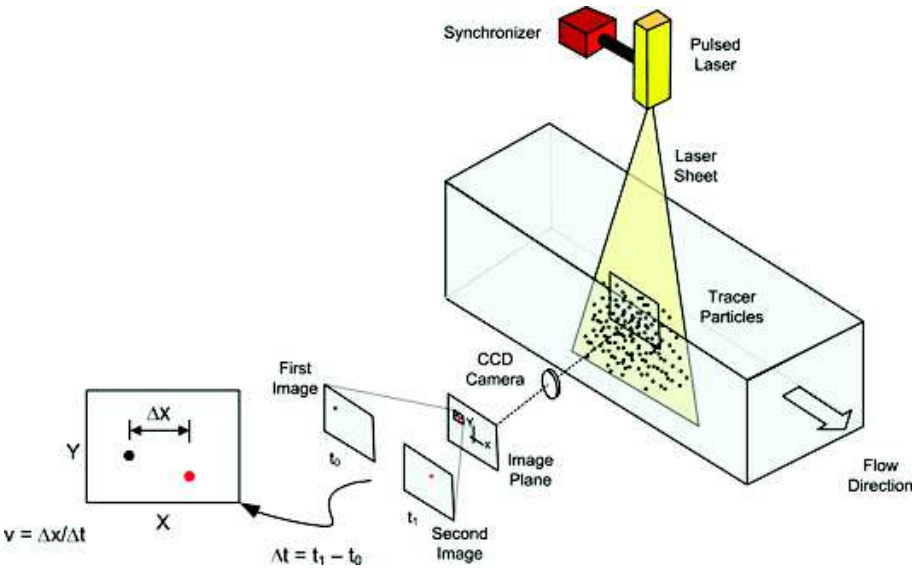

Figure 2.4: Example of the experimental arrangement for a PIV experiment.

The water volume is illuminated with a light source and one or more cameras are used to capture the fluid with the illuminated particles.
Δt is equal to the time between each light pulse and the cameras records the particles position for each light pulse. Δs is the distance between the position occupied by the same particle in two successive recordings.
Two different methods exist to record/analyse the image: auto-correlation and the cross-correlation (see Fig. 2.5). In the first case the camera, records multiple exposures of the same image, while in the second case the camera records two images with one exposure on each. In this work only the cross-correlation method is used (see Fig.2.6).

Even though the PIV is, in principle, a very simple method, its implementation and usage are not simple. A wide variety of parameters, such as particles diameter, light source, aperture and shutter speed, can influence the result.
The characteristics of the tracer particles, like the density, diameter and weight are very important because they can influence the performance of the PIV and, thus, the results. The choice of the particle diameter depends on the flow velocity. For high-speed flows (> 50 m/s), the particle diameter should not be larger than $0.5\mu m$, while for flows of about 1 m/s, the diameter of the particles could even be in the range $50 - 70\mu m$. The surface of the particles should

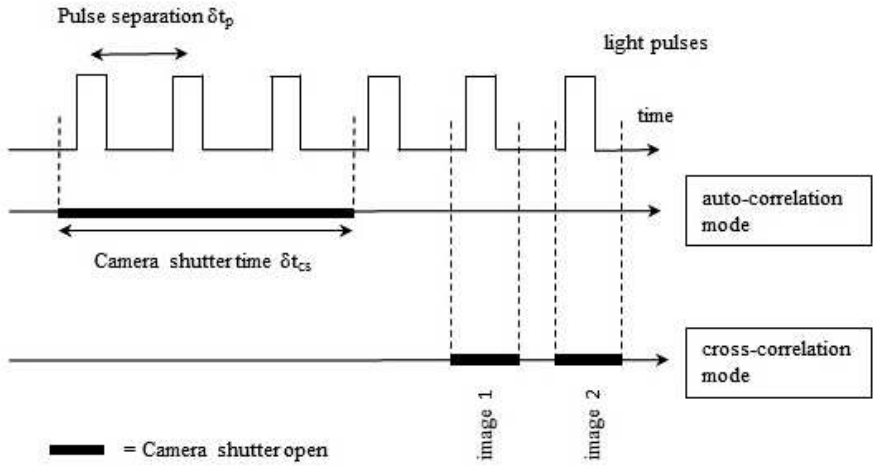

Figure 2.5: Recording mode in PIV.

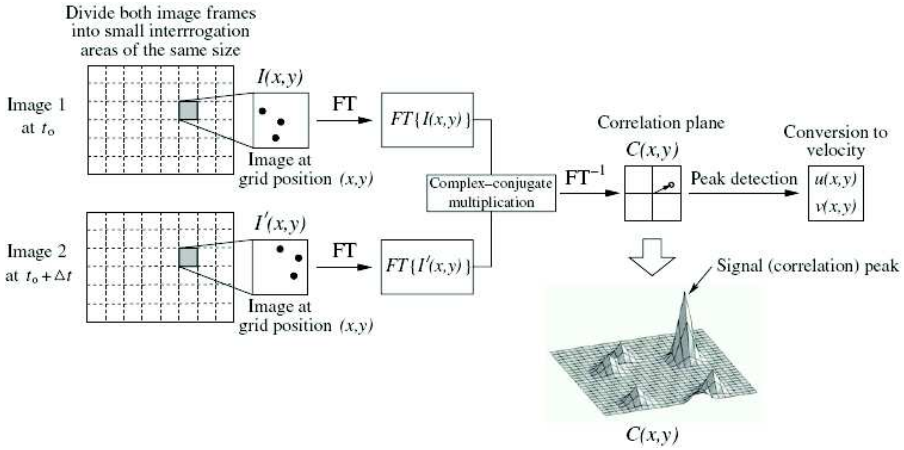

Figure 2.6: Cross-correlation mode: two images are recorded with only one laser pulse in each.

reflect enough light to be recorded by the camera. In this study hollow glass particles were used with an average diameter of about $10\mu m$. They offer a good scattering efficiency and a sufficiently small velocity lag. In most cases, like the present one, the mixing of the particles in the water is very important in order to get a homogeneous distribution.
The choice of the illuminating source is also very important because if inadequate, nothing will be measured. For the measurements of 2D velocity fields it is necessary to generate a 2D light sheet that must respect several requirements:

- the sheet must be pulsed at a prescribed frequency, because otherwise errors can occurs in the measurement of the velocity;
- the light intensity must be sufficiently high, because the light that each particle receives is only a part that will be scattered in the direction of the camera and such light must be sufficient to record it;
- the sheet must be thin in order to "filter out" unwanted 3D flows.

The most common instrument used in PIV for the generation of the light sheet is a laser, because it is able to concentrate the light in a narrow beam. In order to generate a light sheet, a cylindrical lens is used or a combination of this with a spherical lens. The laser beam has a Gaussian profile and the laser sheet intensity is variable. This can be a problem when a large area is to be illuminated. In the present study a combination of cylindrical and spherical lenses was used.
Important is also the optics. The resolution of the image acquisition process must be sufficient to resolve the position of each particle in the image. Two are the main resolution issues:

- spatial resolution, i.e. the number of pixels in the image;
- gray-scale resolution, i.e. each pixel records a grey-scale value. The gray scale resolution is the number of levels that each pixel is capable of resolving.
  A grey-scale value ranges from zero to one, representing zero density (black) and full density (white), respectively.

The accuracy of determination of the particle position increases with increasing resolution. In our experiments the grey-scale resolution was of 16 bit ($2^{16} = 65536$ levels) and the pixel number per mm was of about 9. This was evaluated as the relationship between the object size and the image size. This means that each pixel in the image is about $0.11mm^2$ in the physical scale. Since the seeding particles have a diameter of about $10\mu m$, this should yield a particle diameter in the image of $d_{pi} = 0.09$ px. This is sufficient to resolve the particles.

2.2 Design of the experiments

The experiments were conducted at the Sloshing Laboratory of CNR-INSEAN (Marine Technology Research Institute).
The spilling breaker was reproduced into a 3 m long, 0.6 m deep and 0.1 m wide

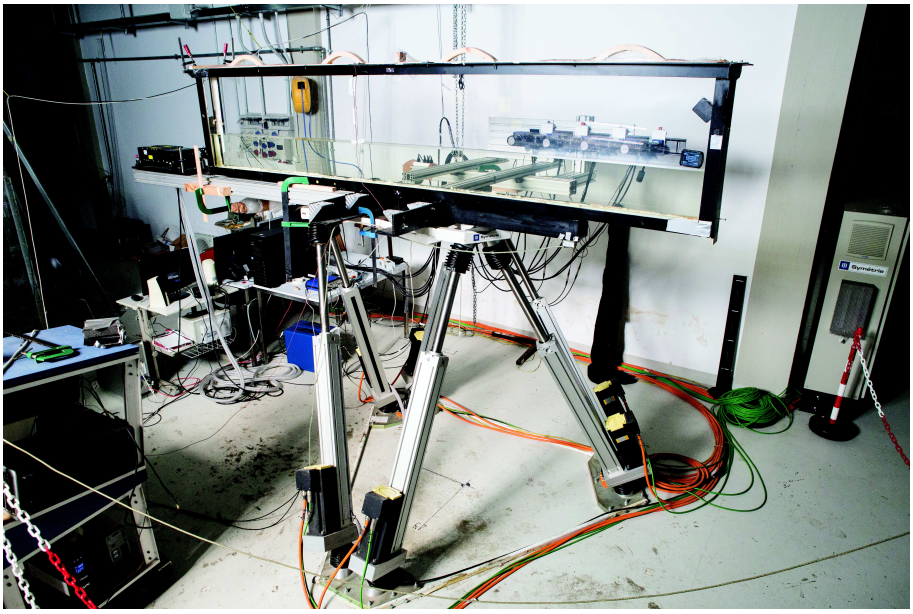

Figure 2.7: Hexapode System.

tank made of Plexiglass. A “Symetrie Mistral” Hexapode system was used to force the motion of the tank and ensured a high accuracy of the motion with a resolution of the order of 0.1 mm (see Fig. 2.7).

The design of the experiments at hand required the tackling of several challenges, first, a reliable measurement of the turbulent flow field, which characterizes the breaker in the region surrounding the wave crest, requires a statistical analysis, i.e. a large number of independent events, each given by a single run. The capability to generate a spilling breaker with high repeatability becomes, then, a crucial issue for the reliability of the statistical analysis. In similarity to previous studies on the evolution of breaking waves induced by shallow sloshing flows (Antuono et al., 2014; Lugni et al., 2014), a suitable spilling breaker was designed to evolve in a sloshing tank by means of a combination of numerical solutions. An efficient HPC (Harmonic Polynomials Cell) solver (Shao and Faltinsen, 2012, 2014), for the solution of a potential flow, was first used to reproduce the flow evolving in a 3 m long, 0.6 m deep and 0.1 m wide tank with a water depth of 0.2 m, where the temporal evolution of the free surface was evaluated in terms of fully Lagrangian, nonlinear kinematic and dynamic (free surface) boundary conditions. The results of the simulations enable the determination of the motion time history, velocity and acceleration of the tank. Because the HPC solver is extremely efficient and fourth-order accurate, i.e. requires a reduced computational time, it was used to check several time his-

tories on a grid with 81×10 stencils, in order to find the most suited for the generation of the gentle spilling breaker of our interest. However, HPC is a potential solver and, thus, it is unable to follow the complete evolution of the spilling breaker inside the tank. For this reason, the tank motion time history found with the HPC solver, was used to force the tank acceleration within a Navier-Stokes solver (Colicchio, 2004), second order accurate in space and time. This unable the estimation of the size region of interest for the measurement of the kinematic quantities. A convergence analysis on three grids was performed for the Navier-Stokes solution. The coarsest grid is 480×96 cells; the other two are two and three times finer than the first one.
To avoid vibrations and mechanical noise, the motion was generated as smoothly as possible, at least during the acquisition of the kinematic flow field. This is shown in Fig. 2.8, indicated by the red and blue line.
The wave breaker generation occurs within the first interval, i.e. for $0s \leq t \leq 1.195s$, denoted by the red dashed line. Then, from $t = t_1 = 1.195s$ up to $t = t_2 = 2.5s$ the tank moves with a constant velocity for the whole evolution of the breaker. Finally, the tank smoothly goes to its initial position.
The time history of the tank position, velocity and acceleration, for $0 \leq t \leq 4.0708$ is:

$$x(t) = A(1-\cos(\omega t))-0.335(t-t_1)+0.084-0.335\sin(t-t_2)-0.353 \quad (2.1)$$

$$v(t) = \omega A(\sin(\omega t))-0.335-0.335\cos(t-t_2) \quad (2.2)$$

$$a(t) = \omega^2 A(\cos(\omega t))+0.335\sin(t-t_2) \quad (2.3)$$

with:
$A = 0.075m$, the oscillation amplitude;
$\omega = 3.9517rad/s$, the angular velocity.
Obviously, the values of displacement, velocity and acceleration achieved with the above-mentioned equations, must fall within the motion limits of the Hexapode system, which are:

$R_x = \pm 0.47m$
$R_y = \pm 0.47m$
$v = 1m/s$
$a = 10m/s^2$

where R_x and R_y are the maximum displacements in the horizontal plane, v is velocity and a is the acceleration. Fig. 2.8 shows that these limits were respected.

Care was put in the realization of the breaking event during the first oscillation of the tank. According to Lugni et al. (2006, 2010a,b, 2014) the technique

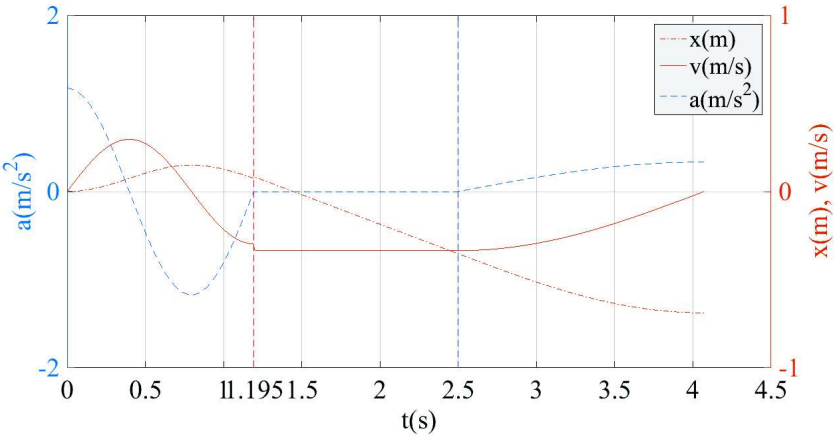

Figure 2.8: Time history of the motion (orange dash-dot line), velocity (orange continuous line) and acceleration (blue dashed line) of the tank.

in use allows for a high repeatability of the sloshing flows, where large nonlinear local effects can make the event highly chaotic in the successive cycles. Further, the capability to control the flow features during the first oscillation (mainly governed by the initial conditions) enables the realization of an unsteady, strongly nonlinear breaking event, i.e. close to the sought physical breaker.

Fig. 2.9 (left panel) shows that the HPC solver allows to follow the wave generation and the wave steepening up to the breaking onset; then the potential solution blows up. In order to estimate the size of the region of interest for the

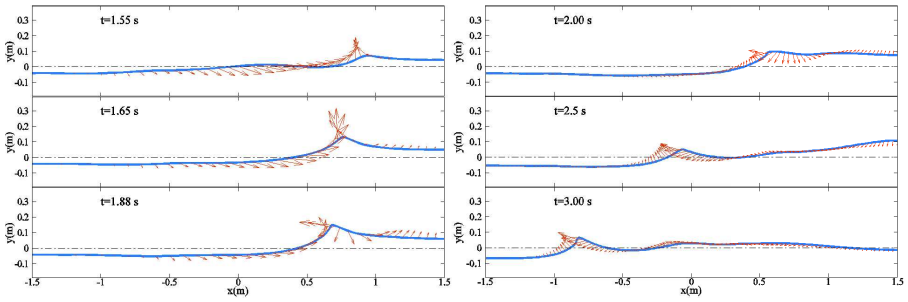

Figure 2.9: Evolution of the free surface before (left column: HPC solver) and after the breaker generation (right column: NS solver).

breaker evolution, the right column of Fig. 2.9, shows the free-surface configuration estimated by the Navier-Stokes solver. Although the latter one is used to reproduce the whole time history of the tank, the free surface deformation

until breaking onset is almost identical to the HPC solution and, therefore, is not shown. From these results we can estimate the size of the region where the breaker would initiate and evolve, this region having a length of about 1.80 m and a height variable according to the evolution of the breaker, but with a maximum extension of about 0.35 m. The large extent of the region of interest and the need to undertake detailed flow measurements with a good spatial and temporal resolution suitable to accurately resolve the evolution of the turbulent flow structures in the spilling breaker, required the implementation of an ad-hoc camera arrangement and acquisition strategies.

2.3 Repeatability analysis

The repeatability analysis is an activity essential to verify the accuracy of the present experimental study, whose results may also be used in future numerical investigations.
The tank motion designed by the HPC solver, was used in the laboratory to reproduce the phenomenon.
The repeatability of the global features was first assessed through the analysis of the recorded images, with particular attention to some geometrical parameters: horizontal position of the wave crest, horizontal position of the breaker toe and horizontal position of the tank.
The main reference geometrical point was the wave crest horizontal position. More in detail, a set of 32 runs of the same event were investigated. This was performed using a simplified configuration with two digital cameras (frame rate = 100 fps and resolution 1920×1088) and diffused light.
The repeatability analysis, based on the horizontal position of the wave crest, provides an error estimate within 10mm, which is of the same order of the camera resolution.
Figure 2.10 gives the horizontal position of the wave crest in time. The small size of the errorbars (red line and circles), confirms the high repeatability of the phenomenon at least until the occurrence of breaking (at $t \approx 0.6s$ and, therefore, the possibility to proceed to the definition of the experimental setup. Noticeable is the increase in the data scattering with the evolution of the wave from the onset of the breaking (between $t = 0.4s$ and $t = 0.6s$) up to the steady-state condition. The reduced repeatability might be associated with the return flow in the crest region, which should characterize the evolution of the average velocity field of a breaker.

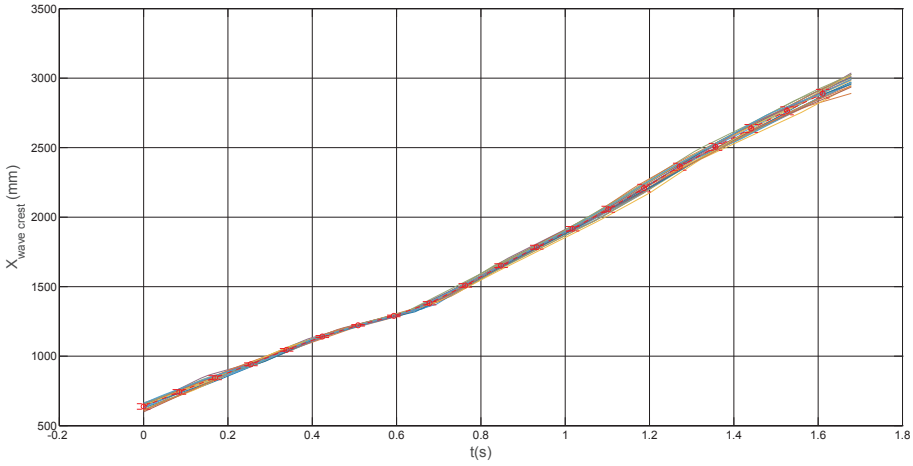

Figure 2.10: Horizontal position of the wave crest (mm).

2.4 Experimental setup

A 2-D Particle Image Velocimetry was used for the measurement of the instantaneous velocity field. The water depth was of 0.20 m and it was seeded with hollow glass particles of a mean diameter of about 10 μm. As previously mentioned, the large extension of the region of interest, suggested to divide this area into two different zones, in order to reach a good spatial and temporal resolution as shown in Fig. 2.11 (bottom). For each zone a multi-camera simultaneous recoding system with 4 cameras arranged side by side was used to acquire a large flow extent at a spatial resolution, adequate to resolve flow eddies as small as 2mm. With this arrangement, the field of view of the camera system allowed us to cover about half of the region of interest and, thus, created the need to split it in two regions. Namely:

- an upstream region, indicated with the black rectangles in the bottom panel of Fig. 2.11, which covers the formation and evolution of the breaker until an almost steady state is reached. As a consequence, the evolution of the wave profile required to arrange the cameras at different vertical positions. This was achieved inclining the cameras by 7 deg in the vertical plane (see image A of Fig. 2.11).

- a downstream region, indicated by the red rectangles in the bottom panel of Fig. 2.11, which covers the rest of the breaker evolution.

The 4 cameras used for the PIV image recording were Imager sCMOS models by LaVision (i.e. 16 bits, 2560 $\times$ 2160 pixel resolution, 6.5 μm pixel size, 50 frames/s maximum frame rate). Each camera was equipped with a 50 mm

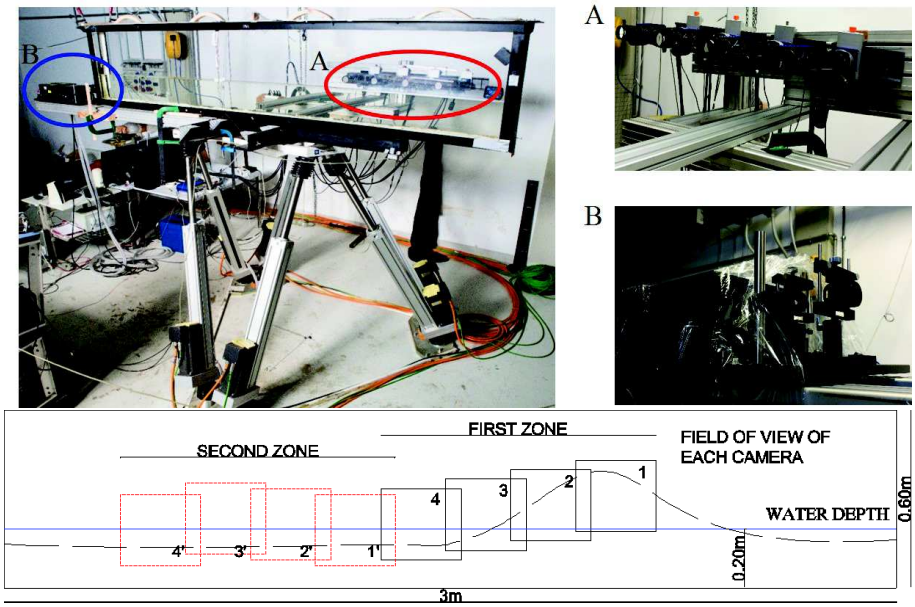

Figure 2.11: Experimental set-up: Exapode System, tank, laser and cameras (top-left panel); cameras in the upstream region inclined by 7 deg in the vertical plane (top-right panel, image A) and laser with cylindrical and spherical lenses (top-right panel, image B); region of interest for the PIV measurements (bottom panel).

lens and positioned at the distance of 800 mm from the laser sheet, pointing normally to the laser sheet itself. It gave a magnification factor of about 9 pix/mm that allow to evaluate the relative overlapping between two subsequent Fields of View of the cameras. The illumination was provided by a double cavity Nd-Yag laser (2×200 mJ/pulse @ 12.5 Hz by Quantel) positioned on the sidewall of the tank. In this way, the laser sheet crosses the whole body of the wave before meeting the air phase. The laser beam was expanded through a set of one cylindrical (i.e. -15mm focal length) and one spherical (i.e. 1000 mm focal length) lenses to obtain an illumination domain extended over the whole region of interest and 1mm thick (see Fig. 2.11, Image B).
A frame rate of 8 fps is the maximum value compatible between the laser source frequency and the camera frame rate. In order to increase the frame rate from 8 to 16 fps, the laser trigger was shifted by $1/2dt$, where dt is the sampling period of the PIV system. This implies that the PIV snapshots were recorded at the instants $t_i = t_0 + idt$ during the first phase and at $t_i = t_0 + 0.5dt + idt$ during the second phase, with $i = 1, \ldots, T/dt$, and T indicating the total acquisition time. In particular, the sampling period dt was $1/8s$ and the acquisition time was

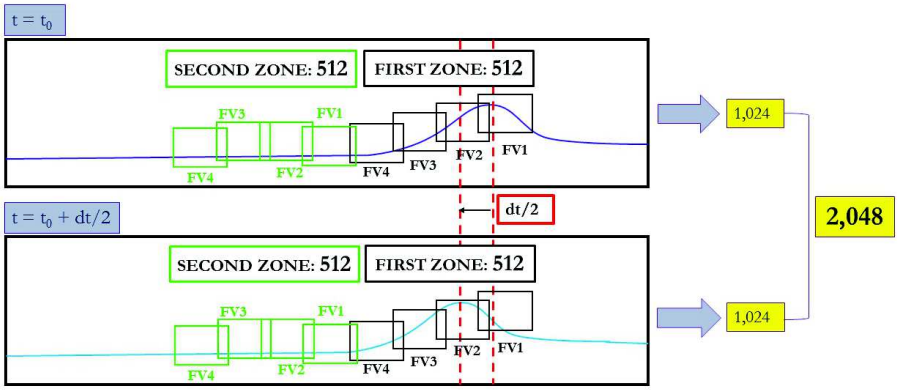

Figure 2.12: Schematic representation of the two different temporal configuration of cameras recording.

$T = 1.5sec$. The value of dt was found by the simple relation: $\Delta x/V$ where $V(1.2m/s)$ is the wave crest velocity evaluated by the NS solver simulation and Δx (10 pixel) are the pixel corresponding to 1 cm and calculated through the magnification factor. For each zone of each temporal configuration 512 realizations were run, for a total number of 1,024 realizations. Considering both temporal configurations, 2,048 realizations were run (see Fig. 2.12).

For the whole experimental campaign, the PIV images were processed by the La Vision software DaVIS 8.2, which uses a multi-pass cross-correlation image algorithm with windows deformation (Scarano, 2002). PIV images were pre-processed masking the image region over the water surface and subtracting the minimum background value. The final size of the interrogation windows was 24 × 24 pixels with an overlap of 75%.
The the range of velocities that can be measured, with this spatial discretization, goes from a minimum of $9cm/s$ to a maximum value of $1.5m/s$. The subimage within the interrogation window was then cross correlated with the corresponding subimage in the subsequent image. The position of the peak in the cross correlation result provides a measure of the displacement of the structure in the second subimage with respect to the first. In this way, an accurate estimation of the instantaneous velocity field was achieved and the large number of repetitions has supported an accurate statistical analysis, which is very important for the characterization of the flow structure.
This aspect will be analysed in detail in the next chapter.

Chapter 3

Problem phenomenology

The dataset made available by the experimental investigation described in the previous chapter allows for useful insight both in the overall dynamics of the breaker and in the details of dynamics of the single-phase, turbulent layer of the model of Brocchini (1996).
The present chapter aims at characterizing the main flow features of our sloshing-breaker, also with reference to similar available literature on hydraulic jump and spilling breakers. Specific emphasis is put in highlighting the differences between dynamics of a steady breaker, like an hydraulic jump, and a rapidly-evolving breaker, like the breaker of interest here.
Hence, the following aspects are investigated in detail: i) the near-surface breaker topology, ii) the injection/generation of vorticity at the free surface, iii) the overall turbulent kinetic energy field and the detection of the single-phase turbulent region, iv) the geometry of the single-phase turbulent region.
Maps of each quantity of interest are superposed to the related underlying flow image and, both, are the result of the mean of 512 realizations. The statistical data have been cropped with a numerical mask, applying a grey scale filtering, in order to remove the from the image the air-water mixing regions.
As mentioned in Chapter 2, we only focus on the first zone (see Fig. 2.12) where the flow is characterized by the highest curvature and rotation. These, clearly, highlight the non-stationarity of the phenomenon, confirmed by Peregrine's criterion (Peregrine, 1992): comparing the time needed for the crest deformation, about 0.65s, to the time needed for a particle to cross in the streamwise direction the single-phase turbulent region, about 0.75 s, we find the fairly rapid crest deformation typical of an unsteady breaker.

3.1 Overall evolution

A first question may arise about the mechanism here used to generate a repeatable breaking event: sloshing flow is not commonly adopted to induce a breaker. However, it is recognized as the onset and the evolution of a breaker is almost independent of the physical mechanism used to generate it. Slosh-

ing flow in tank was successful to get high repeatable wave event during the first cycles of oscillation of the tank (Lugni et al., 2006, 2010b,a, 2014; Abrahamsen, 2011). The capability to ensure high repeatability in the wave body approaching the breaking condition is essential for the following reasons:

i) the flow evolution close to the air-water interface can be properly studied within a statistical approach in the ensemble domain, which enables a reliable interpretation of the turbulent flow at the interface;

ii) the measured dataset is certified for validation and verification of numerical solvers.

These arguments motivated the proper design of the tank motion (see § 2) in order to realize an unsteady spilling breaker during the first tank oscillation. Fig. 3.1 shows the global scenario during the generation and evolution of the event. The time increases from top to bottom and from right to left; top image corresponds to $t = 1.64$ s, bottom to $t = 2$ s, with $t = 0$ identifying the start of the tank motion ($t = 0$); a time step $\Delta t = 0.04$ s between two consecutive images has been chosen. During the first 4 instants (Fig.3.1), the tank moves leftward with constant speed and zero acceleration (linear motion, see Fig. 2.8). The wave profile moves in the same direction of the tank and the local wave steepness increases. Initiated by the tank motion, i.e. the right wall pushes the water (first two images), this is further emphasized by the crest slowdown Barthelemy et al. (2015). The latter, indeed, causes some energy transfer from kinetic (i.e. the velocity is decreasing) to potential inducing an increase of the wave height and, then, of the wave steepness. According to the linear wave theory, this mechanism could continue to really small slowdown values; however, because of the nonlinear wave dispersion, the crest slowdown decreases (Fedele (2014a) for linear narrowband waves) causing a limiting wave steepness and then leading the wave crest to break. In our case the breaker is identified by a whitecap, that is a two-phase flow (see air-water mixture starting at $t = 1.72$s) in the wave front. Note that this is the easiest criteria to visually identify the occurrence of a breaker from global images of the phenomenon.
Although at this stage we refer just at a sequence of images, i.e. no local geometrical measurements are given, we can qualitatively observe as the local curvature at the crest increases until $t = 1.8$ s (see fifth panel from top to bottom in Fig. 3.1) and, then, progressively decreases to reach an almost steady value at $t = 1.92$ s (see third panel from bottom to top of Fig. 3.1).

A second question concerns the scaling of the phenomenon, which is strictly related to the sloshing flow existing in the tank. Several sloshing scenarios are identified in literature (Colagrossi et al., 2004; Bouscasse et al., 2013; Faltinsen and Timokha, 2009); they depends on the filling depth h_0 and on the nondimensional forcing period T/T_0 (nondimensionalized with respect to the largest

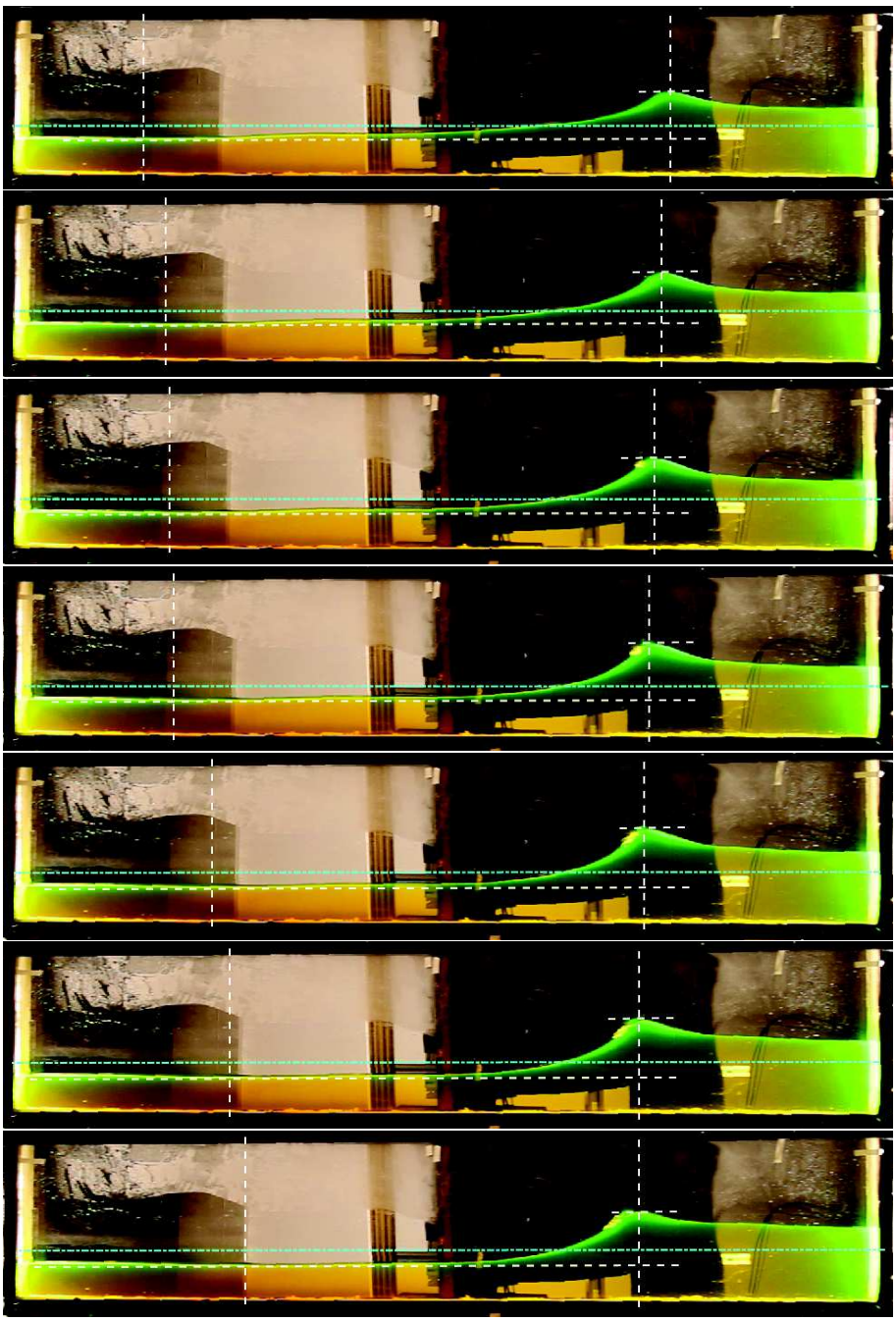

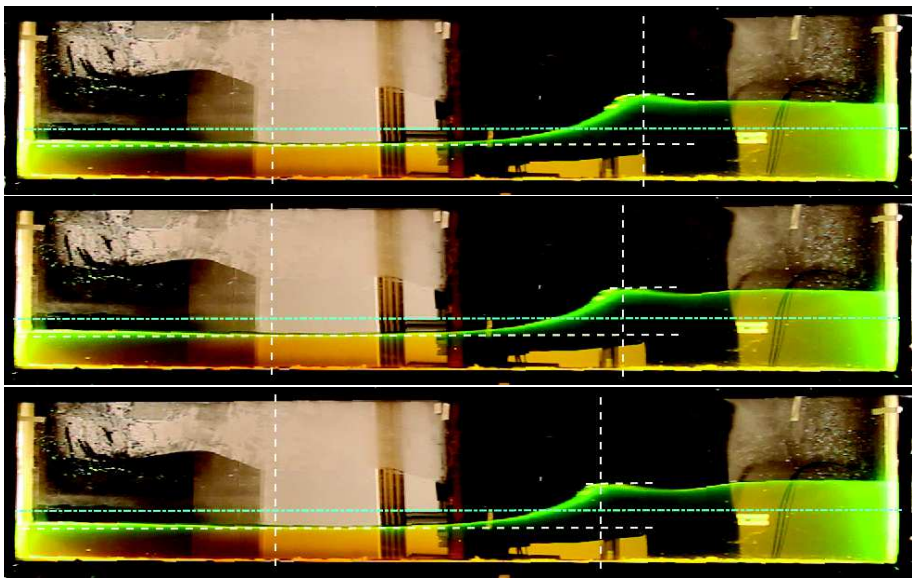

Figure 3.1: Image sequence of the generation and evolution of the spilling breaker in the sloshing tank. The time increases from top to bottom with a time step of $1/25s$.

natural period T_0 of the tank). In particular for shallow water condition, i.e. for $d/L \leq 0.1$, an unsteady breaker evolving to a steady breaker is commonly identified for $T/T_0 \simeq 1$ Bouscasse et al. (2013). In the present case, the motion of the tank is not explicitly excited at a period close to $T_0 = 4.3$ s; then we cannot a priori assess that the breaker is in shallow water condition.

To better understand the flow conditions governing the evolution of the prescribed event, Fig. 3.2 shows the time history of the wave steepness, wave height and wavelength measured from the images shown in Fig. 3.1. Fig. 3.3 shows the definition of the measured geometrical quantities, as well as the comparison with the free-surface configuration achieved from the numerical solver used in § 2 to design the experiment. The wavelength is estimated as twice the horizontal distance between the maximum and the minimum elevation of the free surface (see vertical, white dashed lines in Fig. 3.1); wave height is the vertical distance between the some points (see horizontal, white dashed lines in Fig. 3.1).

According to the above observations, Fig. 3.2 confirms the growth of the wave height until $t = t_1 + 0.16$ s $= 1.8$ s, then it decreases. Conversely, the wavelength decreases almost linearly; this behaviour causes an increase of the wave steepness ($kH/2$) until the breaker occurrence($t = 1.84$ s); then it keeps constant around a value $0.23 - 0.25$. The wavelength varying between 2 and 3.6

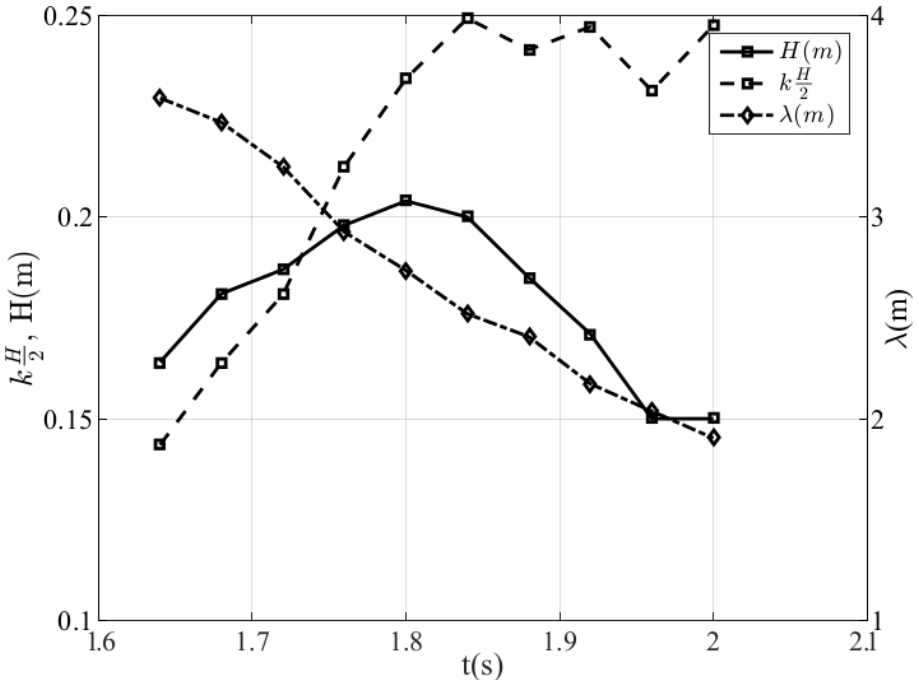

Figure 3.2: Evolution of the wave steepness, wave height and wavelength in time where $t_1 = 1.64$ s is the time of the first image with respect to the starting of the tank motion.

m, i.e. $h_0/\lambda < 0.1$, indicates that shallow water condition governs the flow evolution in the tank.

This is further confirmed by the instantaneous period dominating the flow, shown in Fig. 3.4, and calculated through the wavelet analysis of the wave elevation at 5 cm from the right (left panel) and left wall (right panel) of the tank, respectively. First (dash-dotted line), second (dotted line) and third (dashed line) natural sloshing periods are also indicated.

The wave period that governs the flow evolution is almost equal to the largest natural period T_0 of the tank. This means that the corresponding wavelength is twice the length of the tank, that is $h_0/\lambda < 0.1$. Noticeable is the larger variation of the energy level around the sloshing natural period for $t > 2.5s$. This seems to be associated to the thickening of the turbulent flow as the breaker approaches a steady condition. However, to definitely assess the occurrence of shallow water condition, circle symbols in Fig. 3.5 shows the ratio H/h_0 as function of λ/h_0 during the experimental evolution of the breaker from $t = 1.64$ s to $t = 2$ s. Several limiting curves are also reported. Continuous line represents the limiting curve for the application of cnoidal wave, i.e. $Ur = H\lambda^2/h_0^3 > 40$, while for lower values Stokes theory should be used.

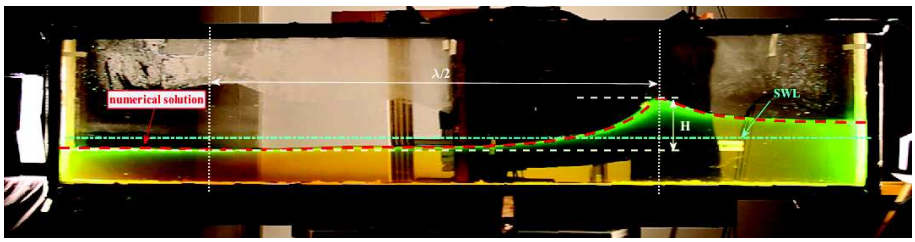

Figure 3.3: Definition of the geometrical quantities measured from the image analysis. Red dashed line represents the free-surface configuration calculated through the numerical solver used in the design of the experimental tank motion.

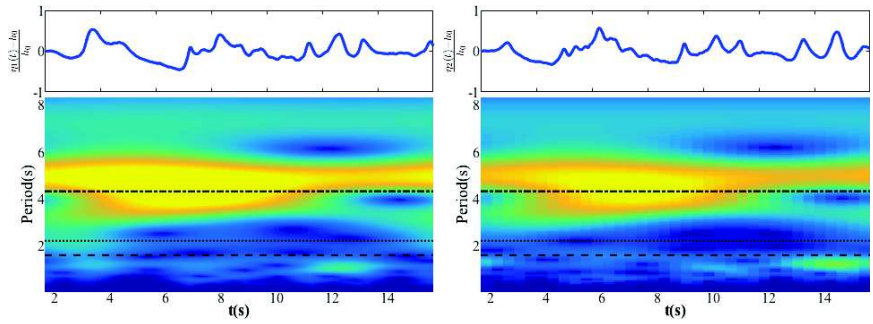

Figure 3.4: Time evolution of the wave elevation (blue lines) and corresponding wavelet analysis in two probes at 5 cm from the right wall (left panel), and at 5 cm from the left wall (right panel) of the tank, respectively. $t_1 = 1.64$ s is the time of the first image with respect to the starting of the tank motion.

The dash-dotted line indicates the highest waves determined by computational studies according to the results of Williams (1981). The dotted line bounds the deep-water breaking limit, while the dashed line is the corresponding limit in shallow water. The present experimental data are, at least after the onset of the breaking, larger than the shallow-water breaking limit, and in any case, larger than the shallow-water limit $\lambda/h_0 = 10$. Then, shallow water conditions can be definitely assumed, which implies that the still water level h_0 can be taken as suitable reference length scale. The time scale is $T = \sqrt{h_0/g}$ with g indicating the gravity acceleration, therefore in the following the dimensionless time $t^* = t\sqrt{g/h_0}$ is used. At this point we are able to make dimensionless the evolution of the wave height and wavelength. This is shown in Fig. 3.6, where starred symbols give dimensionless variables. A last question arises about the possible influence of the capillary waves on the onset of the breaker and on its successive evolution. Although the observation of the images does not empha-

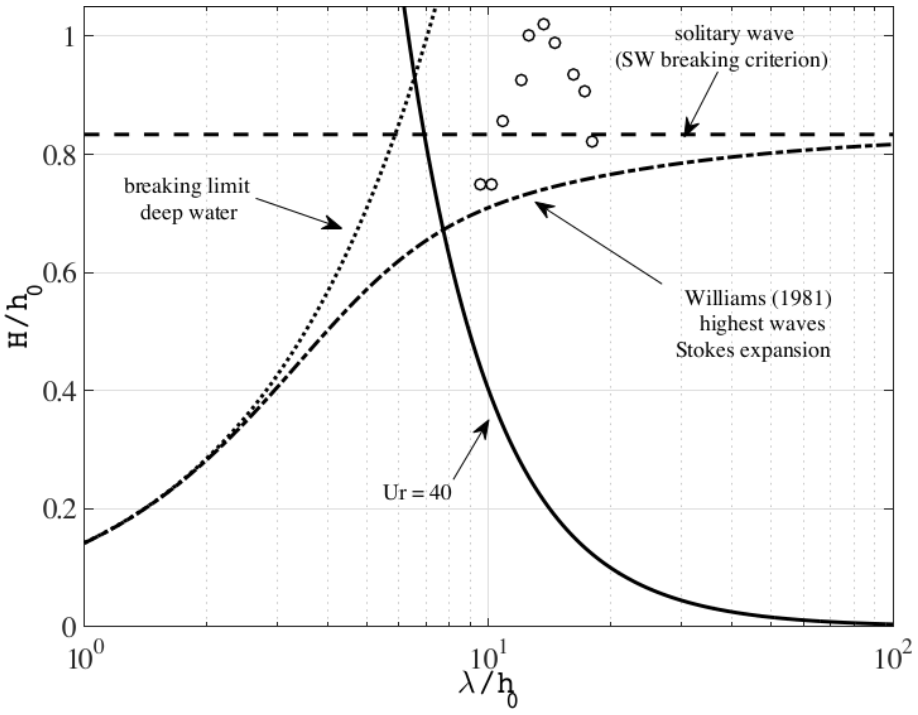

Figure 3.5: Literature limiting curves and our experimental data (empty circles).

size the occurrence of capillary waves at the forward face of the crest, in the following a more physically-oriented analysis is done. This bears on the fact that the radius of curvature in the crest region is large and, consequently its curvature is small. This implies that surface tension effects are negligible and do not influence the breaking process.

In Fig. 3.2 local measurements from the wave images were done in order to estimate the geometrical parameters of the wave: wave steepness ($kH/2$), wave height (H), wavelength (λ). They enable the estimation of the Bond number (Bo):

$$Bo = \frac{\Delta\rho g}{\gamma k^2}$$

where $\Delta\rho$ the density difference between water and air, γ the water surface tension and k the wave number. It measures the importance of the surface tension with respect to the buoyancy effects. Moreover, table 3.1, summarises the main wave geometric characteristics of the wave in both dimensional and dimensionless form:

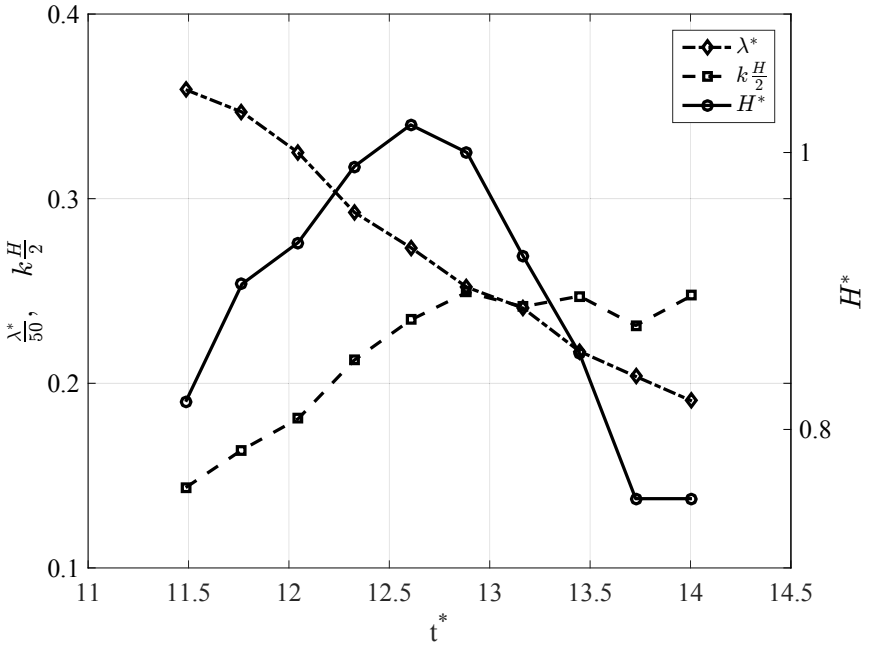

Figure 3.6: Dimensionless time evolution of the wave steepness, wave height and wavelength. The latter one is scaled by a factor 50.

$t(image)$	$H(m)$	$\lambda(m)$	$kH/2$	Bo	t^*	H^*	λ^*
1.64 s	0.1646	3.6013	0.1435	44137	11.486	0.823	18.0065
1.68 s	0.1812	3.4724	0.1639	41035	11.766	0.906	17.362
1.72 s	0.1870	3.2621	0.18	36215	12.046	0.935	16.310
1.76 s	0.1979	2.923	0.2126	29078	12.326	0.989	14.615
1.80 s	0.2042	2.7362	0.2343	25480	12.606	1.021	13.681
1.84 s	0.2000	2.512	0.25	21475	12.886	1.000	12.56
1.88 s	0.1854	2.4108	0.2415	19780	13.167	0.927	12.054
1.92 s	0.1708	2.1699	0.2472	16025	13.447	0.854	10.849
1.96 s	0.1500	2.0363	0.2313	14112	13.727	0.750	10.181
2.00 s	0.1500	1.903	0.2475	12325	14.007	0.750	9.515

Table 3.1: Temporal evolution of the main geometrical characteristics of the wave in dimensional and dimensionless form.

The measured wavelengths in the present study are much larger than the typical wavelength of capillary waves, that is $\mathcal{O}(\infty)$ cm; the same for the Bond number ($Bo \gg 100$).
These two parameters confirm that surface tension does not influence the breaking process investigated.
Fig. 3.7 summarises the results the of the DNS numerical study performed by Deike et al. (2015) to characterize the breaking regimes and the possible influence of the capillary waves. In this figure, the experimental results existing in literature and detailed in the table of Fig. 3.8 are also reported.

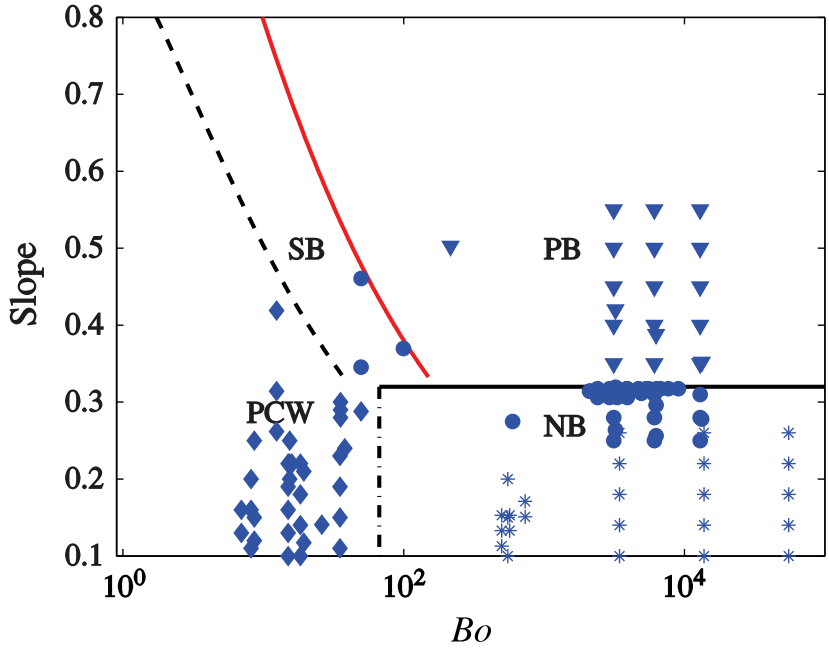

Figure 3.7: Wave state diagram, compares the regimes obtained through the simulation. (Adapted from Deike et al. (2015). Slope means wave steepness).

Symbols represent the results of the experimental data existing in literature, lines indicate the boundaries of the wave breaking regimes identified through the DNS simulations. They are: PB zone, which represents the plunging breaker regime; SB zone, which is the spilling breaker area; PCW zone which indicates the presence of parasitic capillary waves and NB zone which is the non-breaking gravity wave region. The red line is the limiting curve between plunging and spilling breakers. The horizontal solid line (black line), coincident with the critical steepness $kH/2 = 0.32$ line, is the boundary between non breaking and plunging breakers. It is coincident also with the numeri-

cal occurrence of spilling breaker, i.e. it is an extension of the red line. The black dashed line bounds the region between spilling and parasitic capillary waves. Finally, the dot-dashed line at $Bo = 67$, is the critical Bond number for the appearence of parasitic capillaries. The consistent quantity of filled circles around $kH/2 = 0.32$, even in the NB region testifies the presence of experimental data available in literature with the occurrence of spilling breaker generated with different physical mechanisms. This is in reasonable agreement with our data: breaking evolution occurs for a steepness ranging from 0.18 to 0.25 and a Bond number around or larger than 10^4. Results very similar were achieved from Tulin and Waseda (1999) (see stars in Fig. 3.5).

Reference	Wave type	λ (m)	Bo	Slope (ak)	Re	Generation	Measurement
Rapp & Melville (1990)	Plunger	1–2	3000–12 000	0.35–0.55	3–9 × 10^6	Wave maker	Camera & wave gauges
—	Spiller	1–2	—	0.25–0.32	—	—	—
Drazen *et al.* (2008)	Plunger	1–2	3000–12 000	0.35–0.55	3–9 × 10^6	Wave maker	Camera & wave gauges
Duncan *et al.* (1999)	Spiller	0.77	2105	0.31	2 × 10^6	Wave maker	Camera
—	Spiller	1.18	5000	0.31	4 × 10^6	—	—
Duncan (2001)	Spiller	0.41	600	0.275	8 × 10^5	Wave maker	Camera
Liu & Duncan (2003, 2006)	Spiller	0.4–0.65	1000–1750	0.317	8–16 × 10^5	Wave maker	Camera
Fedorov *et al.* (1998)	PCW	0.1	35	0.28, 0.29, 0.33	10 × 10^4	Wave maker	Wave gauges
—	PCW	0.07	15	0.2, 0.22, 0.25	5.8 × 10^4	—	—
—	PCW	0.05	8	0.11, 0.16, 0.2	3.5 × 10^4	—	—
Caulliez (2013)	Spiller	0.12, 0.17	50, 100	0.34, 0.37	13, 22 × 10^4	Wind	Camera
—	PCW	0.05–0.12	9–50	0.26–0.42	3.5, 13 × 10^4	—	—
—	Plunger	0.25	215	0.5	39 × 10^4	—	—
Zhang (1995)	PCW	0.075, 0.05	19, 9	0.21, 0.25	3.5, 6 × 10^4	Wind	Camera
Perlin *et al.* (1993)	PCW	0.068, 0.105	16, 38	0.22, 0.24	3.5, 10 × 10^4	Wave maker	Camera
Jiang *et al.* (1999)	PCW	0.101	35	0.11–0.25	10 × 10^4	Wave maker	Camera
—	PCW	0.073	18	0.08–0.22	6 × 10^4	—	—
—	PCW	0.066	15	0.1–0.21	5 × 10^4	—	—
—	PCW	0.05	8.6	0.03–0.15	3.5 × 10^4	—	—
—	PCW	0.045	7	0.13–0.16	3 × 10^4	—	—
Banner & Peirson (2007)	Breakers (MI)	0.38–0.46 m	500–766	0.11–0.17	3–9 × 10^6	Wave maker	Wave gauges
Tulin & Waseda (1999)	Breakers (MI)	0.4–4	500–50 000	0.1–0.3	0.8–20 × 10^6	Wave maker	Wave gauges

Figure 3.8: Experimental parameters of observed parasistic capillary waves, spilling and plunging breakers observed in the literature. Adapted from Deike et al. (2015)

3.1.1 Onset of the breaker

Several researchers investigated the wave evolution in the stage preceding the occurrence of the breaker in order to identify the ultimate condition leading the wave to break. Different criteria have been proposed, based on geometric, kinematic and energetic considerations, as already discussed in section (1.1). Recently a new criterion for the breaker onset (Fig. 3.1, 1^{st} frame), have been proposed by Prof. Banner group (Barthelemy et al., 2015), based on the following insight: "*the onset of the breaker occurs when the wave crest celerity reveals a deceleration*". Through an extensive numerical investigation, authors found that the irreversible condition for the breaker occurs when the ratio between flux energy speed (i.e. the ratio between the local energy flux and the

local energy density) and the local crest velocity c is larger than a threshold value. This is the *dynamical breaking parameter* B; it coincides with the u/c ratio on the free surface, as u the particle velocity. They found that the onset of the breaking occurs for $B = 0.84$. Although this criterion is based on a physical insight, previous work of Fedele (2014a), Fedele (2014b) shows that the wave crest steepens as the onset of the breaking is approached. This causes a crest slowdown due to the nonlinear dispersive effects. Preliminary studies (Fedele, Personal communication) show that the gentle focusing wave crests slow down more than steeper crests (see also Fedele (2014a), Fedele (2014b)). This causes the threshold $B = 0.84$ is attained faster as wave crest steepens; the associated particle speed u increases as the focusing point is attained.
During a recent symposium, Prof Banner invited us to verify the criterion and in particular the *wave crest slowdown* insight. Although the large time step used in the PIV analysis (i.e. $dt = 1/16s$) does not allow a time resolved estimation of the wave crest speed, we have used the images from a digital camera with 25 fps and spatial resolution $1920 \times 1088px$, relatively to the evolution of the whole tank, to evaluate the wave crest slowdown. To do that, from the images we measured the horizontal wave crest position, as shown in Fig. 3.9 (top panel): dashed line represents the average value of the horizontal position of the wave crest determined through the 7 repetitions of the same run; the corresponding standard deviation is represented by the errorbar. Because the measurement was done manually, an under sampling technique was used to reduce the effort; this means 8 fps, i.e. $0.125s$ as time step. This preliminary analysis enables an estimation of the wave crest celerity, whose results are reported in the bottom panel of Fig. 3.9; a minimum value occurs around $t^* = 13$. The large dt used does not ensure an accurate evaluation of the wave crest speed. Then, we increase the time resolution (frame by frame, i.e. dt = 0.04 s) in a window around the predetermined minimum value and, however, around the time instant of the frame where, for the first time, we observed a whitecap event. Note that at this stage, because of the global images available, the whitecap is the only criterion to be used for the breaker occurrence. The videos of two different runs were analysed and the results are shown in the top panel of Fig. 3.9 by means of the green and blue symbols. Such measurement is within the errorbar of the previous one obtained as the mean of 7 runs, testifying the repeatability of the phenomenon. However, by looking at the horizontal component of the velocity of the wave crest (i.e. time derivative of the horizontal position) reported on the bottom panel of Fig. 3.9 (green and blue symbols), we observe significant deviations from the red line. In particular, the minimum value of the horizontal component of the crest celerity, corresponds to the instant $t^* = 12.046$, i.e at the onset of breaking.

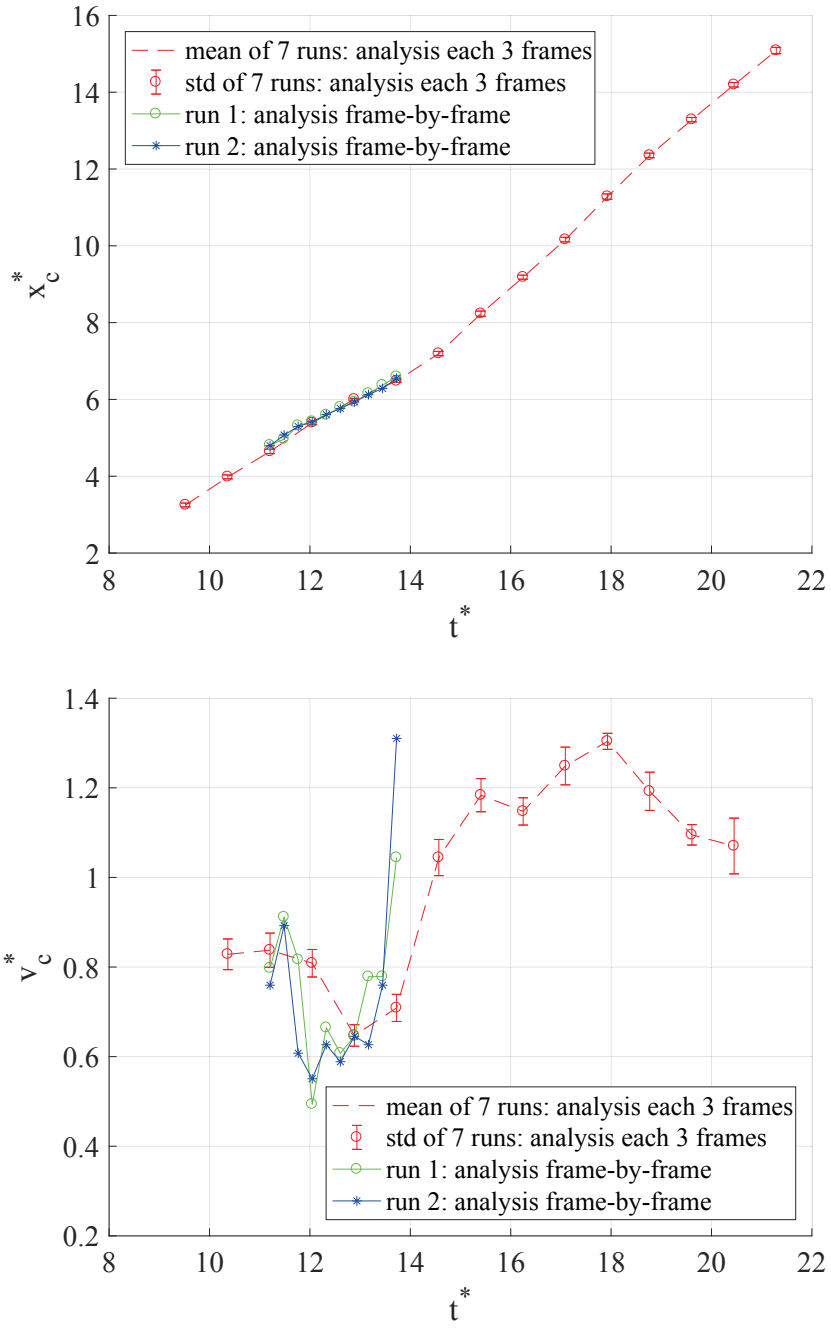

Figure 3.9: Evolution of the wave toe displacement (top panel), Velocity of the wave crest (bottom panel).

Moreover, according to Barthelemy et al. (2015), breaking onset commences when the breaking crest "whitecap" commences at a significantly lower initial velocity than expected. The images shown in Fig. 3.10, support their observation: first image, at $t^* = 11.77$, shows the free surface configuration just before the inception of the breaker; $t^* = 12.046$ is the instant when the celerity assumes the minimum value; $t^* = 12.32$ represents the following instant.

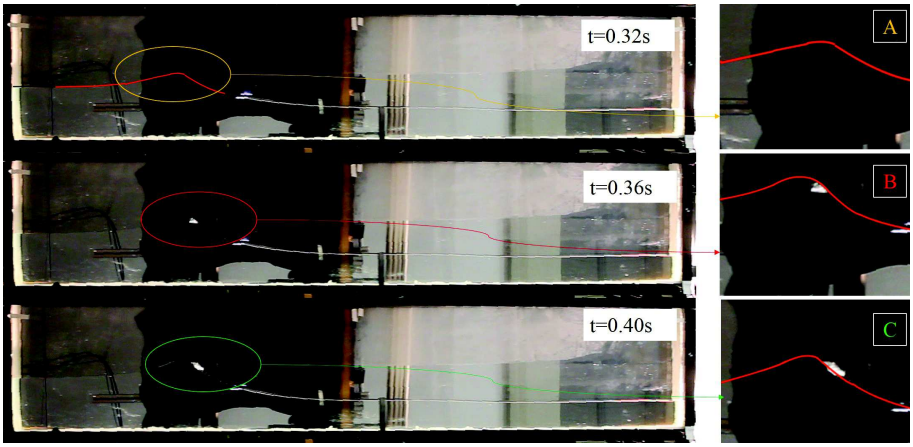

Figure 3.10: Visual observation of the wave crest evolution at three different time instants.

3.2 Mean velocity field

The mean and turbulent flow components were obtained through an ensemble-average of the instantaneous velocity. The mean velocity was calculated as

$$\langle \mathbf{v} \rangle = \frac{\sum_{i=1}^{N} \mathbf{v}}{N} \tag{3.1}$$

where $\mathbf{v} = (u, v)$ are the components of the instantaneous velocity in the (X, Y) coordinate system and $\langle \mathbf{v} \rangle = (U, V)$ are the related mean components.

The turbulent velocity components were evaluated as:

$$\mathbf{v'} = \mathbf{v} - \langle \mathbf{v} \rangle \tag{3.2}$$

In the present study, we focused on the single-phase turbulent region. Therefore, the mean average was done neglecting the air-water region close to the free surface, where the accuracy of the average algorithm could be strongly

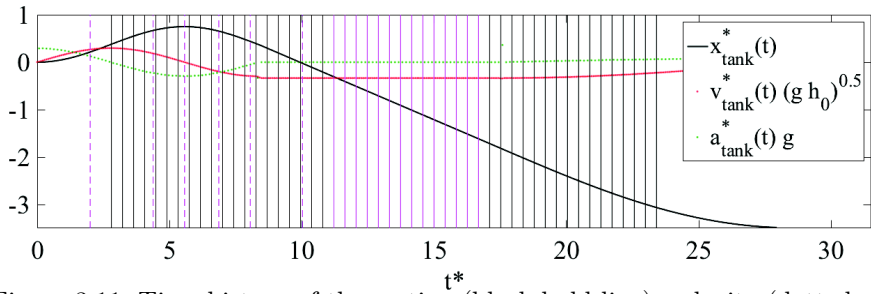

Figure 3.11: Time history of the motion (black bold line), velocity (dotted red line) and acceleration (dotted green line) of the tank. The continuous lines correspond to the times of the images of interest.

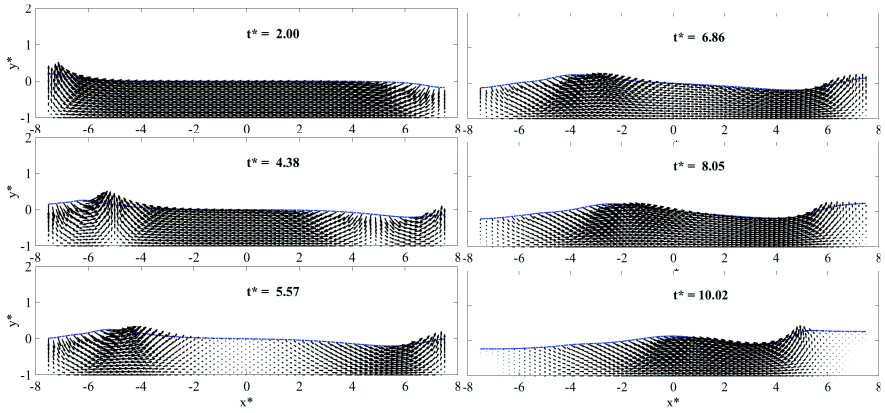

Figure 3.12: Image sequence of the velocity field evolution by the HPC solver.

affected by the two phase flow. For a proper understanding of the kinematic field in the wave body, we refer to the prescribed motion of the tank, which is shown in Fig. 3.11 with the black bold lines, along with its velocity (dotted red line) and acceleration (dotted green line).

In the same figure, the times corresponding to the experimental images are indicated by the continuous lines. Because the main focus of the present analysis is on the turbulent layer evolution, only the images between $t^* = 11.21$ and $t^* = 16.67$ (magenta continuous lines in Fig. 3.11) have been analysed. However, the initial evolution of the kinematic field is essential to fully understand the onset and the evolution of the breaking wave. Hence, we use the results of the HPC numerical solver; the chosen times are indicated by the magenta dashed lines in the tank motion history (see Fig. 3.11), while the corresponding images of the internal velocity field are shown in Fig 3.12.

At the beginning the tank is moved rightward, inducing a runup on the left wall and a rundown on the right side as a consequence of the standing wave connected with the highest sloshing natural period of the tank (see $t^* = 2$ in

Fig. 3.12). Due to the impulsive start of the tank and to the shallow-water condition, higher modes are quickly excited. This is testified by the velocity field shown at $t^* = 4.38$ in Fig. 3.12, which highlights a convergent line on the left side ($x^* \approx -1$) and a divergent line on the right side (approximately at $x^* \approx 1$) of the tank, distinctive of the third sloshing mode. A rightward propagating wave is generated at $t^* = 5.57$, corresponding to the time of the reverse tank motion; such flow counteracts the wave generated at the right wall by the reverse motion of the tank and propagating leftward (see $t^* = 6.86 - 8.05$). The interaction between the reverse waves causes, first, a stagnation region at the right wall (see panel at $t^* = 10.02$ in Fig. 3.12) and, then, the onset of breaking.
The following evolution of the mean velocity is shown on the left column of Fig. 3.13, through the results of the experimental analysis. The related streamlines are also reported on the right column of the same figure. Because of the light saturation of the two-phase turbulent layer, such layer has been removed through a gray-scale filtering of the images. The dashed lines on each panel of the right column represent the upper boundary of the two-phase layer, while the continuous line provides the single-phase free-surface. At these instants, corresponding to the magenta continuous lines of Fig. 3.11, the tank is moving leftward with a uniform motion. A first visual inspection of the velocity field, shows that the tank motion, along with the interaction of the two reverse waves, causes an upward flow with a steepening of the free surface from $t^* = 11.21$ (top panels of Fig. 3.13) to $t^* = 12.47$ (fourth row of the same figure).

However, the reverse flow interaction of the two waves governs the onset and the kinematics of the breaking wave, with a portion of the leftward wave which rides on top of an underlying "return flow" from the rightward propagating wave, this leading to an oblique divergent flow (see $t^* = 12.05$ of Fig. 3.13). In more detail, for $11.21 \leq t^* \leq 12.05$, the flow just at the lee and below the crest of the wave is largely upward, fed by the incoming opposite waves, and induces a slowdown and steepening of the wave crest. Then, breaking occurs (i.e. $t^* = 12.05$, see the previous section) and at $t^* = 12.47$, the still active wave interaction originates the splitting of the flow in four rotating flow regions: i) a lower flux moving clockwise and ii) an upward counterclockwise flow, both consequence of the wave propagating from left to right, iii) a downward counterclockwise and iv) an upper clockwise flow regions as consequence of the wave generated at the right wall and moving leftwards. These regions originate two flow lines, convergent and divergent, respectively (see Fig. 3.15), intersecting one another and generating a quadrupolar structure with a central saddle point. Very similar structures have been observed in numerical calculations of spiller and plungers (Watanabe et al., 2005).

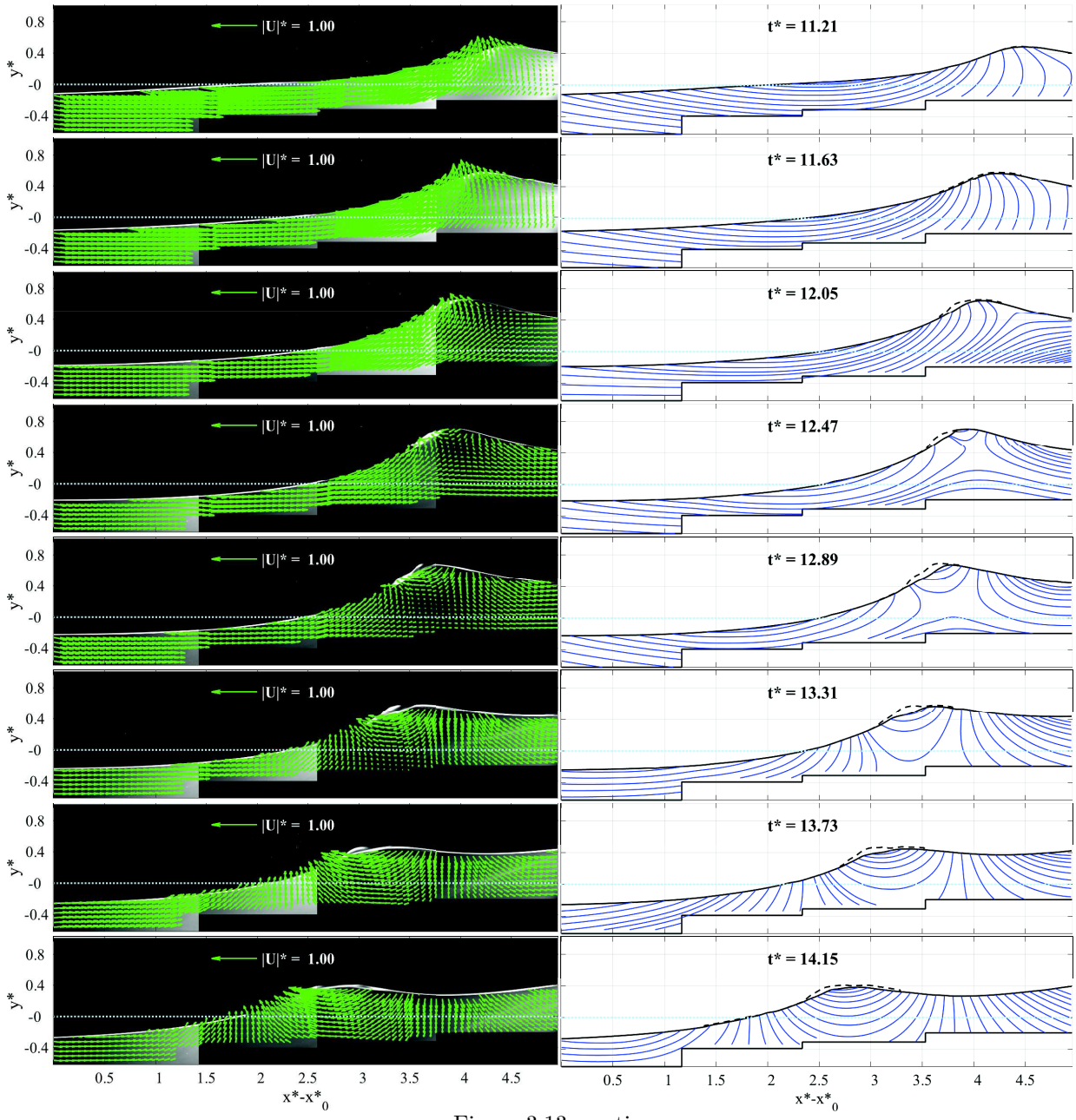

Figure 3.13: continue

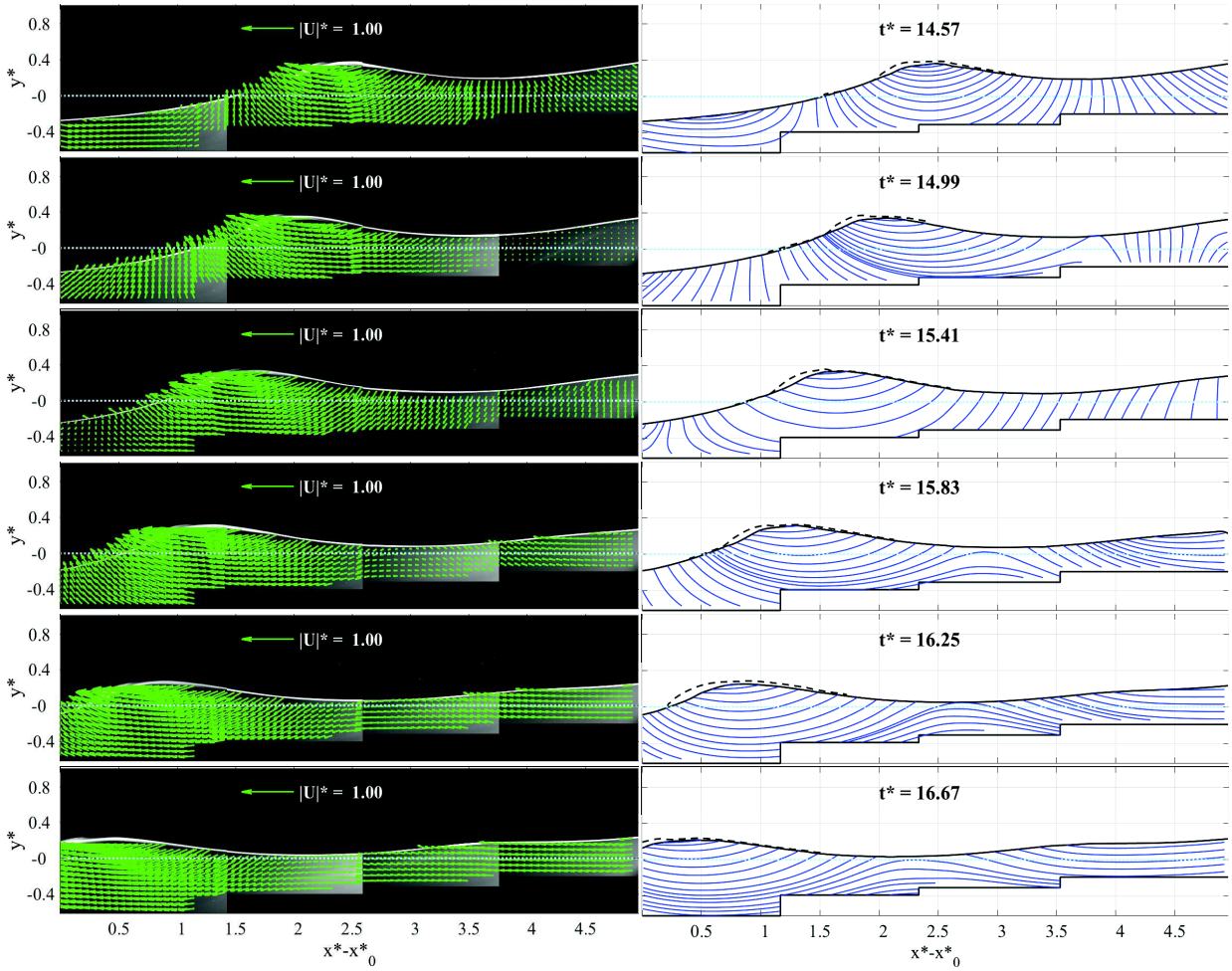

Figure 3.14: Image sequence of the evolution of the internal mean velocity field.

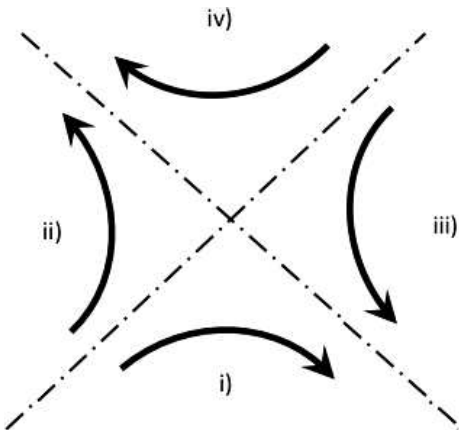

Figure 3.15: Sketch of the saddle-point at a quadrupole.

The saddle-point structure evolves towards the front of the wave, its center deepening of about $0.2h_0$ below the crest at $t^* = 12.47$ and of about $0.4h_0$ below the aerated breaker surface at $t^* = 12.89$. Over this period the wave steepness ($kH/2$) increases to reach its maximum of 0.25 at $t^* = 12.89$. It, thus, seems that the energy-based breaking occurs sometime before the largest wave height ($12.47 \leq t^* \leq 12.89$, see Fig. 3.6) and steepness (see also Fig. 3.6) are reached, such lags providing some measure of the wave inertia in its shoaling and steepening processes.
The mentioned flow structure, moves downward and in both the horizontal directions (see $t^* = 12.89$ of Fig. 3.13). In particular, it presses down region i), squeezing it, from $t^* = 12.89$ to $t^* = 14.15$, to the tank bottom. The consequent weakening of the quadrupole induces a flattening of the free-surface after $t^* = 14.57$, which preludes to the evolution of a quasi-steady breaker. In this second stage of evolution, the following main dynamics: evolve the near-surface flow of the breaker, part of the upper portion of a quadrupole and moves in the direction of the crest motion; the quadrupole deepens and weakens, its center moving towards the bottom of the tank and the front of the wave; the wave slowly flattens preluding to a quasi-steady evolution, as a consequence of the slow weakening of the quadrupolar structure. With the aim to understand the physical mechanisms governing the turbulent flow field below the wave crest, hereafter we discuss the spatial and temporal variation of the kinematic statistical quantities.

3.3 Characteristics of the vorticity at the free surface

Notwithstanding the evolution of the flow structures described in the previous section, a detailed analysis of the mean vorticity (i.e. associated with the mean flow) reveals that the body of the wave is almost irrotational, the vorticity being confined to the near-surface region (see Fig. 3.17). The flow related with the two-phase flow region has been removed by applying a gray scale filtering of the images. At the first instant that we consider useful for the analysis, is $t\sqrt{g/h_0} = 11.21$, a layer of counterclockwise (positive) vortical flow is evident far upstream of the wave crest, the lee side of the crest being characterized by some very small counterclockwise vorticity. At $t^* = 11.63$ much stronger vorticity ($20 \leq \omega^* = \omega\sqrt{h_0/g} \leq 25$) is observed exactly at the wave crest and using a vorticity-injection-based criterion this would be the time of breaking inception. However, in view of the fairly coarse temporal resolution available ($\Delta t^* = 0.4375$), it is possible that the actual vorticity-based breaking onset occurs in the interval $11.21 \leq t^* \leq 11.63$.

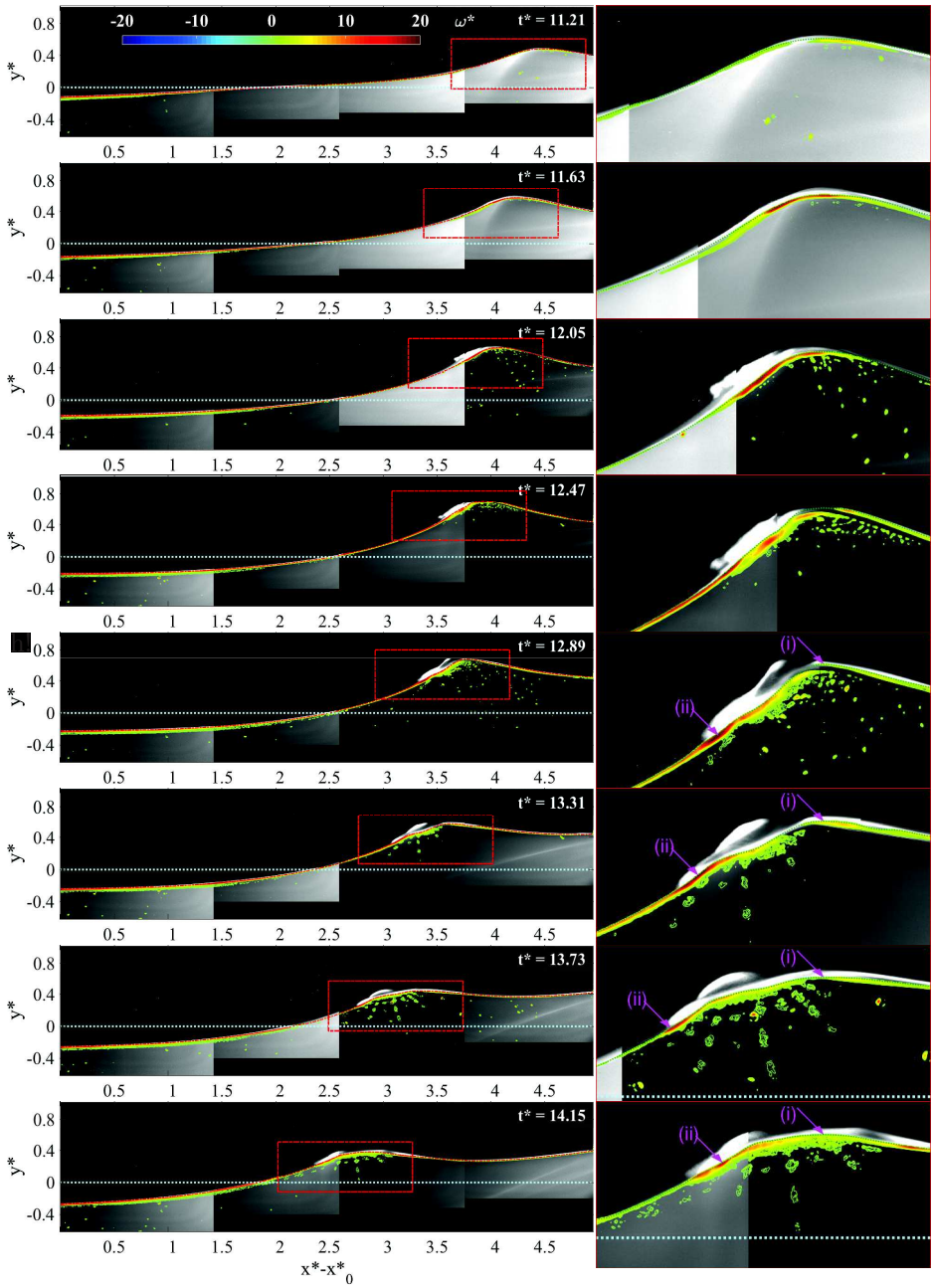

Figure 3.16: continue

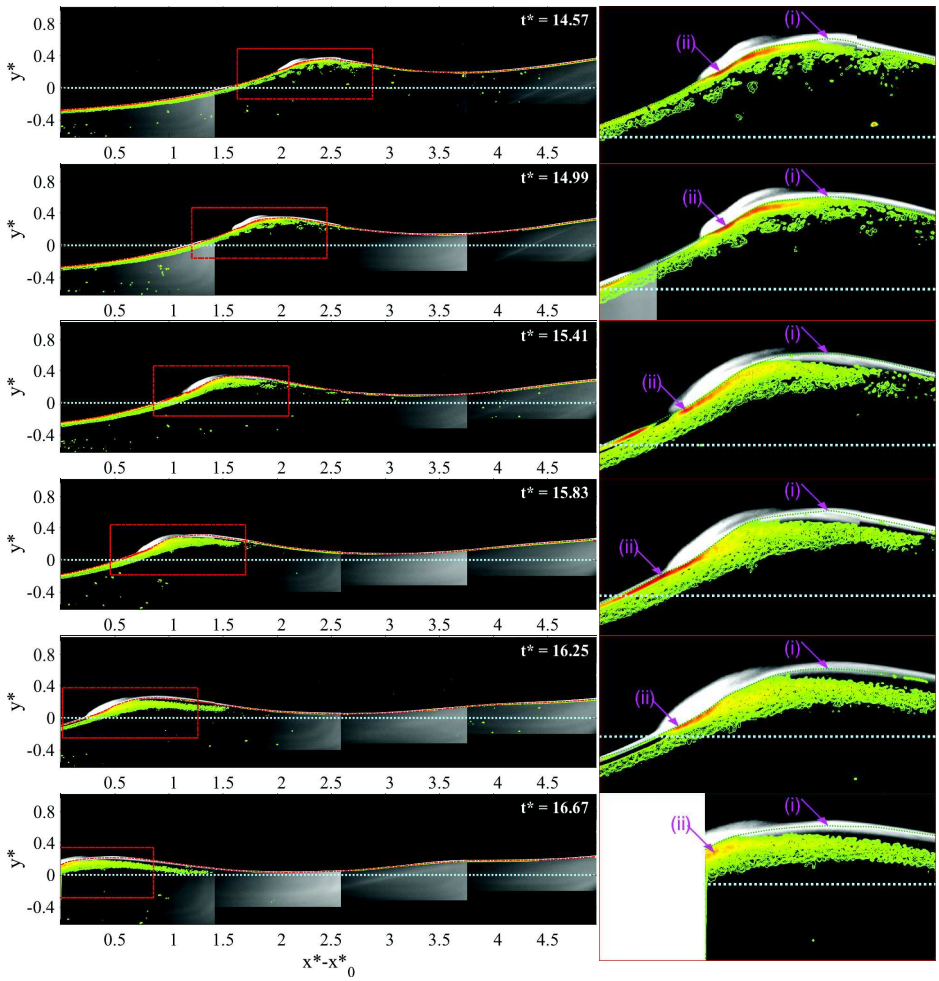

Figure 3.17: Image sequence of the generation and evolution of the vorticity in the shear layer for an unsteady spilling breaker.

It is noted that these times are in fairly good agreement with the breaking onset time, $t^* = 12.046$, given by the energy criterion illustrated in the previous section. At later times the vortical layer lengthens down the front face of the wave, increases in intensity and thickness (because of diffusion), till time $t^* = 12.89$ when the maximum wave steepness is reached and the peak of positive vorticity is well ahead of the wave crest. At the same time the crest deforms to assume a non-monotonic shape, made of two bumps, (i) crest and (ii) location of maximum vorticity upstream of the crest, and a small intermediate dip. The interface bump characterized the maximum vorticity stays ahead of the crest of a fairly constant distance (about $2h_0$) till the end of the observation ($t^* = 16.25$) and, in view of the common knowledge on wave breaking, might be regarded as the toe of the breaker.
From what above, the mechanism of generation of vorticity seems more connected to the local deformations of the free-surface (i.e. increase of its curvature) rather than to the global steepening of the wave crest. The vorticity that we analysed is due to the mean velocity field and probably, we are unable to identify a vortical structures because they are present in a smaller spatial scales, while, in this case we are in a more larger spatial scales.

3.4 The turbulent kinetic energy

The temporal evolution of the specific (per unit mass) turbulent kinetic energy (TKE) (see Fig. 3.18), highlights the generation of an intense shear layer formed below the free surface of a fully-formed unsteady spilling breaker, which spreads upward from the toe of the breaker.
A small fraction of the maximum turbulent kinetic energy (5%), has been chosen as a threshold to define the lower spatial boundary (pink dashed line) of the turbulent region which in the analytical model gives $\Upsilon(t)$. It is noted that the TKE is here made dimensionless with the velocity scale gh_0, i.e. $TKE^* = TKE/gh_0$. The upper boundary of the thin single-phase turbulent layer, instead, has been determined through gray scale filtering of images and excludes the two-phase turbulent layer.
The spatial and temporal evolution of the TKE (shown in Fig. 3.18) have been analysed from $t\sqrt{g/h_0} = 11.21$.
However, it is only at time $t^* = 11.63$ that some intense turbulence is visible at the front face of the wave, slightly downward, more upstream (about $h_0/3$) of the peak of vorticity (generation of TKE, labelled as “phase a”). This instant exactly coincides with the vorticity-based onset of breaking and almost exactly with the onset predicted through the energy-based criterion (at time 12.046, see previous section).

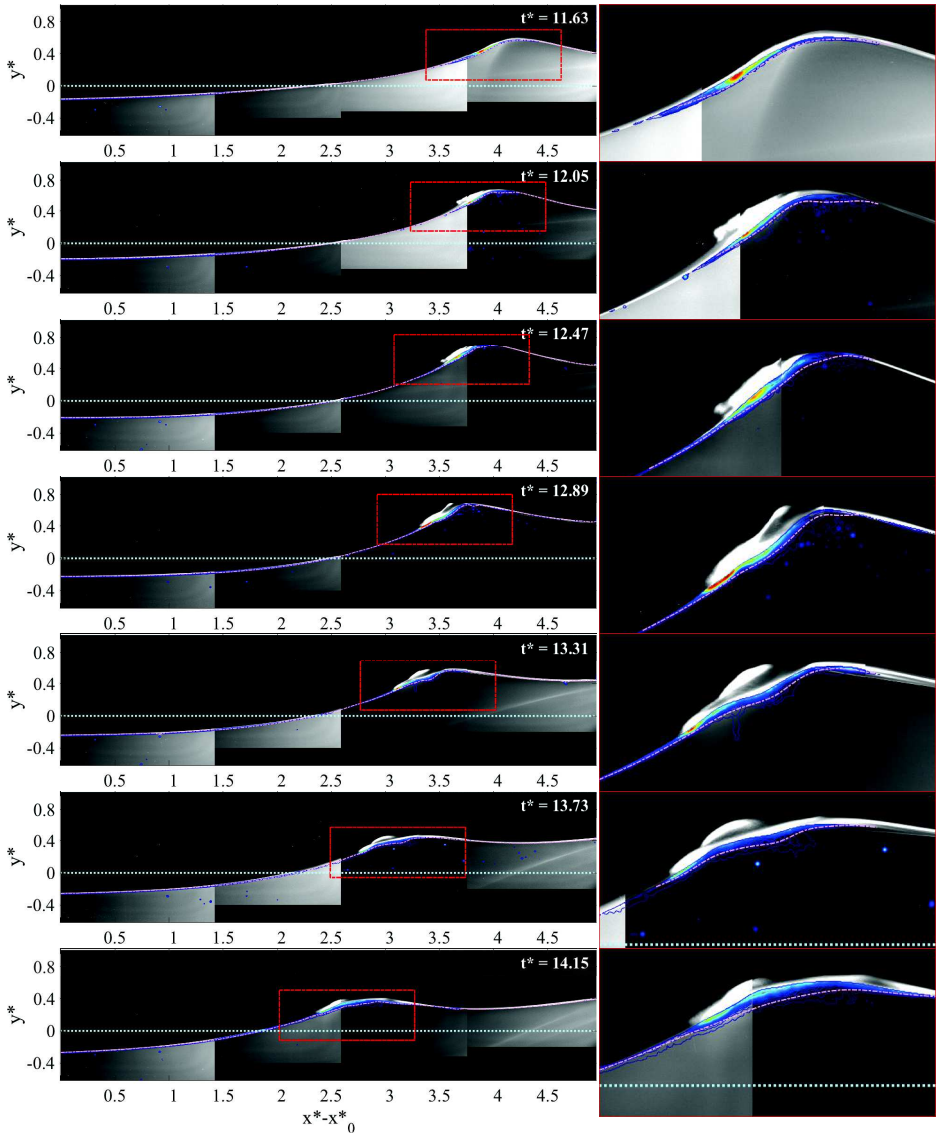

Figure 3.18: continue

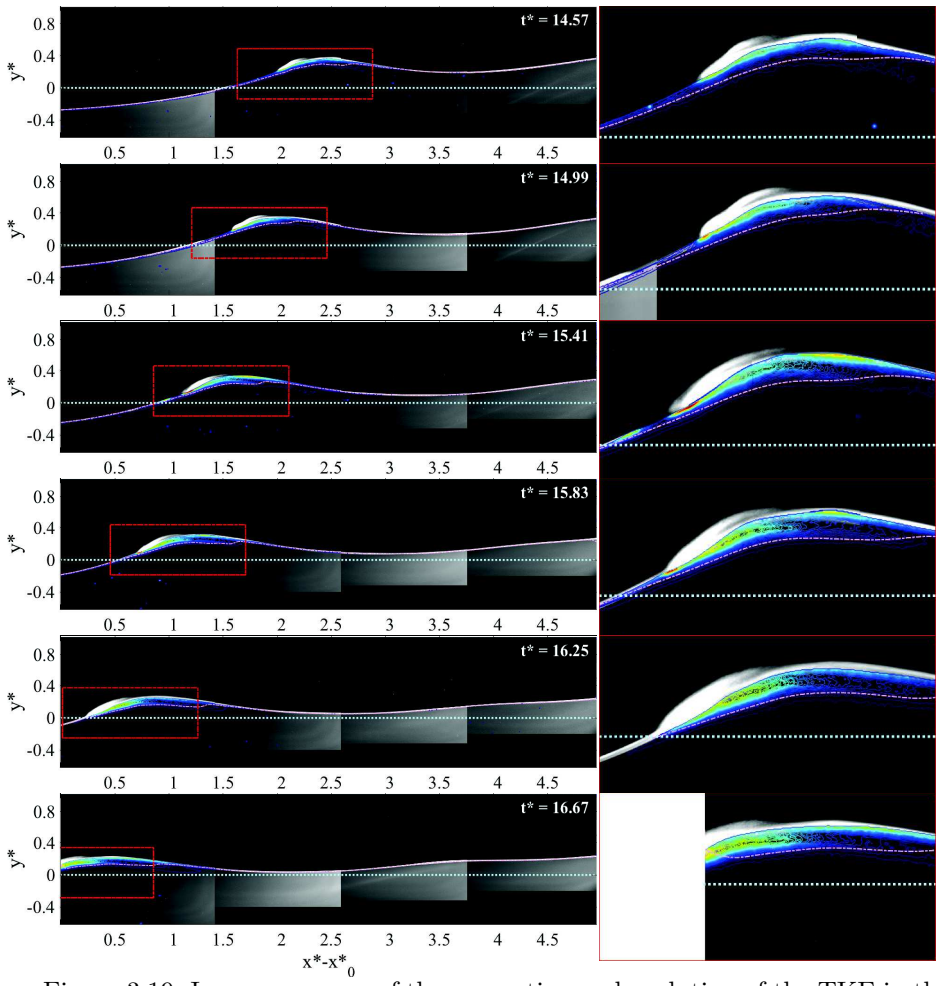

Figure 3.19: Image sequence of the generation and evolution of the TKE in the shear layer of an unsteady spilling breaker.

Like for the vorticity, the patch of TKE is seen to slide and lengthen down the front face of the wave, its peak ($TKE^* \sim 0.020 - 0.025$) being still more upstream than the peak of vorticity and reaching the toe of the breaker at $t^* = 13.31$ (downward slide of turbulence, labelled as "phase b"). Also, similarly to the vorticity, the TKE peak is placed below the more upstream of the two local bumps visible at the wave crest (i.e. bump (ii)). All the events here described evolve during stage (1) of evolution of the TKE. Such coherent stage of evolution is also reflected in the analysis of the geometry of the turbulent layer (see the subsequent section).
Later, during stage (2), which begins at $t^* \geq 13.73$, similarly to the vorticity, the TKE, though steadily diffusing in the lower region of the flow, is characterized by an intensity pulsation made of sudden decays ($t^* = 13.73, 14.15, 16.25$) and growths ($t^* = 14.57, 14.99, 15.41$) of its peak values. Moreover, the region over which the TKE diffuses is slightly smaller than that over which the vorticity diffuses. We believe that the above effects, pulsation and reduced diffusion, are due to some centrifugal action related with the curvature and local rotation of the single-phase turbulent layer, here measured with κ and Ω, respectively. These aspects will be analysed in detail in a dedicated work.
In other words, the gradual decrease of wave steepness, which occurs for $t^* = 13.73$ is accompanied by unsteady local effects related with the pulsation of the local flow curvature, rotation and thickness of the turbulent layer. Hence, like for the vorticity, also the TKE seems to be more significantly affected by local rather than global dynamics. During the final stages of interest ($t^* \geq 16.25$) the Υ interface becomes almost parallel to the tank bottom with the turbulent region closely resembling that evolving into a quasi-steady hydraulic jump.

3.5 Geometry of the single-phase turbulent region

In this section, the attention was focused on the geometric characteristics (thickness (b), streamwise length (L) and ϵ) of the single-phase turbulent layer, as described in the theoretical model by Brocchini (1996) (see Fig. 3.20). The analysis is similar to that of Misra et al. Misra et al. (2008), who used their experimental data for a hydraulic jump (steady phenomenon) to provide estimates of the geometry of the shear layer as a proxy for the single-phase turbulent region of a spilling breaker. In that case, the shear layer, being caused by a quasi-steady hydraulic jump, was characterized by one single value of ϵ, independent of time. On the opposite, our unsteady breaker is characterized by thicknesses and length that are functions of time and also of the position downstream of the breaker toe. Fig. 3.21 illustrates the evolution in time of the single-phase layer thickness (b) and length (L_s). Such thickness has been evaluated through the intersection of the limit curves that define the shear layer.

The red dashed line visible in each plot, represents the maximum possible experimental error ($2px/mm$). The first point, located at zero abscissa, is at the toe of the breaker, here taken as the most upstream point of the single-phase turbulent region.
Two main stages of evolution are here visible. Stage (1), goes from $t^* = 11.63$ to $t^* = 13.73$ and it is characterized by an almost constant maximum thickness of about 0.03 and length pulsation around the value of 1. This first stage includes both phases of (a) generation of TKE and (b) downward slide and lengthening of the single-phase turbulent region, described in the previous section.
The second stage, (2), begins at $t^* = 14.15$ when the layer thickness rapidly and unsteadily increases from 0.05 to the maximum value of about 0.1 at time $t^* = 15.41$, settling to about the same value for longer times. During the same stage the length of the single-phase turbulent region oscillates between 1.5 and 2. These behaviours are well evident in Fig. 3.22 and 3.23, which, respectively, give the evolution in time of the maximum layer thickness and length. The blue circles and the dashed line give, respectively, the effective measures of the maximum shear layer thickness and the interpolating polynomial, fourth-order for b and third-order for L_s. Hence, this second stage coincides with the vorticity and TKE pulsation stage described in the previous sections.
The above clear subdivision seems to occur at the time when the crest steepness significantly decreases and the pulsation in thickness observed during the second stage seems to be related with the pulsation of local curvature and rotation of the turbulent layer.

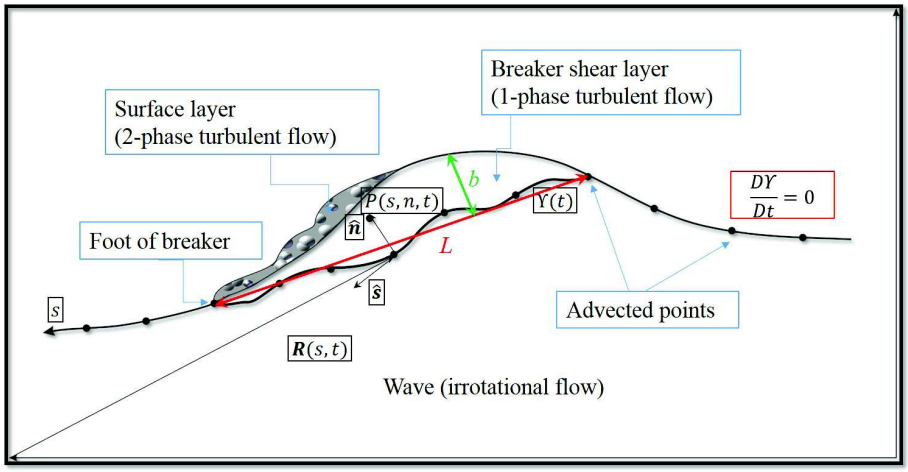

Figure 3.20: Schematic view of the theoretical model of Brocchini (1996)

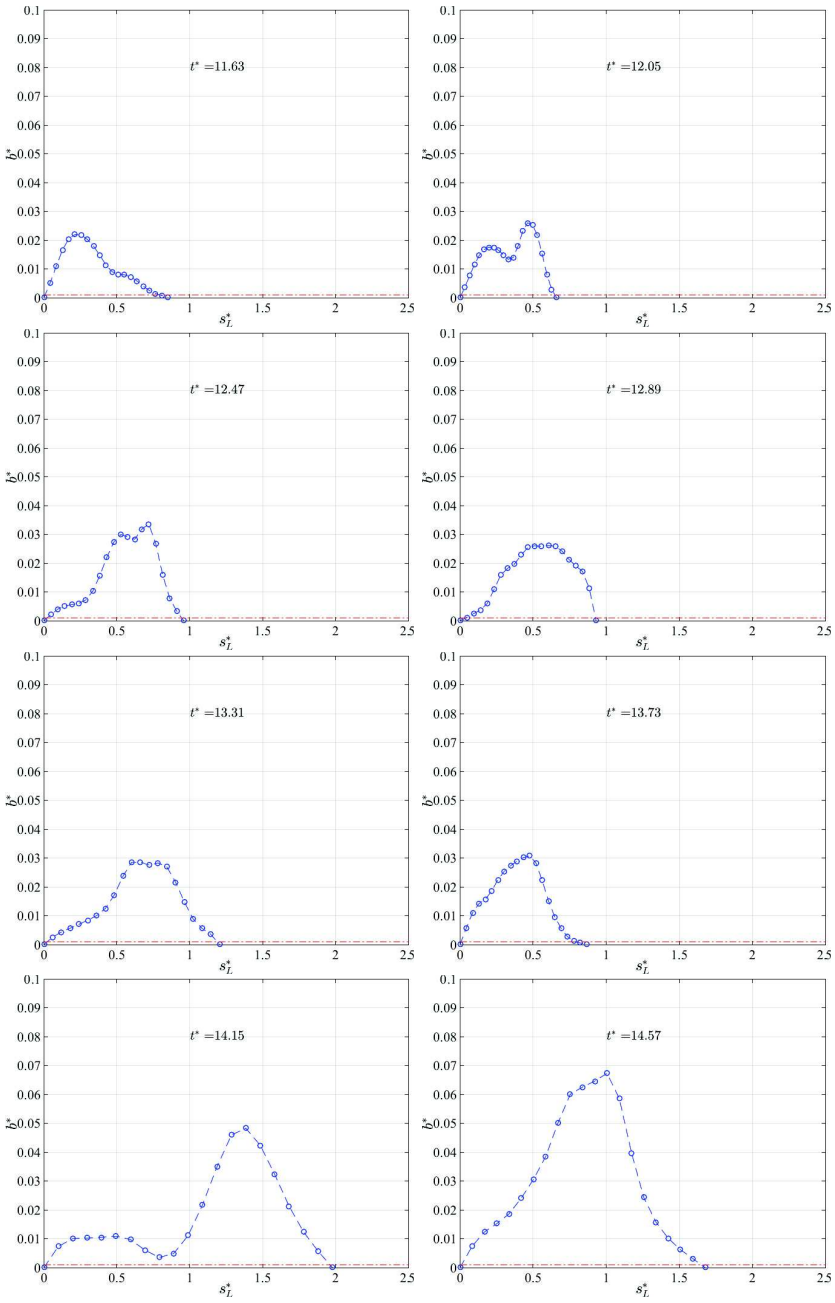
$t^* = 11.63$
$t^* = 12.05$
$t^* = 12.47$
$t^* = 12.89$
$t^* = 13.31$
$t^* = 13.73$
$t^* = 14.15$
$t^* = 14.57$
b^*
s_L^*

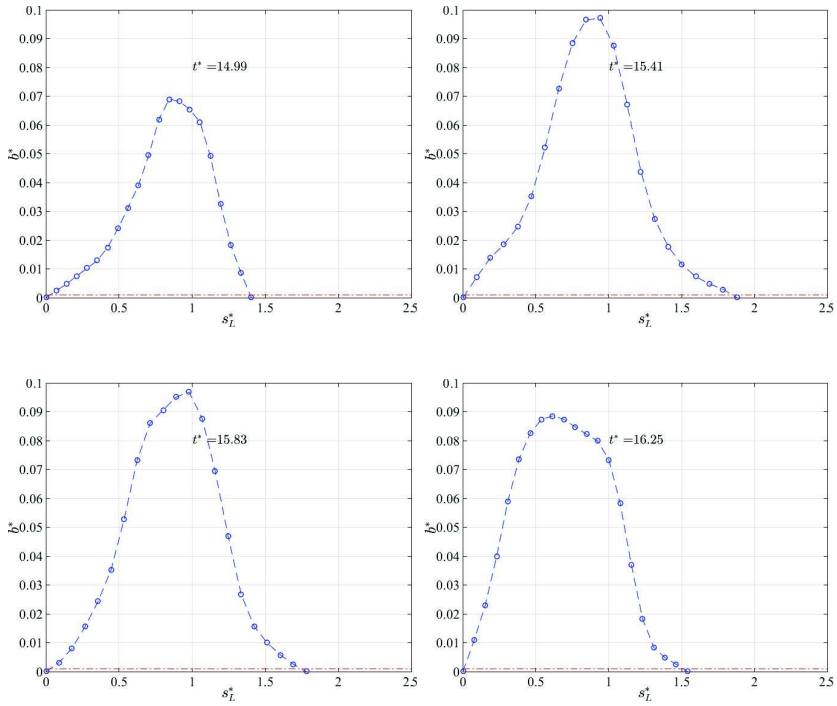

Figure 3.21: Evolution in time of the single-phase layer thickness plotted against normalised curvilinear abscissa: the time is increasing from left to right, from top to bottom.

Attempting at a comparison with the literature, we find that in Misra et al. Misra et al. (2008), the dimensionless streamwise variation of the width of the layer, increased linearly until 0.29, after which it becomes constant and the flow resembles a wake. In any case, the thickness of the turbulent region observed by Misra et al. Misra et al. (2008) is very large compared with our results.
Finally, the thickness parameter ϵ, is shown in Fig. 3.24. Also this function has been interpolated with a fourth-order polynomial, like b. The maximum value achieved is about 0.06, which is the same of that observed by Tennekes and Lumley (1972) for jets and mixing layers (values of order 0.06). In Misra et al. Misra et al. (2008), values of ϵ averaged over the breaker shear layer were of the order 0.03, which is slightly smaller compared with our results and those of Tennekes and Lumley Tennekes and Lumley (1972). These values are small enough to justify use of the "thin layer" approximation.

Fig. 3.24 also highlights the clear separation of stages (1) and (2), this occurring around $t^* = 14.15$.

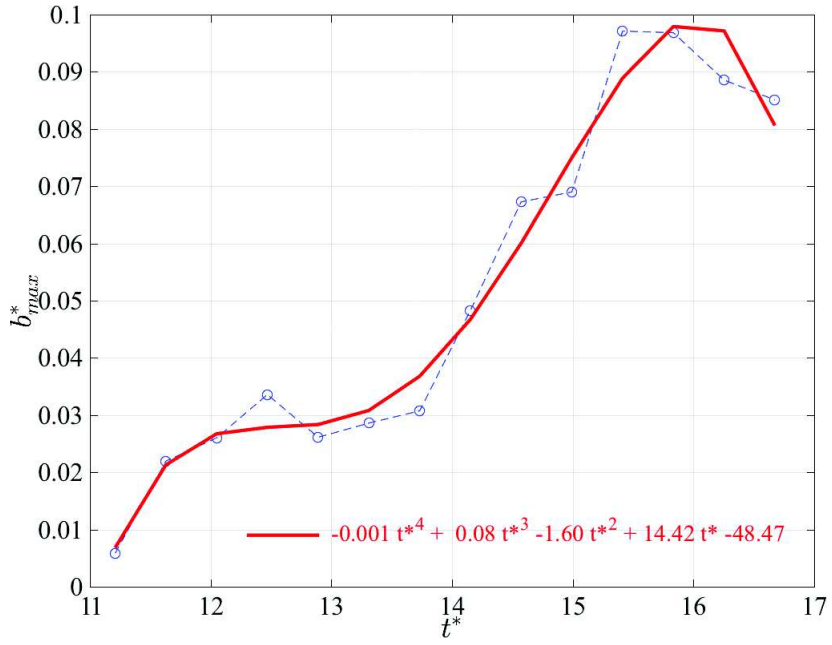

Figure 3.22: Evolution of the maximum thickness of the single-phase layer in time.

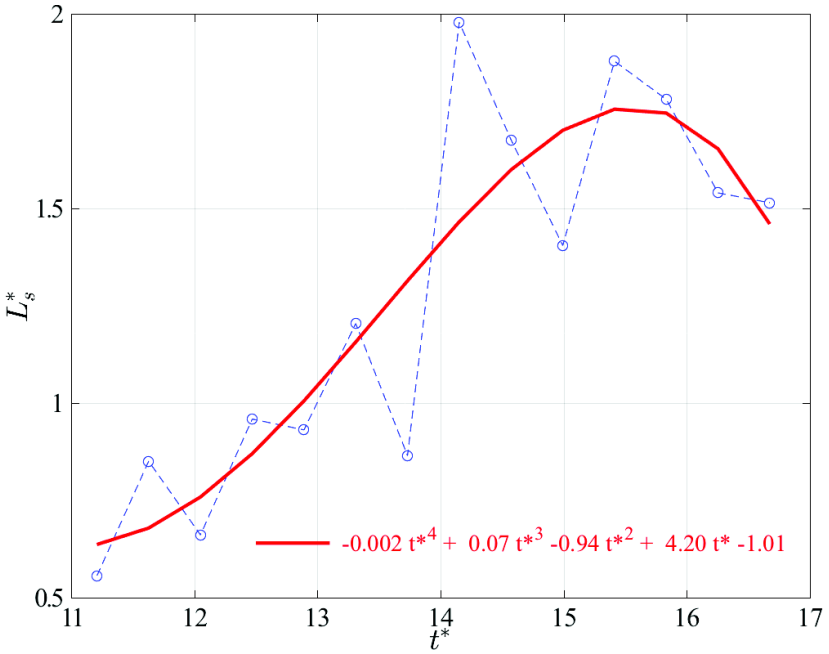

Figure 3.23: Evolution of the interface length in time.

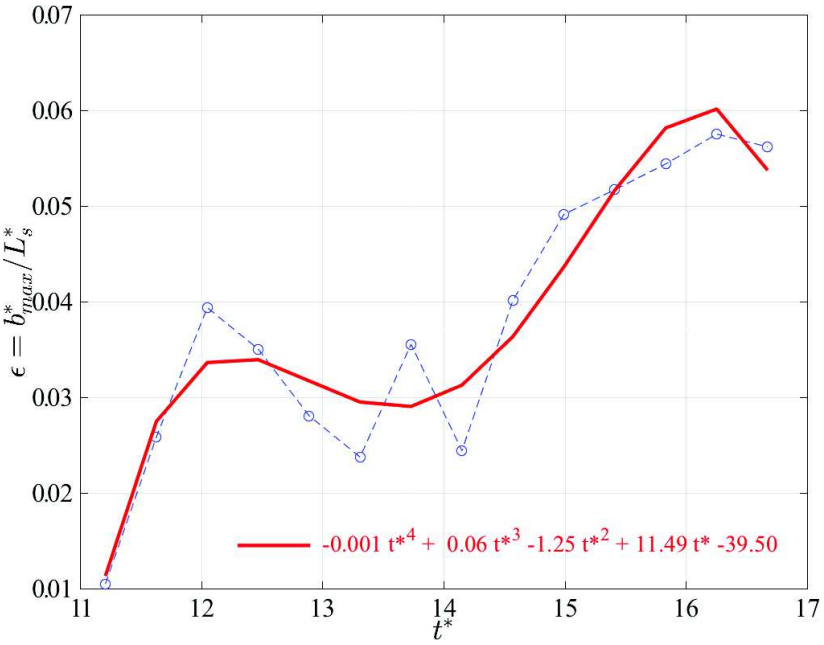

Figure 3.24: Evolution of thickness parameter in time.

Chapter 4

Validation of the theoretical model by Brocchini and Peregrine

The experimental data set collected in the present work will help validate the analytical model proposed by Brocchini (1996), limiting to the case of a gentle spilling breaker. Only the experimental mean velocity profile in the shear layer is here used as preliminary validation of the analytical model. Other physical quantities defined in the analytical model will be inspected in future studies.

4.1 Mean velocity profile in the shear layer

Following the idea of Madsen and Svendsen (1983) for a steady breaker, a cubic polynomial profile was defined by Brocchini (1996) for the mean velocity profile in the shear layer below an unsteady breaker, in correspondence of the single-phase layer below the crest. They get a quantitative description of the flow by forcing a solution which obeys one single physical constraint, i.e. an inflection point for the velocity within the thin single-phase turbulent layer.
In physical component it is of type:

$$\langle u(1)\rangle(s,n,t) = \langle u(1)\rangle(s,0,t) + f(s,t)\,g(\sigma)$$

$$with \quad g(\sigma) = -A\sigma^3 + B\sigma^2 + C\sigma + D \quad and \quad \sigma = \frac{n}{b(s,t)} \tag{4.1}$$

where $\langle u(1)\rangle$ is the streamwise component of the mean velocity, $b(s,t)$ is the local thickness of the single-phase turbulent layer.
Lastly, $\langle u(1)\rangle(s,0,t) = \frac{\partial \phi}{\partial s}(s,0,t)$ is the velocity at the lower limit of the layer ($n = 0$), on the $\Upsilon(t)$.
The coefficients of $g(\sigma)$, differently to that used in the model of Madsen and Svendsen (1983), are not constant but functions of (s,t).
These coefficients and $f(s,t)$ are found through an appropriate matching conditions at $n = 0$ or $\sigma = 0$ (i.e. at the interface between the single-phase turbulent

layer and the irrotational flow region below), and at $n = b$ or $\sigma = 1$ (i.e. at the top of the single-phase turbulent layer).
The two phase surface layer contributions were taken into account by enforcing the kinematic free surface boundary condition at the top of the single-phase shear layer, using the results of Brocchini and Peregrine (2001b) and Brocchini (2002).
Assuming the vanishing of the shear stresses at the interface with the underneath irrotational flow and the continuity of the mean velocity across the single-phase turbulent layer, the mean streamwise velocity, is equal to:

$$U(s,\sigma,t) = \hat{U} + \left(U_b + \hat{U}\right)\sigma^2 + A\left[U_b - \hat{U} - b(s,t)\,\Omega\right]\sigma^2(1-\sigma) \qquad (4.2)$$

Considering $\Omega = 0$, the mean flow profile becomes:

$$U(s,\sigma,t) = \hat{U} + \left(U_b + \hat{U}\right)\sigma^2 + A\left[U_b - \hat{U}\right]\sigma^2(1-\sigma) \qquad (4.3)$$

Through our experimental data, we are able to check the analytical solution (4.3) for the mean velocity profile (Fig. 4.1). By approximating $\hat{U}$ and U_b with the mean streamwise velocity values at the bottom and top of the shear layer, respectively, the cross-flow profile of the mean streamwise velocity at each vertical location was calculated. The assumption is that in the local frame of reference, $\hat{U} = 0$. Furthermore, a cubic polynomial (continuous magenta line) has been fit to the measured value of $U(s,\sigma,t)$, all the streamwise locations were treated and for each instant t_0, the value of the parameter $A(s,t_0)$ is shown with relative errorbar (Fig. 4.1).
In Misra et al. (2006), the same procedure was adopted, but because of the small thickness of the shear layer near the toe, few data points were available for a robust fit of the profile. Therefore they chose the streamwise location in the middle part of the shear layer.
In the present case, considering $\hat{U} = 0$ and dividing each term for U_b, the equation 4.3, becomes:

$$\frac{U(s,\sigma,t)}{U_b(s,t)} = \sigma^2 + A(s,t)(1-\sigma)\sigma^2 \qquad (4.4)$$

The unsteady flow of the present breaker leads to $A = A(s,t)$, differently from the case Misra et al. (2006) (steady phenomenon) where $A = A(s)$.
Though at this preliminary stage, it is not possible to explicitely relate the variation of $A(s,t)$ with the physical quantity involved, it is expected that future analyses of the data will enable the modelling of $A(s,t)$.

Analysing in time the cross-flow profile of the mean streamwise velocity and the behaviour of the parameter $A(s,t)$, we can identify three main stages. The first one, that goes from $t^* = 11.63$ to $t^* = 12.47$, where the value of A is influenced by the nonstationarity of the phenomenon and a fairly small mean velocities are observed to occur within a fairly thin single-phase turbulent layer. The second one, from $t^* = 12.89$ to $t^* = 14.57$, shows how, the parameter $A(s,t)$ is characterised by fairly streamwise-uniform distribution with mean $A(s,t) = 1$. This mean that, assuming $\Omega = 0$, the shear stress at the top boundary of the single-phase turbulent region is:

$$\frac{\partial U}{\partial n} \approx \frac{U_b}{b} > 0.$$

Noticeable is the small size of the errorbar, testifying an excellent fit of the experimental data. The situation changes in the third stage (from $t^* = 14.89$ to $t^* = 16.67$), where the rotation and curvature of the shear layer decrease and the thickness of the single-phase turbulent region increase. The maximum of the streamwise velocity is located in the middle of the layer while the streamwise distribution of $A(s,t)$ is less uniform and tends to increase till $6 \div 7$ from the leading edge to its trailing edge. This means that, assuming $\Omega = 0$, the shear stress at the top boundary of the single-phase turbulent region is:

$$\frac{\partial U}{\partial n} \approx -C\frac{U_b}{b} < 0, \qquad with \qquad C \sim 4 - 5.$$

This negative shear depends on the value of U_b that decrease and the cubic profile is very evident.

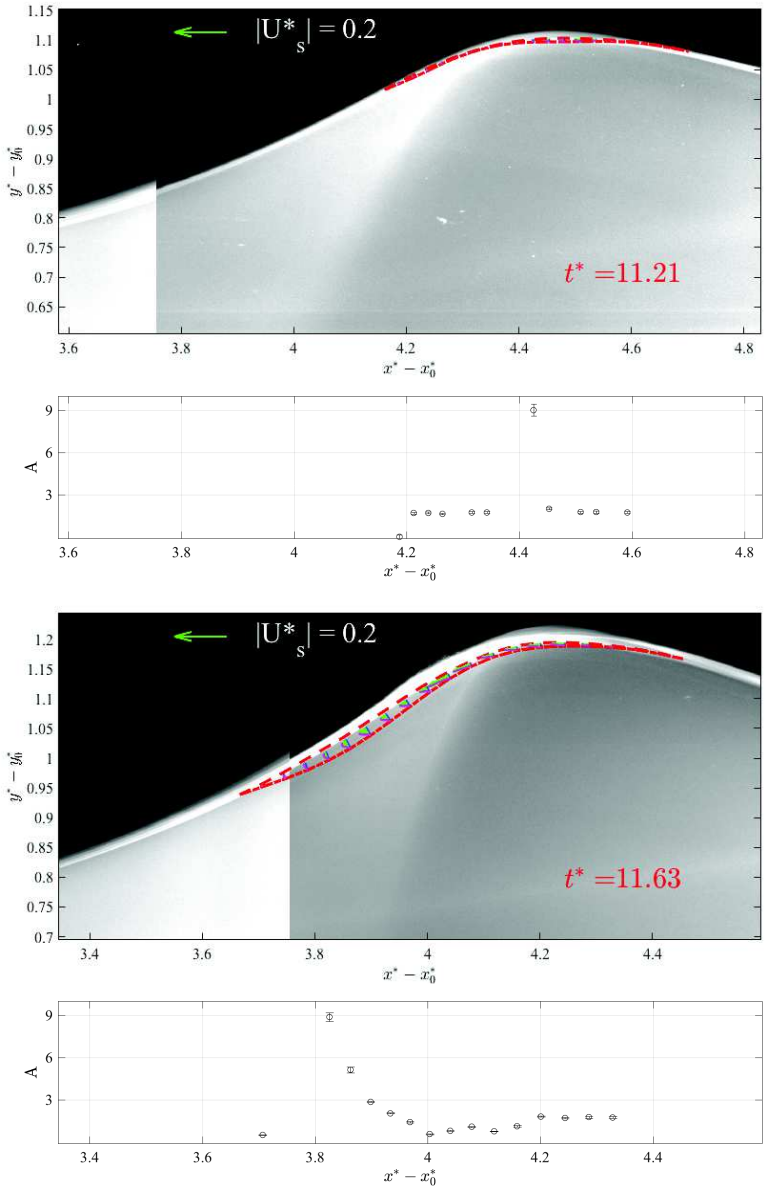
|U*s| = 0.2
t* =11.21
A
$x^* - x_0^*$
$y^* - y_b^*$
|U*s| = 0.2
t* =11.63
A
$x^* - x_0^*$
$y^* - y_b^*$

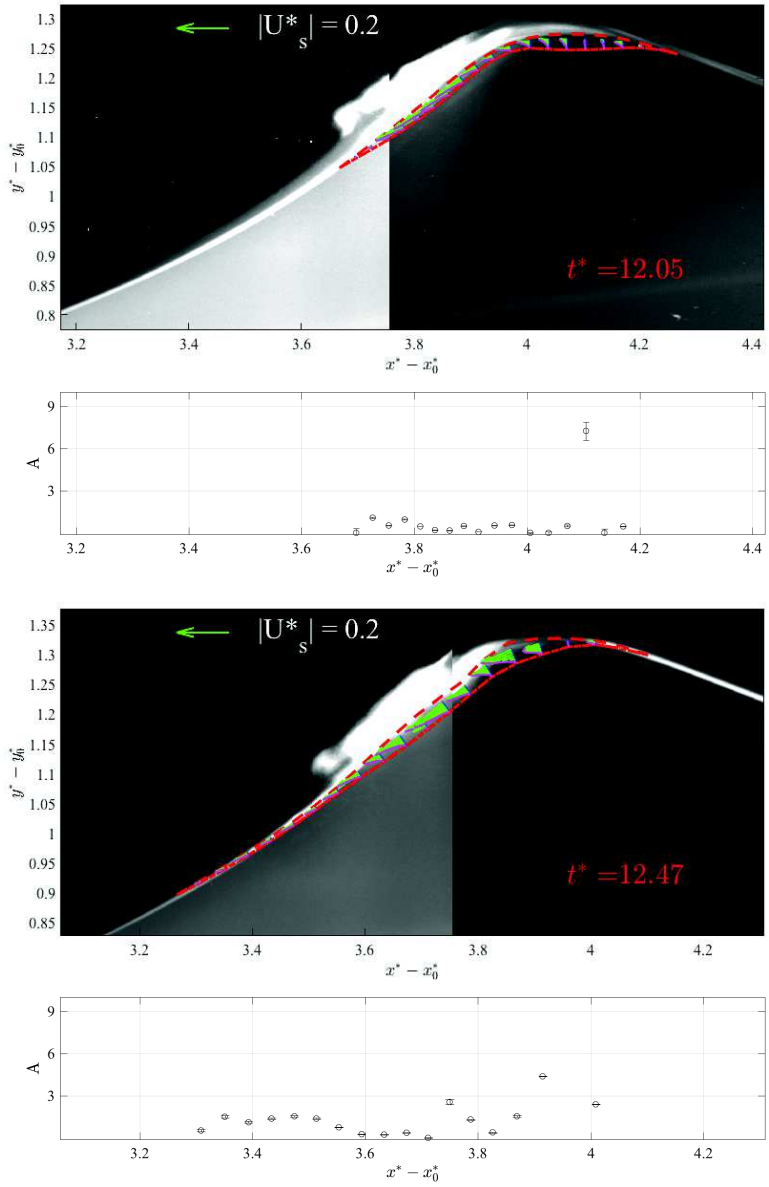
|U*s| = 0.2
t* =12.05
y* − y*0
x* − x*0
A
|U*s| = 0.2
t* =12.47
y* − y*0
x* − x*0
A

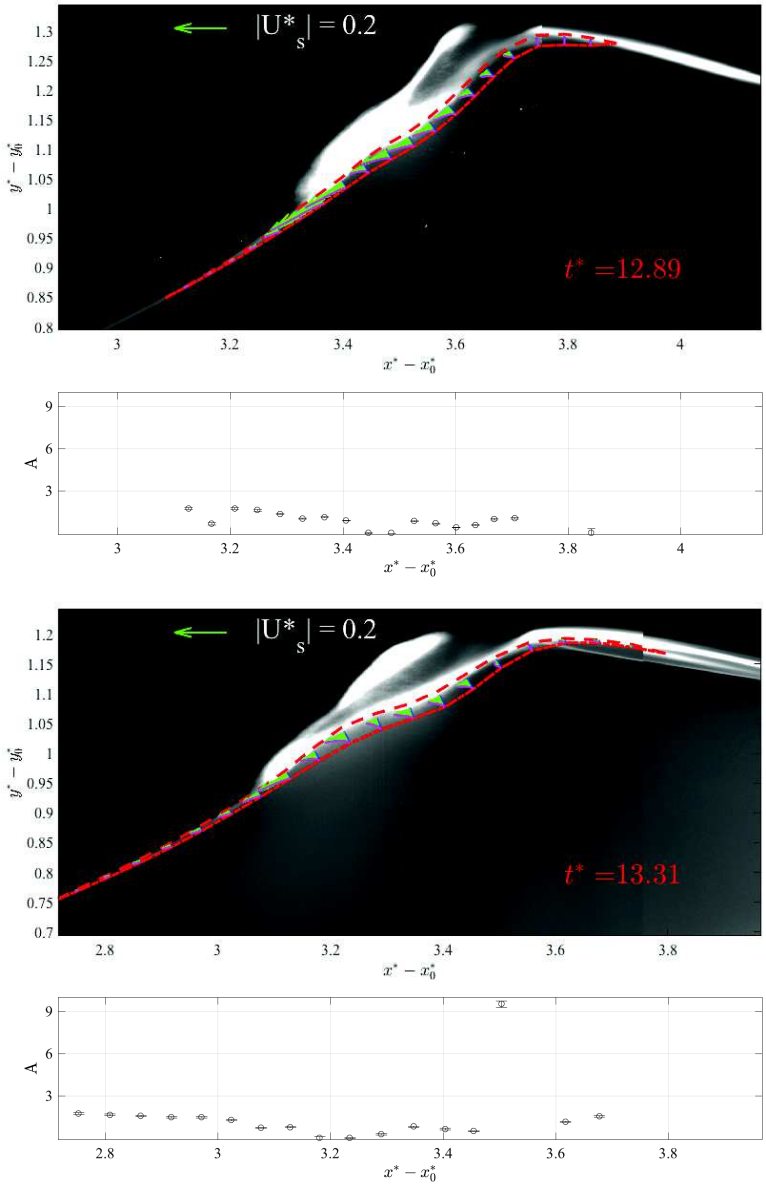
|U*s| = 0.2
t* =12.89
A
|U*s| = 0.2
t* =13.31
A

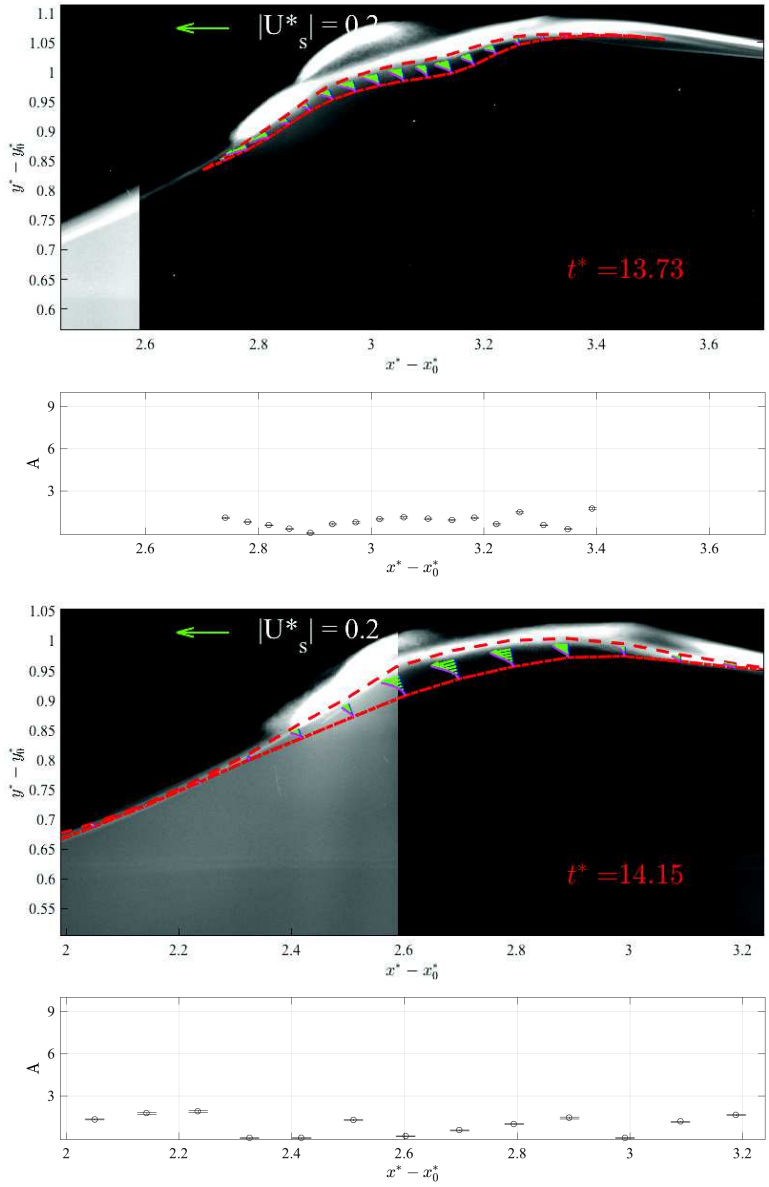
|U*s| = 0.2
t* =13.73
y* − y*0
x* − x*0
A
|U*s| = 0.2
t* =14.15
y* − y*0
x* − x*0
A

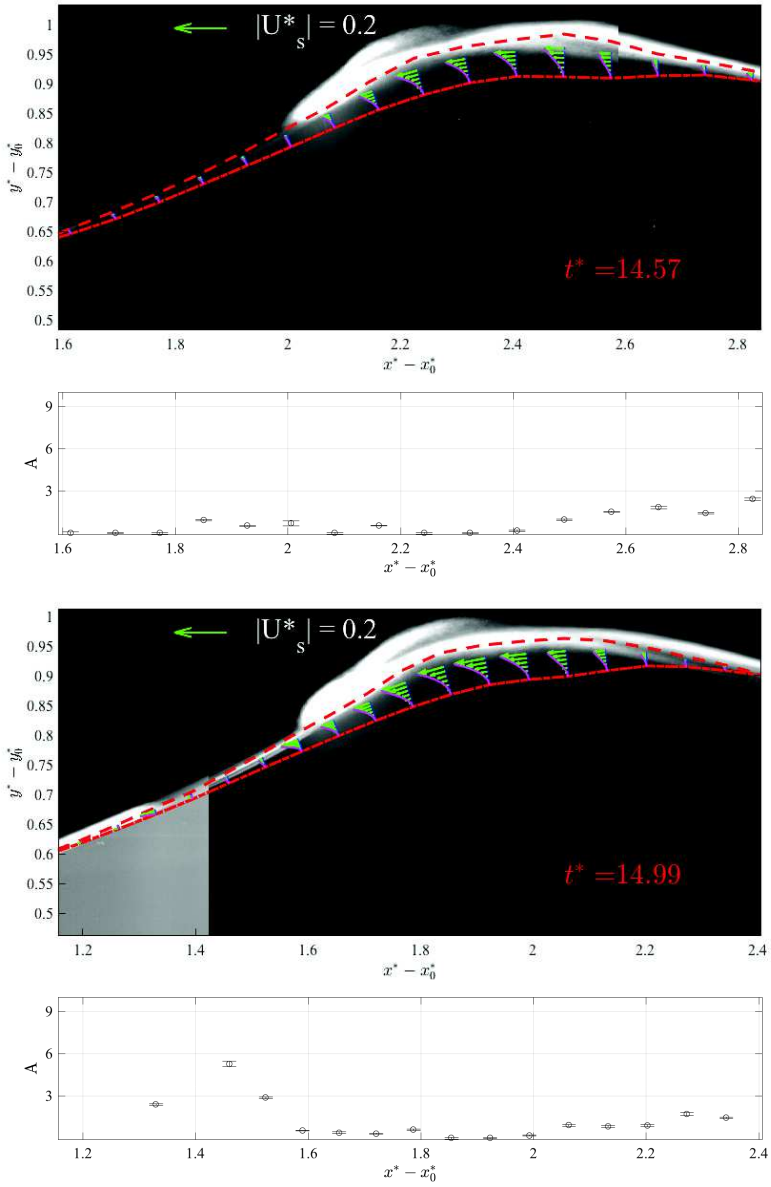
|U*s| = 0.2
t* =14.57
$y^* - y_0^*$
$x^* - x_0^*$
A
|U*s| = 0.2
t* =14.99
$y^* - y_0^*$
$x^* - x_0^*$
A

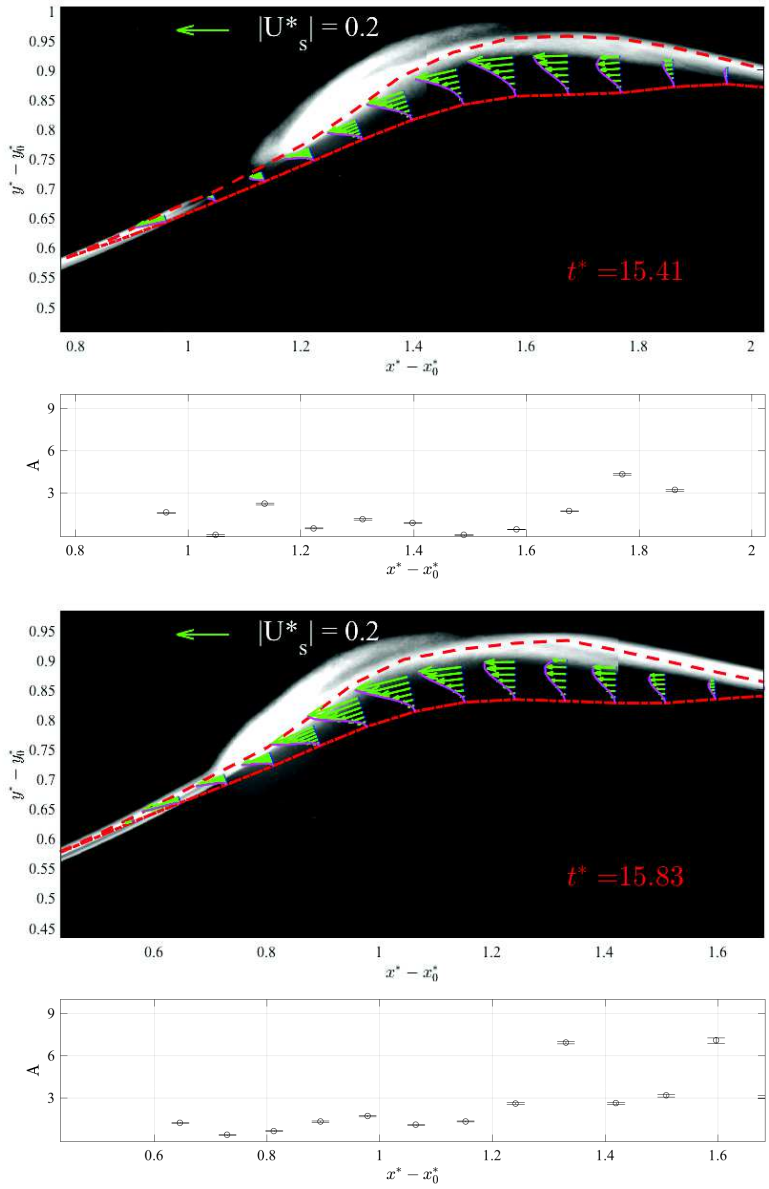
|U*s| = 0.2
t* =15.41
$y^* - y_0^*$
$x^* - x_0^*$
A
|U*s| = 0.2
t* =15.83
$y^* - y_0^*$
$x^* - x_0^*$
A

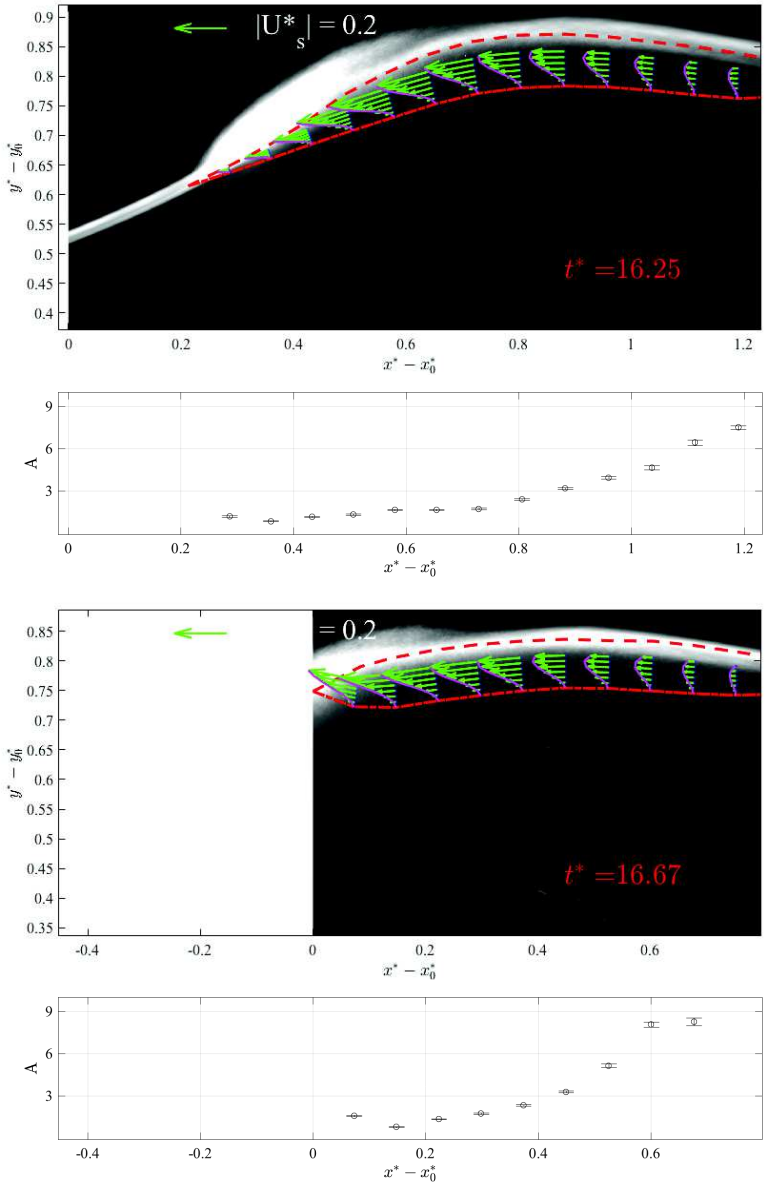

Figure 4.1: Evolution in time of the mean velocity profile in the thin single-phase turbulent layer.

Chapter 5

Discussion and conclusions

The objective of this thesis has been to experimentally study an unsteady gentle spilling breaking wave and to analyse in details the geometric and kinematic characteristics of the thin single-phase turbulent layer. A sloshing wave has been used for the generation of the breaker. A 3m long, 0.60 depth and 0.10m wide tank has been built in Plexiglass and forced through an hexapode system. The tank motion has been designed by two different numerical solver: HPC (potential solver) and Navier-Stokes solver. Thanks to the last one, we have been able to define the area of interest (1.80m) for our analysis and choice the equipment for measurements. For a good temporal and spatial resolution of each camera, the area of interest has been divided into two different zones and only the first one (upstream zone) has been analysed because it is there that flow unsteadiness, curvature and rotation are more evident.
A repeatability analysis of 32 runs of the same event has been done, considering the horizontal position of the wave crest profile, providing an error estimation within 10mm.
The high repeatability of the phenomenon it has been an essential condition for the accuracy of the present experimental study and of future numerical investigation. For the measurements of the kinematic quantities, the Particle Image Velocimetry (PIV) method has been used. A number of 2048 realizations have been done in order to obtain a good statistical analysis.
The gentle breaker here studied evolves in shallow water, hence the use of scaling typical of shallow water flows (i.e. still-water depth h_0 for the lengths and $\sqrt{g/h_0}$ for the times). All results have been given in dimensionless form for portability.
The evolution of the breaker is described in terms of both global and local features. Global characteristics, like wave height and wave steepness describe a flow characterized by an initial growth until the maxima of H and steepness are achieved at the times $t^* = 12.47$ and 12.89 after the start of the motion, respectively. However, while the wave height immediately and rapidly decays after peaking, the wave steepness remains constant at about 0.25 till $t^* = 14.15$ before decreasing.

The times of peaking of H and steepness are larger than the onset times for breaking based on various criteria. In summary, breaking is predicted to occur: at the earliest, $t^* = 11.63$, by the appearance of significant levels of both vorticity (at crest) and turbulence (slightly upstream of crest); slightly later by the novel criterion of Banner and co-workers (at $t^* = 12.05$), when also air entrainment is seen to start and somehow later by the attainment of maxima wave height and steepness.

The mean flow in the tank motion reference frame is characterized by a quadrupolar vortical structure connected by a saddle point, which at breaking onset is near the free surface at the lee of the crest. Later on the saddle point is seen to move upstream and downward of the wave crest. The mentioned flow structure has significant similarities with those observed in the numerical simulations by Watanabe et al. (2005). However, a more detailed analysis is needed for a thorough comparison.

The most interesting dynamics are those related with the evolution of the vortical and turbulent flows. Two main stages characterize such evolution.

Stage (1) goes from the onset of breaking ($t^* = 11.63$) and includes the generation of vorticity and TKE (phase a) and their lengthening down the front face of the wave (phase b), till $t^* = 13.31 - 13.73$. At the end of this stage: a) the peaks of vorticity and TKE have reached their most upstream location, which can be regarded as the toe of the breaker, b) the whole crest has deformed, being it made of two bumps, one coinciding with the top of the crest (bump (i)) and one just downstream of the toe of the breaker (bump (ii)). During this stage the thickness and downstream length of the single-phase turbulent region remain almost constant ($b \approx 0.03, L_s \approx 1$). Fitting of the crossflow profiles of the mean streamwise velocities with cubic power laws is excellent and reveals a positive mean shear at the top of the layer.

Stage (2) goes from the peaks of vorticity and TKE reaching their most upstream location ($t^* = 13.31 - 13.73$) till the wave attains a quasi-steady shape ($t^* = 16.25$). This stage is characterized by a pulsation in intensity of both vorticity and TKE for which their peak values may increase/decrease of about 100%. This stage closes when the lower edge of the single-phase turbulent region Υ becomes almost horizontal and the wave undergoes a quasi-steady evolution. Fitting of the crossflow profiles of the mean streamwise velocities with cubic power laws suggests a negative mean shear at the top of the layer.

Because of the above, stage (1) can be regarded as "build-up" stage where vorticity and TKE rapidly grow to their maxima in intensity and extension, while stage (2) can be seen as a "relaxation" stage from the build-up to the following quasi-steady evolution, such a relaxation being characterized by some significant flow pulsation. The analysis of the flow evolving over the above two stages suggests that vorticity and TKE are more influenced by local dynamics

associated with the flow curvature and rotation than by global dynamics like the wave steepening, this is particularly visible during stage (1).

Bibliography

Abrahamsen, B. C.
2011. *Sloshing induced tank-roof impact with entrapped air pocket*. PhD thesis, Norwegian University of Science and Technology, Trondheim, Norway.

Antuono, M., A. Bardazzi, C. Lugni, and M. Brocchini
2014. A shallow-water sloshing model for wave breaking in rectangular tank. *J. Fluid Mech*, (746):437–465.

Babanin, A., D. Chalikov, I. Young, and I. Savelyev
2007. Predicting the breaking onset of surface water waves. *Geophysical Research Letters*, 34(7). L07605.

Babanin, A. V., D. Chalikov, I. R. Young, and I. Savelyev
2010. Numerical and laboratory investigation of breaking of steep two-dimensional waves in deep water. *Journal of Fluid Mechanics*, 644:433–463.

Banner, M. L. and W. L. Peirson
2007. Wave breaking onset and strength for two-dimensional deep-water wave groups. *Journal of Fluid Mechanics*, 585:93–115.

Banner, M. L. and D. H. Peregrine
1993. Wave breaking in deep water. *Annual Review of Fluid Mechanics*, 25(1):373–397.

Banner, M. L. and O. M. Phillips
1974. On the incipient breaking of small scale waves. *Journal of Fluid Mechanics*, 65(4):647–656.

Barthelemy, X., M. Banner, W. Peirson, F. Fedele, M. Allis, and F. Dias
2015. On the local properties of highly nonlinear unsteady gravity water waves. part 2. dynamics and onset of breaking. *arXiv preprint arXiv:1508.06002*.

Barthelemy, X., M. L. Banner, W. L. Peirson, F. Fedele, M. Allis, and F. Dias
2015. On the local properties of highly nonlinear unsteady gravity water waves. Part 2. Dynamics and onset of breaking. *ArXiv e-prints*.

Battjes, J. and T. Sakai
1980. Velocity field in a steady breaker. In *Coastal Engineering 1980*, Pp. 499–511.

Bouscasse, B., M. Antuono, A. Colagrossi, and C. Lugni
2013. Numerical and Experimental Investigation of Nonlinear Shallow Water Sloshing. *International Journal Of Nonlinear Sciences and Numerical Simulation*, 14(2):123–138.

Bradshaw, P.
1973. Effects of streamline curvature on turbulent flow (no. agard-ag-169). Technical report, DTIC Document.

Brocchini, M.
1996. *Flows with freely moving boundaries: the swash zone and turbulence at a free surface*. PhD thesis, University of Bristol, School of Mathematics.

Brocchini, M.
2002. Free surface boundary conditions at a bubbly/weakly splashing air–water interface. *Physics of Fluids*, 14(6):1834–1840.

Brocchini, M. and D. Peregrine
2001a. The dynamics of strong turbulence at free surfaces. part 1. description. *Journal of Fluid Mechanics*, 449:225–254.

Brocchini, M. and D. Peregrine
2001b. The dynamics of strong turbulence at free surfaces. part 2. free-surface boundary conditions. *Journal of Fluid Mechanics*, 449:255–290.

Chaplin, J. R. et al.
1996. On frequency-focusing unidirectional waves. *International Journal of Offshore and Polar Engineering*, 6(02).

Cointe, R. and M. P. Tulin
1994. A theory of steady breakers. *Journal of Fluid Mechanics*, 276:1–20.

Colagrossi, A., C. Lugni, G. M, and F. OM
2004. Experimental and numerical investigation of 2d sloshing with slamming,. In *Proceeding 19th Int. Workshop on Water Waves and Floating Bodies*, Pp. –.

Colicchio, G.
2004. *Violent disturbance and fragmentation of free surface*. PhD thesis, University of Southampton, School of engineering and the enviroment.

Dabiri, D. and M. Gharib
1997. Experimental investigation of the vorticity generation within a spilling water wave. *Journal of Fluid Mechanics*, 330:113–139.

Deike, L., S. Popinet, and W. K. Melville
2015. Capillary effects on wave breaking. *Journal of Fluid Mechanics*, 769:541–569.

Diorio, J., X. Liu, and J. Duncan
2009. An experimental investigation of incipient spilling breakers. *Journal of Fluid Mechanics*, 633:271–283.

Drazen, D. A., W. K. Melville, and L. Lenain
2008. Inertial scaling of dissipation in unsteady breaking waves. *Journal of Fluid Mechanics*, 611:307–332.

Duncan, J.
2001. Spilling breakers. *Annual Review of Fluid Mechanics*, 33(1):519–547.

Duncan, J. H. and A. A. Dimas
1996. Surface ripples due to steady breaking waves. *Journal of Fluid Mechanics*, 329:309–339.

Duncan, J. H., V. Philomin, M. Behres, and J. Kimmel
1994. The formation of spilling breaking water waves. *Physics of Fluids*, 6(8):2558–2560.

Duncan, J. H., H. Qiao, V. Philomin, and A. Wenz
1999. Gentle spilling breakers: crest profile evolution. *Journal of Fluid Mechanics*, 379:191–222.

Faltinsen, O. M. and A. N. Timokha
2009. *Sloshing*. Cambridge University Press.

Fedele, F.
2014a. Geometric phases of water waves. *EPL (Europhysics Letters)*, 107(6):69001.

Fedele, F.
2014b. On certain properties of the compact zakharov equation. *Journal of Fluid Mechanics*, 748:692–711.

Hornung, H. G., C. Willert, and S. Turner
1995. The flow field downstream of a hydraulic jump. *Journal of Fluid Mechanics*, 287:299–316.

Hoyt, J. W. and R. Sellin
1989. Hydraulic jump as "mixing layer". *Journal of Hydraulic Engineering*, 115(12):1607–1614.

Lin, J.-C. and D. Rockwell
1994. Instantaneous structure of a breaking wave. *Physics of Fluids*, 6(9):2877–2879.

Lin, J.-C. and D. Rockwell
1995. Evolution of a quasi-steady breaking wave. *Journal of Fluid Mechanics*, 302:29–44.

Longuet-Higgins, M. S.
1963. The generation of capillary waves by steep gravity waves. *Journal of Fluid Mechanics*, 16(1):138–159.

Longuet-Higgins, M. S.
1973. A model of flow separation at a free surface. *Journal of Fluid Mechanics*, 57(1):129–148.

Longuet-Higgins, M. S.
1985. Accelerations in steep gravity waves. *Journal of Physical Oceanography*, 15(11):1570–1579.

Longuet-Higgins, M. S.
1990. Flow separation near the crests of short gravity waves. *Journal of Physical Oceanography*, 20(4):595–599.

Longuet-Higgins, M. S.
1992. Capillary rollers and bores. *Journal of Fluid Mechanics*, 240:659–679.

Longuet-Higgins, M. S.
1994. Shear instability in spilling breakers. In *Proceedings of the Royal Society of London A: Mathematical, Physical and Engineering Sciences*, volume 446, Pp. 399–409. The Royal Society.

Longuet-Higgins, M. S. and J. Turner
1974. An 'entraining plume'model of a spilling breaker. *Journal of Fluid Mechanics*, 63(01):1–20.

Lugni, C., A. Bardazzi, O. M. Faltinsen, and G. Graziani
2014. Hydroelastic slamming response in the evolution of a flip-through event during shallow-liquid sloshing. *Physics of Fluids*, 26(3).

Lugni, C., M. Brocchini, and O. M. Faltinsen
2006. Wave impact loads: The role of the flip-through. *Physics Of Fluids*, 18(12).

Lugni, C., M. Brocchini, and O. M. Faltinsen
2010a. Evolution of the air cavity during a depressurized wave impact. II. The dynamic field. *Physics Of Fluids*, 22(5).

Lugni, C., M. Miozzi, M. Brocchini, and O. M. Faltinsen
2010b. Evolution of the air cavity during a depressurized wave impact. I. The kinematic flow field. *Physics Of Fluids*, 22(5).

Madsen, P. A. and I. A. Svendsen
1983. Turbulent bores and hydraulic jumps. *Journal of Fluid Mechanics*, 129:1–25.

Misra, S., J. Kirby, M. Brocchini, F. Veron, M. Thomas, and C. Kambhamettu
2008. The mean and turbulent flow structure of a weak hydraulic jump. *Physics of Fluids (1994-present)*, 20(3):035106.

Misra, S. K., M. Brocchini, and J. T. Kirby
2006. Turbulent interfacial boundary conditions for spilling breakers. In *Coastal Engineering Conference*, volume 30, P. 214. Asce American Society Of Civil Engineers.

Misra, S. K., J. T. Kirby, M. Brocchini, M. Thomas, F. Veron, and C. Kambhamettu
2004. Extra strain rates in spilling breaking waves. In *Coastal Engineering Conference*, volume 29, P. 370. Asce American Society Of Civil Engineers.

Monahan, E. C. and G. Mac Niocaill
2012. *Oceanic Whitecaps: And Their Role in Air-Sea Exchange Processes*, volume 2. Springer Science & Business Media.

Moore, D. W.
1978. The equation of motion of a vortex layer of small thickness. *Studies in Applied Mathematics*, 58(2):119–140.

Mossa, M.
2008. Experimental study of the flow field with spilling type breaking. *Journal of Hydraulic Research*, 46(sup1):81–86.

Nepf, H., C. Wu, and E. Chan
1998. A comparison of two-and three-dimensional wave breaking. *Journal of Physical Oceanography*, 28(7):1496–1510.

Oh, S.-H., N. Mizutani, K.-D. Suh, and N. Hashimoto
2005. Experimental investigation of breaking criteria of deepwater wind waves under strong wind action. *Applied Ocean Research*, 27(4–5):235 – 250.

Peregrine, D. and I. Svendsen
1978. Spilling breakers, bores, and hydraulic jumps. *Coastal Engineering Proceedings*, 1(16).

Peregrine, D. H.
1992. *Mechanisms of Water-Wave Breaking*. Berlin, Heidelberg: Springer Berlin Heidelberg.

Perlin, M., W. Choi, and Z. Tian
2013. Breaking waves in deep and intermediate waters. *Annual Review of Fluid Mechanics*, 45:115–145.

Phillips, O. M.
1958. The equilibrium range in the spectrum of wind-generated waves. *Journal of Fluid Mechanics*, 4(4):426–434.

Qiao, H. and J. H. Duncan
2001. Gentle spilling breakers: crest flow-field evolution. *Journal of Fluid Mechanics*, 439:57–85.

Rapp, R. J. and W. K. Melville
1990. Laboratory measurements of deep-water breaking waves. *Philosophical Transactions of the Royal Society of London A: Mathematical, Physical and Engineering Sciences*, 331(1622):735–800.

Scarano, F.
2002. Iterative image deformation methods in piv. *Measurement Science and Technology*, 13(1):1–19.

Schultz, W. W., J. Huh, and O. M. Griffin
1994. Potential energy in steep and breaking waves. *Journal of Fluid Mechanics*, 278:201–228.

Shao, Y.-L. and O. M. Faltinsen
2012. Towards efficient fully-nonlinear potential-flow solvers in marine hydrodynamics. In *ASME 2012 31st International Conference on Ocean, Offshore and Arctic Engineering*, Pp. 369–380. American Society of Mechanical Engineers.

Shao, Y.-L. and O. M. Faltinsen
2014. A harmonic polynomial cell (hpc) method for 3d laplace equation with application in marine hydrodynamics. *Journal of Computational Physics*, 274:312–332.

Snyder, R. L., L. Smith, and R. M. Kennedy
1983. On the formation of whitecaps by a threshold mechanism. part iii: Field

experiment and comparison with theory. *Journal of Physical Oceanography*, 13(8):1505–1518.

Soldati, A. and C. Marchioli
2009. Physics and modelling of turbulent particle deposition and entrainment: Review of a systematic study. *International Journal of Multiphase Flow*, 35(9):827 – 839. Special Issue: Point-Particle Model for Disperse Turbulent Flows.

Tennekes, H. and J. Lumley
1972. *A First Course in Turbulence*. Pe Men Book Company.

Tian, Z., M. Perlin, and W. Choi
2008. Evaluation of a deep-water wave breaking criterion. *Physics of Fluids*, 20(6).

Tian, Z., M. Perlin, and W. Choi
2010. Energy dissipation in two-dimensional unsteady plunging breakers and an eddy viscosity model. *Journal of Fluid Mechanics*, 655:217–257.

Tulin, M. and M. Landrini
2001. Breaking waves in the ocean and around ships. In *Twenty-Third Symposium on Naval Hydrodynamics*.

Tulin, M. P. and T. Waseda
1999. Laboratory observations of wave group evolution, including breaking effects. *Journal of Fluid Mechanics*, 378:197–232.

Watanabe, Y., H. Saeki, and R. J. Hosking
2005. Three-dimensional vortex structures under breaking waves. *Journal of Fluid Mechanics*, 545:291–328.

Wu, C. H. and H. Nepf
2002. Breaking criteria and energy losses for three-dimensional wave breaking. *Journal of Geophysical Research: Oceans*, 107(C10).